AIX-MARSEILLE UNIVERSITE

Réalisation de Détecteurs de Neutrons en Carbure de Silicium

THÈSE

Présentée pour obtenir le grade de

DOCTEUR D'UNIVERSITE

Présentée Par

FATIMA ISSA

ECOLE DOCTORALE N°353

SCIENCES POUR L'INGENIEUR : MECANIQUE, PHYSIQUE, MICRO ET NANOELECTRONIQUE

Soutenue publiquement le 19/02/2015, devant la commission d'examen :

Président du jury:	Pr. Dominique Planson	INSA de Lyon
Rapporteur:	Pr. Gaël Gautier	INSA CVL
Rapporteur :	Pr. Abdel Mjid Nourreddine	Université de Strasbourg
Directeur de thèse:	Pr. Olivier Palais	Université Aix-Marseille
Co-directeur de thèse :	Pr. Abdallah Lyoussi	CEA/Cadarache
Co-directeur de thèse:	Dr. Laurent Ottaviani	Université Aix-Marseille
Examinateur:	Dr. Isabelle Schuster	KIC InnoEnergy
Membre invité:	Eng. Richard Saenger	Schlumberger

ABSTRACT

Nuclear radiation detectors are important tools in many fields such as in nuclear reactors, homeland security and medical applications. Recent advances in semiconductor technology allow construction of highly efficient low noise detectors for different nuclear radiations. Silicon carbide (SiC) is a wide band gap semiconductor with a high thermal conductivity and high radiation resistance. It is suitable for a harsh environment where high temperatures and radiation fluxes may exist. In the framework of the European project (I_SMART) the purpose of this work is to demonstrate the reliability of new methods of realizing nuclear radiation detectors and to study their performance under different types of irradiation (fast and thermal neutrons) and at elevated temperatures. Different methods have been used to realize SiC based-radiation detectors. For instance boron ion implantation has been used to create the neutron converter layer either in the metallic contact or directly in the SiC. The fabricated detectors have been tested in the BR1 nuclear reactor revealing the thermal neutron detection and the feasibility of gamma discrimination from thermal neutrons using one single detector. Such detectors are sensitive to fast neutrons with a stable response under elevated temperatures (up to 150 °C). Furthermore, the studied detectors show stability under different neutron fluxes, indicating a reliability of such new methods of realizing radiation detectors which could replace those of the current state of the art.

RÉSUMÉ

Les détecteurs de radiations nucléaires sont des outils importants dans de nombreux domaines tels que dans les réacteurs nucléaires, la sécurité nationale, mais ils sont également primordiaux dans des applications médicales. Les progrès récents dans la technologie des semi-conducteurs permettent la réalisation de détecteurs très efficaces et quasi-insonores qui permettent la détection de différents types de radiations nucléaires. Le carbure de silicium (SiC) est une bande semi-conductrice large, grâce à sa conductivité thermique élevée et à une résistance élevée aux rayonnements, il est adapté pour les environnements difficiles où peuvent exister des flux élevés de température et de rayonnement. Le but du projet européen (I_SMART) est ainsi de prouver la fiabilité de nouvelles méthodes de réalisation de détecteurs de radiations nucléaires et d'étudier leur performance dans différents types d'irradiation (neutrons rapides et thermiques) et à différentes températures. Différentes méthodes ont été utilisées pour réaliser les détecteurs de rayonnement SiC. Par exemple l'implantation d'ions de bore a été utilisé pour créer la couche de conversion de neutrons soit dans le contact métallique ou directement en SiC. Les détecteurs fabriqués ont été testés dans le réacteur nucléaire BR1, mettant en lumière la présence de neutrons thermiques. En outre, ces détecteurs détectent des neutrons rapides sous n'importe quelle température. En outre, les détecteurs utilisés montrent leur stabilité sous différents flux de neutrons qui indiquent la fiabilité de ces nouveaux modes de réalisation de détecteurs de rayonnement qui pourraient remplacer ceux utilisés actuellement.

ACKNOWLEDGEMENTS

This work has been performed within the frame work of the European project I_SMART at Aix-Marseille University. Throughout these years I developed many skills thanks to my supervisors Dr. Laurent Ottaviani, Pr. Abdallah Lyoussi, and Pr. Olivier Palais for encouraging my research and for allowing me to grow as a research scientist and for providing me with a good atmosphere for doing research. I would like to thank you for your positive attitude and continuous encouragements.

I would also like to thank my committee members, Pr. Dominique Planson, Pr. Abdel Mjid Nourreddine, Pr. Gaël Gautier, Dr. Isabelle Schuster, and Eng. Richard Saenger for serving as my committee members. I thank you for a number of important comments and corrections, which significantly improved this manuscript.

I would also like to acknowledge with all praise and thanks to the group of OPTO-PV students and Professors for all their support during my work at Aix-Marseille University. My special thanks for my colleague Dr. Vanessa Vervish, Dr. Raffaello Ferone and Dr. Stephane Biondo and Dora Szalkai for all the very nice time we spent together and also for the valuable discussion we did which improved my work.

Special thank goes to Dr. Ludo Vermeeren, at SCK.CEN for his help during the irradiation tests and for all the scientific and non-scientific discussions, I learned a lot from him. I would also like to thank Dr. Andrej Kuznetsov for his help during my work at University of Oslo.

I gratefully acknowledge the Knowledge and Innovation Community (KIC InnoEnergy) through the European project Innovative Sensor for Material Ageing and Radiation Testing I_SMART. This research work was supported financially by the PACA Région, CEA Cadarache and by ANR agency ANR-12-EITE-0004-01.

A special thanks to my family. Words cannot express how grateful I am to my father, my mother and my brothers for all of the sacrifices that you've made on my behalf. At the end I would like to thank my beloved husband Mohamad who supported me for everything, and thank you for encouraging me throughout this experience.

Table of Contents

Table of figures

List of tables

List of Acronyms

ADC	Analogue-to-digital converter
CCE	Charge Collection Efficiency
CSP	Charge sensitive preamplifier
DLTS	Deep level transient spectroscopy
D-T	Deuterium tritium
FWHM	Full width at half maximum
LiF	Lithium Fluoride
MCA	Multichannel analyzer
NCL	Neutron converter layer
PIII	Plasma immersion ion implantation
PHS	Pulse height spectra
RT	Room temperature
RIE	Reactive ion etching
RTA	Rapid thermal annealing
SCR	Space charge region
SiC	Silicon carbide
SNR	Signal-to-noise ratio
SRIM	Stopping and range of ions in matter
SIMS	Secondary ion mass spectroscopy

Introduction

Nuclear radiation detectors are important tools in many fields such as in nuclear reactors, high energy particle physics experiments, and in medical applications such as in boron neutron capture therapy or in radiography (x-ray radiography or neutron radiography). Additionally such detectors are crucial in homeland security for detecting nuclear weapons and special nuclear materials to thwart nuclear proliferation and terrorism and to secure weapons and materials worldwide. Typically nuclear weapons contain material which emits notably gammas and neutrons generating a detectable radiation. Moreover such detectors can be used in well logging. Generally a radioactive source such as ^{241}Am-Be can be used for emitting neutrons. The emitted radiation interacts with the formation and backscattered to a detector with information on a particular target that can be evaluated. Furthermore radiation detectors are necessary in nuclear reactors to enhance the safety conditions in nuclear instrumentations and to have detailed nuclear reactor monitoring. This is needed because global demand for green energy is always in increase requiring effective clean source of energy. Currently nuclear energy seems to be the most mature in this manner. However to avoid serious accidents such as Chernobyl and Fukushima nuclear reactors which had severe effects on humans and environment, this requires more efforts to enhance the safety conditions in nuclear instrumentations and to have detailed nuclear reactor monitoring. This could make nuclear energy more reliable energy source and may change public opinion about this major source of energy.

All what have mentioned and other pressing global issues have created tremendous demand for, robust neutron detectors especially for harsh environments that can replace the current state-of-the art. Currently the European project "I_SMART" (Innovative Sensor for Material Ageing and Radiation Testing), is trying to satisfy some of these demands. The main objective of this project is to develop an innovative complete radiation detection system for enhancing the safety of nuclear power installations. Such a detection system will be used in severe media where high temperature (300-600 °C), high pressure, and high dose rate exist. Currently there is no available system for spectroscopic radiation monitoring for elevated temperatures

(up to 600 °C). The complete system will be comprised of the detector, the electronics, and the treatment and analysis methodology, probably all will be manufactured in one chip. Since inside the reactor there are thermal and fast neutrons as well as gamma irradiations it is obvious that such a system should be able to detect and discriminate each of these radiations. As a part of this project, the purpose of this work is to prove the reliability of new methods of realizing nuclear radiation detectors and study their performance under different types of irradiation (fast and thermal neutrons) and at different temperatures. Therefore in what follows we just focus on the detector itself and its operation ignoring the electronics of the whole system.

Taking into consideration that the final prototype will be placed in harsh environments, the material based detectors should be well chosen. Recent advances in semiconductor technology allow construction of highly efficient and low noise detectors for different ionizing radiation detection. Although conventional semiconductor such as silicon is currently widely used for device manufacturing, it is not the proper material dedicated to high temperature, and radiation rich environments due to its relatively small bandgap and low thermal conductivity. As an alternative to the conventional semiconductor, silicon carbide (SiC) has been developed as radiation detectors for harsh environments. Improvements in SiC material processing have provided an opportunity to offer a feasible replacement for Si in devices for harsh environment applications. Thanks to its wide band gap, high radiation resistance and high thermal conductivity. SiC is one of the best candidates to be dedicated for such environments. In the first chapter we highlighted the properties that make this semiconductor one of the best candidate for high temperatures and high irradiation fluxes after reviewing the state-of-art of the current detectors. Moreover the principles of interaction of different radiations with matter and the types of the current SiC-based detectors are summarized as well in this chapter.

Regarding what have mentioned we realized SiC-based detectors. These detectors are fabricated by new methods mainly based on ion implantation of boron. Referring to the SRIM simulations (Stopping and Range of Ions in Matter) presented in chapter two we chose the proper thickness of the active region of the detector and its position with respect to the boron based-neutron converter layer (NCL). Such a layer

is necessary to converts neutrons into detectable charged particles. Then in chapter three we described in some details the way used to fabricate four different types of detectors where the first type is implanted by Al to create the p+ layer followed by and ^{10}B ion implantation to realize the NCL. The second type is implanted directly by ^{10}B to create the p+ layer and the NCL simultaneously. In the third type ^{10}B is implanted into the ohmic contact of the SiC-based pn junction. In the last geometry a thin layer of boron has been sputtered on the top of a 4H-SiC p-n junction. Then the electrical characteristics for the manufactured diodes were measured.

After realizing and characterizing the detectors they have been irradiated under different types of irradiations in order to evaluate the performance of each type under different types of irradiation. Chapter four summarizes the main results of these irradiation tests. Moreover the thermal stability of the neutron detectors has been examined. Finally, some concluding remarks and a future outlook of the current work are given in Chapter 4.

This page intentionally left blank

Chapter 1. Introduction to SiC Radiation Detectors

Radiation detectors based on semiconductor materials have received considerable attentions in recent years over other types of detectors such as gas-filled counters. In this chapter we will state the different types of radiation detectors, and the advantages of semiconductor based detectors over other types. Moreover, we will answer the question why SiC-based detectors are better than conventional semiconductor for harsh environment? At the end of this chapter we will describe the way different radiations interact with matter and the way different SiC-based radiation detectors are realized and their responses under different types of irradiation.

1.1 Types of irradiation

The term radiation is commonly used to describe the energy travelling through space. Radiation can be classified into ionizing and nonionizing radiation. Ionizing radiation refers to radiation that has enough energy to remove electrons from the atom and to break the chemical bonds creating highly reactive ions. Heavy charged particles, beta particles, neutrons, gamma and X-rays are all examples of ionizing radiations. These radiations differ in their principle of interaction with matter and thus their ability to penetrate different thicknesses of specific materials as shown in figure 1.1. For example alpha particles due to their relatively heavy mass are less penetrative than beta particles. However gamma and neutrons are more penetrative which requires a thick layer of lead or concrete respectively to stop them.

Since these radiations are hazardous and can't be detected by the human senses, specific types of detectors are required for detecting and measuring such radiation. These detectors have many applications in different fields such as for the safety in nuclear instrumentations, for homeland security and radiotherapy (example BNCT; Boron Neutron Capture Therapy). The operation of any radiation detector basically depends on the way the radiation to be detected interacts with the detector itself. Studying these interactions is necessary before designing any detector in order to interpret its response. The radiations of our concern are thermal neutrons but as we will see that some of these interactions are followed by gamma and alpha emission, so it is important to understand the behavior of these radiations as well.

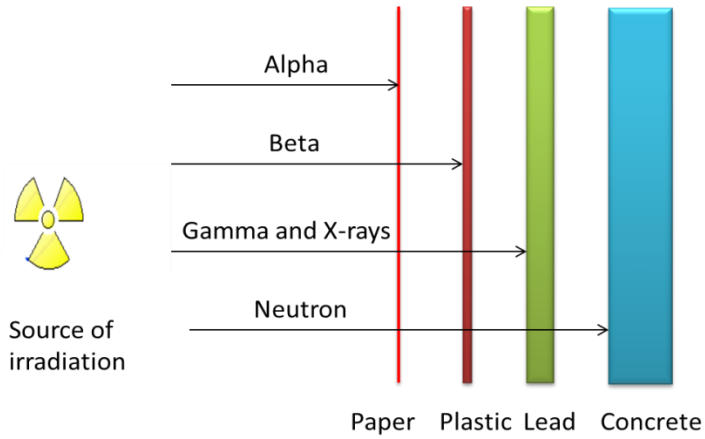

Figure 1.1 Effective shielding materials for various types of irradiation

Currently there are many types of radiation detectors used in different fields. Such detectors are specified according to the type of the detection medium used such as gas-filled, scintillation and semiconductor detectors.

1.2 Gas-filled and scintillation detectors

Typically gas-filled detector consists of a volume of gas between two electrodes, with an applied voltage between them. As the radiation passes through the gas, ion pair could be produced if the energy of the incident particle is greater than the average energy needed to create electron-ion in gas. Typically the average energy

required to produce an ion pair is 25-35 eV/ ion pair [1]. The resulted positive ions and the free electrons move to the cathode and the anode respectively. As a result of the movement of the charge pairs, a perturbation in the electric field occurs leading to a pulse at the electrodes. However scintillation detectors are one of the oldest detectors for ionizing radiation. The principle of detection relies on the emission of light photons due to the interaction of radiation with the scintillation material used in the detector. Usually a photomultiplier is used to convert the extremely weak light output of a scintillation pulse into a corresponding electrical signal.

For example the most commonly known gas-filled neutron detectors are those containing either Boron Trifluoride (BF_3) or Helium-3 (^3He) [2]. However the use of ^3He, in particular, is becoming more and more of a problem because of the severe ^3He shortage, hence a replacement technology for neutron detection is required. The use of BF_3 could arise as a solution for replacing ^3He. BF_3 counters are similar to ^3He but with lower efficiency and with higher gamma discrimination due to their higher Q-value. The problem, however, is the hazardous nature of BF_3 gas which has led to this technology being largely discontinued. On the other hand neutron-induced fission reaction can be also used for neutron detection in a fission chamber. The walls of the fission chambers are usually lined with highly enriched uranium to enhance the ionization current. Due to the high energy released by such reaction a good discrimination from the background could be achieved. The typical operating voltage varies from 50 to 300 V. The gradual burn-up of neutron sensitive material is a problem for long–term operation for in-core operation. This requires the use of fissile and fertile material in the neutron sensitive lining of the chamber.

1.3 Semiconductor detectors for harsh environments

Furthermore, devices using semiconductor as the basic detection medium were available since 1960, and they are known as semiconductor diode detectors or solid-state detectors. Semiconductor detectors are expensive, because extremely pure starting material is required. The operation of most semiconductor detectors is based on the use of a p-n junction or a Schottky diode which will be explained in details in chapter 2. The principle of detection in solid detectors relies on the creation of electron-hole pairs which are somehow analogous to the ion pair created in gas-filled detectors. Because their density is about 1000 times greater than that for gas, solid-

state detectors are available with compact sizes which still produce enough signals to be measured. Furthermore the best energy resolution from any radiation spectrometers can be achieved by semiconductor detector, because of the large number of carriers that are created for a given incident radiation event compared with other types of detectors. For example 3.6 eV is the average energy needed to create an electron-hole pair in Si detectors which is much smaller than the ionization energy of gases (around 30 eV). Another desirable feature of these detectors is their relatively fast charge-collection times (due to the mobility of electron-hole pairs)[1][3]. However some drawbacks may include the limitation to small sizes and the degradation of the performance of the detector due to radiation-induced damage especially with the use of conventional semiconductors such as silicon (Si) and germanium (Ge).

Although semiconductor detectors offer many advantages over other types of detectors, the conventional semiconductor is still too sensitive to be used in harsh environments where high temperature and high irradiation fluxes exist. Conventional semiconductors such as silicon and germanium have been used to fabricate different types of radiation detectors.

Currently Si is the most commonly used semiconductor material and its major advantage resides in its availability to be produced with a very high quality. Although its small energy band gap (1.12 eV at room temperature) is enough to produce a large number of charge carriers per unit energy loss of the ionizing particles to be detected, detectors based on Si materials are still sensitive to be used for harsh environments applications. Despite the efforts to increase the radiation hardness of Si pixel detectors by hydrogenated amorphous Si and oxygenated Si [4], other wide band gap semiconductors seem to be better candidates to be used in harsh environments [4][5][7]. Silicon detectors suffer severe radiation damage which leads to low energy resolution. The performance of Si detector [8] was degraded by 3 MeV protons irradiation. Additionally, the main limitation in Si is its high dark current which generally confines Si-based detector to operate at temperature lower than 30 °C. This effect is related to the thermal generation of charge carriers at temperatures as low as 30 – 40 °C.

As an alternative to the conventional semiconductors, wide band gap semiconductors such as silicon carbide (SiC), gallium nitride (GaN) and diamond (D) have received considerable attentions in recent years. Independent of which type of semiconductor material is used, specific properties are required for realizing high performance spectrometers especially for harsh environments. Typically ionizing radiation semiconductor detectors for such environments could be used in different fields; such as for controlling nuclear plants and guiding systems for satellites and shuttles. The various significant electrical and mechanical properties for a range of semiconductor materials are summarized in table 1.1 [9].

Table 1.1 Comparison of properties of selected different semiconductor materials

Property	**Si**	**Ge**	**GaAs**	**GaN**	**D**	**4H-SiC**
Bandgap (eV)	1.12	0.67	1.42	3.45	5.5	3.27
Density ($g \cdot cm^{-3}$)	2.3	5.33	5.3	6.2	3.5	3.2
Atomic number Z	14	32	31-33	31-7	6	14-6
Relative dielectric constant	11.9	16	13.1	9	5.7	10
Breakdown field ($MV \cdot cm^{-1}$)	0.3	0.1	0.4	2	10	3
e-hole creation energy (eV)	3.6	2.95	4.3	8.9	13	7.78
Electron mobility at 300 K ($cm^2 V^{-1} S^{-1}$)	1300	3900	8500	1000	1800	800
Hole mobility at 300 K ($cm^2 V^{-1} S^{-1}$)	460	1900	400	30	1200	115
Threshold displacement energy (eV)	13-20	16-20	8-20	10-20	40-50	22-35
Thermal conductivity ($W/cm \cdot K$)	1.5	0.6	0.46	1.3	22	4.9

1.3.1 Wide band gap energy

The energy band gap of SiC, GaN and diamond are much larger than that of Si allowing their classifications as wide band gap semiconductors. Large band gap energy is essential parameter to fabricate devices with low leakage current and thus to allow their operation at high temperatures. In fact the reverse current is predominantly controlled by the intrinsic carrier concentration which is proportional to exp ($-E_g/2K_BT$). E_g is the energy band gap of the used semiconductor, K_B and T are the Boltzmann's constant (1.38×10^{-23} J/K) and the temperature respectively.

The importance of the low leakage current relies on its correlation with the signal-to-noise ratio. Thus devices with low leakage current, show high signal-to-noise ratio and high energy resolution. The wide energy band gap of SiC compared with Si or Ge leads to almost negligible thermally generated dark current. Although the use of wide band gap materials decrease the total signal since more energy is required for electron hole pair generation, it is still necessary to use such materials in order to reduce the thermal induced carriers which contribute to the dark current and thus to the noise level.

1.3.2 High atomic displacement energy

During the irradiation process, the energy of the incident particle is transferred to the lattice which may lead to the displacement of the atoms from their lattice site causing degradation of the detector performance. Depending on the type and energy of the impinging particle some defects are created such as vacancies, interstitials, Frenkel pairs and antisites. Generally neutrons and heavy charged particles lead to significant damage compared to highly ionizing radiations such as X and gamma irradiation. One important parameter that characterize the radiation damage processes in a material is the threshold energy, which is the minimum energy needed to create one of the previously mentioned defects. As shown on the above table, materials with the highest displacement energy are diamond and silicon carbide [10]**.** This property should lead to detectors capable for operating in high radiation environments. Materials with high threshold energy are needed for realizing detectors for high radiation environments to avoid the degradation of the detector. The degradation could be revealed by the creation of charge trapping centers which lead to the reduction of the output signal [11].

1.3.3 High thermal conductivity

The third most important parameter for detectors devoted to harsh environments is the thermal conductivity of the used material. The greater this value is, the better the material conducts heat to its surroundings, which means the device temperature increases slowly and thus no need for cooling systems. Moreover, the use of material with high thermal conductivity; such as SiC and diamond ensures the cooling down of the device itself without using external cooling systems. This property allows the SiC detectors to operate at high temperature up to 700 °C without cooling systems.

High purity semi-insulating SiC material has high thermal conductivity (4.9 W/cm·K). This value is almost four times that of GaN, which makes SiC more preferable for high temperature applications.

1.3.4 Small electron hole pair generation energy

If the energy deposited by a given ionizing radiation in a semiconductor detector is enough, it may result in the creation of the electron-hole pairs. The average energy needed to create electron-hole pairs is independent from the energy and the type of the ionizing radiation. The average energy needed to create an electron-hole pair in 4H-SiC is about 7.78 eV. This value is much lower than the energy necessary to create electron-ion pair in gas-filled (typically around 30 eV) detectors leading to higher resolution. This value should be small to ensure that the generated e-h pairs are enough to obtain high signal-to-noise ratio.

1.3.5 High purity and low defect

Actually, a perfect defect-free crystal where all the atoms are located in their correct position doesn't exist. Semiconductor crystals may contain some crystal defects such as vacancies (missing atoms in the crystal lattice), interstitials (excess of atoms in the crystal lattice) and dislocations (imperfection in crystal structure). These defects affect the performance of the device as they give rise to permitted levels in the energy bandgap which can trap free charge carriers and thus reduce the signal amplitude. In other words high purity of the semiconductor material is required in order to minimize signal charge trapping and recombination. Therefore using materials with low defect density is necessary for detectors to ensure full charge collection, high energy resolution and low dark current.

Back to table 1.1, it arises some wide band semiconductors with properties suitable for harsh environment applications. For instance diamond has the best theoretical performance. However, the current status of semiconducting diamond is far behind that of SiC in terms of availability of large-area device grade wafers and device processing maturity. One might speculate that diamond would be the future generation semiconductor. However, recently single-crystal chemical vapor deposition (sc-CVD) diamond detectors have been tested and compared with Si detector under irradiation by 5.5 MeV alpha-particles [12]. Si and diamond detectors

behave in same way and no significant change in the efficiency and the resolution was obtained. Another type of sc-CVD diamond detectors were irradiated by MeV protons [13]. It was found that the radiation hardness of diamond for MeV energy range protons is worse than that of Si and is superior at higher energies (GeV).

It seems that SiC device technology is much more advanced than GaN and diamond technology and is leading in research and commercialization efforts. The technology of diamond electronic devices is still in its early stages with respect to that of SiC, where the development of diamond bipolar junction transistor is still hindered by the availability of n-type diamond with high electron densities[14]. Furthermore, problems related to electrical contacts and the high activation energies of the some dopants (boron and nitrogen) still limit the commercial application of diamond.

Taking into account the above-mentioned properties (wide band gap, high thermal conductivity, high radiation resistance), it is clear that SiC is one of the best candidate semiconductor for realizing ionizing radiation detectors especially for harsh environments. In fact detectors based on SiC have proved their ability in detecting different types of ionizing radiations at high temperature and in harsh environments. Moreover since its technology is the most mature one among other wide bandgap semiconductors, we decided to realize our neutron detectors based on 4H-SiC. Therefore in what follows we will focus on SiC as a wide bandgap semiconductor and its development as radiation detectors and we will review the main results achieved by SiC detectors.

Beside all the superior properties of SiC materials mentioned above, another significant advantage of this material which is related to its advanced micro-electronic planar technology and the availability of a developed SiC technology which also allows the integration of the detector and the electronics on the same substrate which is one of the main aims of the I_SMART project. Moreover, the advanced micro-electronic planar technology of silicon carbide including the photolithography with high resolution is important to realize multi-electrode detectors such as pixel or microstrip types [6] [15].

1.4 Silicon Carbide

1.4.1 General properties

Silicon carbide is a wide band gap semiconductor suitable for many applications where high-power, high frequency, high temperature and high radiations may exist [16]. Among other wide band gap semiconductors, currently SiC is the most intensively studied semiconductor and its technology is the most mature.

Silicon carbide was first discovered by the Swedish scientist, Jons Jakob Berzelius in 1824 [17]. The history of man-made SiC starts with Edward G.Acheson in 1891 [18]. Acheson produced a crystalline product in an electric smelting furnace. This product was characterized by a great hardness which shown to be a compound of silicon and carbon he called it 'carborundum'. Natural SiC has been first discovered by Henri Moissan in 1905 [19] in Arizona. However naturally occurring SiC materials are very rare where it can be found in miniscule quantities in difficult geological places.

Later Lely in 1955 [20] proposed a new crystal growth technique. Although with Lely's method the crystal purity and properties could to some extent be controlled, there are still difficulties in processing high-purity SiC substrates. Consequently the modified Lely process, also called seeded sublimation growth, was developed by Tairov and Tsvetkov in 1978 [21].

Further development of SiC materials continued where now they are commercially available through several companies pioneered by Cree, which produce bulk and epitaxial SiC. Bulk SiC is available with thicknesses up to 400 μm while SiC epitaxial layers are available with much thinner thicknesses (lower than 150 μm) and with quality superior to that of the bulk. In other words the epitaxial SiC materials seem to dominate over bulk SiC for the near future thanks to their high purity. Further improvements in the thicknesses, quality and supply are always expected.

In fact the realization of high purity SiC materials was limited by some crystalline defects such as micropipes and basal plane dislocations. Micropipes are hollow defects that can act as trapping centers reducing the performance of the detector which were considered as detector killers. SiC with large diameter crystals tends to have higher density defects. However, thanks to the continuous progress in improving the SiC crystalline quality [22], [23], the density of these defects are

dramatically reduced during the last decade and development of SiC wafers with very low micropipe densities and with bigger diameter are now commercially available as shown in figure 1.2 and 1.3. Recently Dow Corning has demonstrated micropipe free material over a full 100 mm diameter [24].

Furthermore, due to the high interest in SiC, two main conferences were introduced focusing on the latest advances in investigations of crystal growth and characterization of material properties. These conferences are the International Conference on Silicon Carbide and Related Materials (ICSCRM) and the European Conference on Silicon Carbide and Related Materials (ECSCRM).

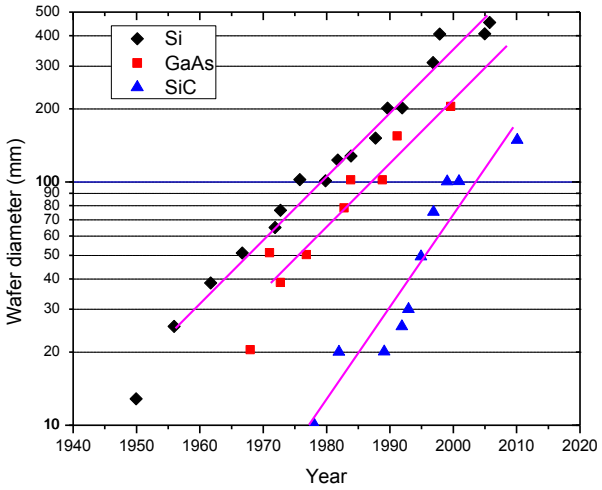

Figure 1.2 The progress in SiC wafer diameter compared to that of Si and GaAs [24]

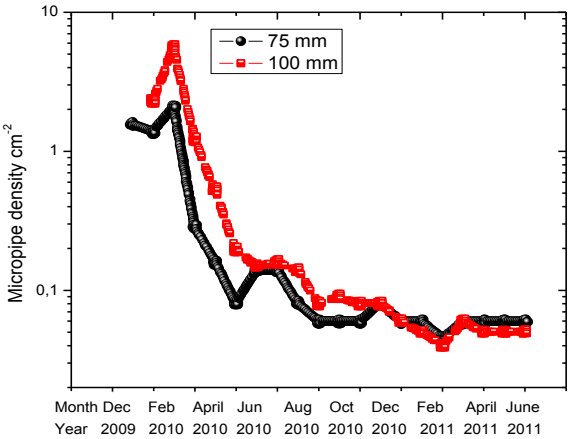

Figure 1.3 The reduction in the micropipe density in 100 mm n-type 4H-SiC wafers vs. time [24]

1.4.2 Crystalline structure

The basic unit of a silicon carbide crystal is a tetrahedron with four Si atoms and one C atom in the center as shown in figure 1.4. The distance between carbon and silicon atom is 1.89 Å while the distance between carbon atoms is 3.08 Å. The SiC crystals are constructed with such tetrahedra attached to each other at the corners.

Silicon carbide has over 200 polytypes which refers to different crystal structures with the same stoichiometry of a compound semiconductor. In such polytypes similar layer of atoms are stacked atop of each other. The different directions perpendicular to these layers would arise in a variety of polytypes. By referring to the possible positions of the layers as A, B and C, the polytype can be constructed by arranging the layers in a specific order, with the restriction that layers with the same notation cannot be stacked upon each other.

The crystal structures of SiC polytypes are: cubic, hexagonal or rhombohedral, for which the letters C, H and R refer respectively. The only cubic polytype in SiC is the 3C-SiC which is also known as β-SiC, which has the stacking sequence ABCABC. Some of the well-known polytypes are: 2H-SiC, 4H-SiC and 6H-SiC with the corresponding stacking sequences, ABAB, ABCBABCB, and ABCACBABCACB respectively as shown in figure 1.5.

Despite the fact that all SiC polytypes consist of 50% C atoms and 50% Si atoms, each SiC polytype has its own distinct set of electronic and optical properties. For example the bandgap of 4H-SiC is 3.265 eV while that of 6H-SiC is 3.023 eV. The most commercially available SiC polytypes are 6H- and 4H-SiC which are available in both bulk wafers and epitaxial layers. Being with wider bandgap and the one with more isotropic electrical properties, 4H-SiC is more preferable than 6H-SiC in many applications.

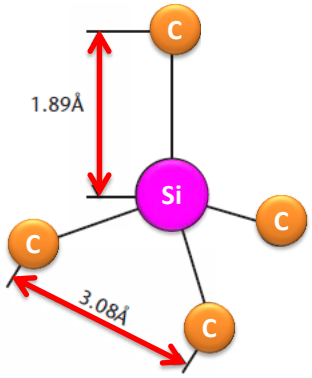

Figure 1.4 The basic unit of a silicon carbide crystal

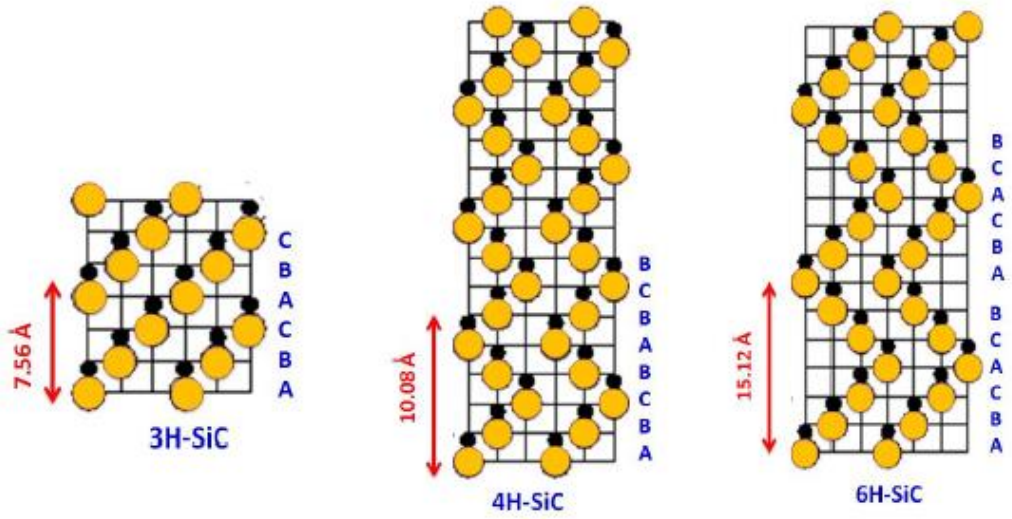

Figure1.5 The three most common polytypes in SiC viewed in the [1120] plane. From left to right 3C-SiC, 4H-SiC and 6H-SiC

Since the operation of any radiation detector basically depends on the way the radiation to be detected interacts with the detector itself, it is worthwhile to study these interactions before designing any detector. Therefore in what follows we briefly summarize these interactions before reviewing the SiC-based detectors.

1.5 Interaction of heavy charged particles with matter

Heavy charged particles (HCP) refers to those energetic particles whose mass is one atomic mass unit or greater. Alpha particles, protons, deuterons, and fission

fragments are all examples of heavy charged particles and they carry at least one electronic charge.

HCP such as alpha particles consist of two neutrons and two protons bound together into particle identical to helium nucleus. Generally alpha particles are emitted with several discrete energies through alpha decay, particularly from some natural radioactive nuclides such as americium ^{241}Am or plutonium ^{239}Pu. Since an alpha particle is relatively a heavy charged particle, it interacts strongly with matter, generating large number of ions along its track. Alpha particles are not very penetrative. For example a 5 MeV alpha particle passes only several millimeters in air before it stops and it doesn't penetrate an ordinary piece of paper.

Due to their positive charge, alpha particles interact mainly through Coulomb forces with the electrons of the target atoms. Charged particles detectors rely on this interaction for their response assuming elastic nuclear scattering is negligible. As the charged particle passes through any absorbing medium, it interacts with its orbital electrons. Thus the electron feels an impulse of the attractive Coulomb force as the charged particle passes its vicinity. The impulse could either raise the electron into a higher-laying shell within the absorber atom (excitation) or remove it from the atom (ionization). Ionization occurs when the energy given by the charged particle is sufficient enough to pull the electron out from its orbit through Coulomb force. The maximum energy transferred by a charged particle to an electron is $4Em_0/M$ where E and M are the kinetic energy and the mass of the charged particle respectively and m_0 is the mass of an electron [1]. Since a small percentage about 0.2 % of proton energy and about 0.05 % of alpha energy is transferred per interaction, thus a given charged particle undergoes many such interactions before it is stopped.

1.5.1 Stopping power

As the heavy charged particle passes through a given medium it starts to lose its energy until it is stopped, the rate of energy loss or the "linear stopping power" is given by:

$$S = -dE/dx \tag{1.1}$$

The energy loss of a charged particle with mass M >> m_0 is given by the Bethe-Bloch expression for stopping power [1] [25]:

$$\frac{-dE}{dx} = \frac{4\pi q^4 z^2}{m_0 v^2} NB \tag{1.2}$$

where B is the atomic stopping number given by:

$$B = Z\left[ln\frac{2m_0 v^2}{I} - ln\left(1 - \frac{v^2}{c^2}\right) - \frac{v^2}{c^2}\right] \tag{1.3}$$

where v and zq are the velocity and the charge of the incident particle respectively, Z and N are the atomic number and number density of the absorber atoms respectively. The parameter I is an experimentally determined quantity representing the average excitation and ionization of the absorber. For non-relativistic charged particles where $v << c$, only the first term of equation (1.3) is important and the Beth equation reduces to the following equation:

$$\frac{-dE}{dx} = \frac{4\pi q^4 z^2}{m_0 v^2} NZ\left[ln\frac{2m_0 v^2}{I}\right] \tag{1.4}$$

From equation (1.4) dE/dx varies as $1/v^2$ or it is inversely proportional to the particle energy. In other words, as the charged particle slows down the energy loss starts to be greater, this is because at low velocity the charged particle spends greater time in the vicinity of a given electron and thus a greater amount of energy is transferred to the electron. Also dE/dx is proportional to z^2 this means that particles with greater charge will lose more energy in a given absorbing medium. From Bethe formula it is clear that the energy loss doesn't depend only on the charge and the velocity of the incoming particle but also on the electron density of the absorber (NZ). Therefore high density materials results in the higher energy loss.

The Bethe formula is generally valid for different types of charged particles assuming their velocities remain large compared with that of the orbital electrons of the absorbing medium. Moreover this formula starts to fail at low particle energies where the positively charged particle becomes neutral after picking up z electrons along its path in the absorbing medium.

1.5.2 Range

The plot of the specific energy loss as function of distance travelled by a beam of incoming particle in the absorbing material is called Bragg curve. The maximum energy loss corresponds to the range of the particle in the material which is the distance it travels before coming to rest. The range R of a charged particle can be calculated by integrating over the energy loss along its path as follows:

$$R = \int_0^R dx = \int_0^E \frac{dE}{S(E)} \tag{1.5}$$

The range of a given incident charged particle depends not only on its energy and its charge but also on the density of the stopping medium. Using Bragg-Kleeman rule if the range of a given particle is known in one medium it can be estimated in another medium as follows:

$$\frac{R_1}{R_0} \cong \frac{\rho_0}{\rho_1}\sqrt{\frac{A_1}{A_0}} \tag{1.6}$$

where the subscripts 0 and 1 refer to different absorbing materials and R is the range, ρ and A are the density and the atomic weight of the absorbing medium respectively. The range of a given charged particle in a given absorbing medium is considered a crucial parameter for detector fabrication. For instance, in order not to reduce the detector efficiency, the distance between the starting-point of the charged particle and the sensitive volume of the detector should be less than the range such particles.

1.6 γ-ray interaction

The energies of electromagnetic radiations span orders of magnitude, from 10^{-6} eV to 10^{6} MeV. Photons are classified according to their mode of origin rather than their energy. For instance, x-rays are identical to gamma rays except that they are emitted during rearrangement of the atomic electron structure. However gamma rays are electromagnetic radiations emitted by nuclear transitions during radioactive decay or in nuclear reactions. When a nucleus is in excited energy level, goes back to ground level, it releases energy in form of gamma rays. Typically the natural range for gamma-rays emitted by nuclei is 0.01~10 MeV.

There are 12 different processes by which gamma can be scattered or absorbed such as Thomson scattering, Delbruck scattering or Meson production and others [25]. Many of these processes are infrequent. However the three main modes of interaction of gamma rays with matter are: photoelectric effect, Compton scattering and pair production. All these processes cause a partial or complete transfer of gamma energy into the electrons of the absorbent. Depending on the atomic number of the target and the energy of the incident γ-ray, different interactions may take place as shown in Figure 1.6. Being uncharged x-ray or γ-ray photons are invisible to the detector since they can't create direct ionization and excitation within the material they pass. Their detection relies on their interaction with the electrons of the absorbing material. These secondary electrons contribute to the output signal if they are properly stopped in the active region of the detector. In other words the design of any γ-ray or x-ray detector should promote these interactions and fully stop the secondary electron.

Understanding the way photons interact with matter is not only necessary for realizing γ-ray or x-ray detectors but also for neutron and charged particles detectors, particularly for applications where the signal from gamma should be discriminated from that of neutron interactions.

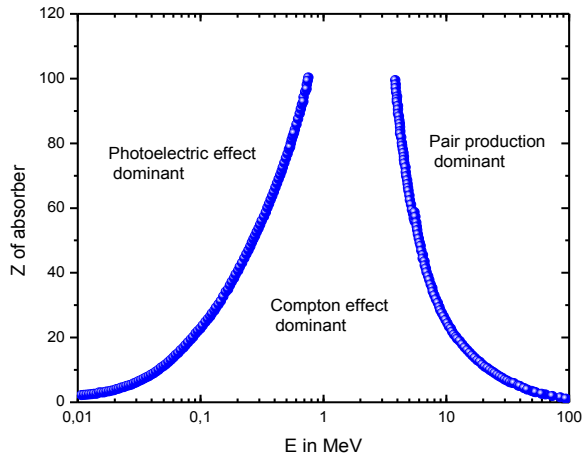

Figure 1.6 Relative importance of the three major types of interaction of γ-ray interaction. The two lines show the values of Z and E_γ at two which neighboring effects are equal [25] .

1.6.1 Photoelectric absorption

The photoelectric process becomes the predominant interaction as the gamma energy goes below 0.1 MeV. In this process the interaction takes place between the incoming photon and the absorber atom where the photon is absorbed. This total absorption of the photon takes place only if the electron is initially bond in an atom. As a result an electron is ejected from the atom with energy equal to the difference between the photon energy and the binding energy of the ejected electron. It was found that 80 % of the photoelectric absorption processes take place in the most tightly bond shell (K shell). A rough approximation of the probability of the photoelectric absorption per atom can be written as follows:

$$\tau \cong constant \times \frac{Z^n}{E_\gamma^{3.5}} \tag{1.7}$$

where n varies between 4 and 5. Equation 1.7 shows that the probability of a photoelectric absorption depends not only on the γ-ray energy but also on the atomic number of the absorbing material. This dependence is the main reason for using high-Z material such as lead for gamma shielding. Moreover the photoelectric

absorption is an ideal process for measuring the original gamma ray energy where it is equal to the total electron kinetic energy assuming no escape from the detector.

1.6.2 Compton scattering

Compton scattering is the predominant interaction in the entire region of intermediate γ-ray energy and for most values of Z. In this process, the γ-ray transfers part of its energy to the electron of the absorbing medium assuming they are initially at rest. As a result of this interaction the γ-ray deviates from its initial direction by an angle θ as shown in figure 1.7.

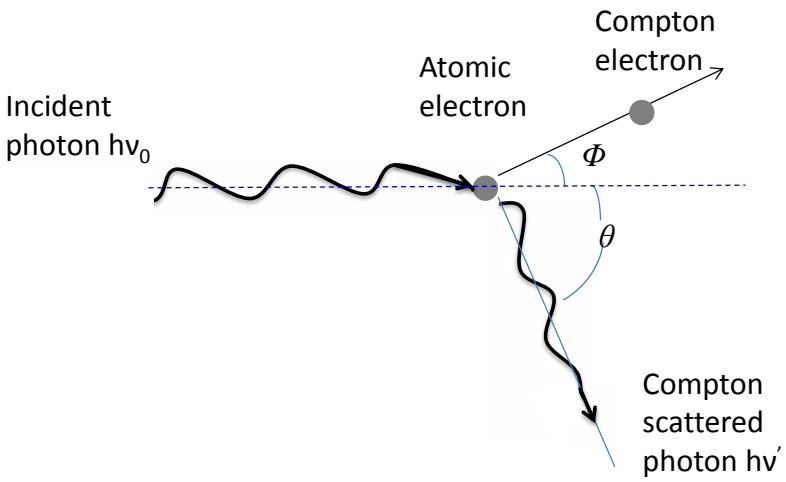

Figure 1.7 Compton scattering showing the incident photons with energy hv_0, the scattered photon is emitted with energy hv' and angle θ.

Using the conservation of momentum and energy the final energy of the γ-ray after interacting with electron can be written as follows.

$$E' = \frac{E}{1 + \frac{E}{m_0 c^2}(1 - \cos\theta)} \tag{1.8}$$

E and E′ are the initial and the final energy of γ-ray respectively, m_0c^2 is the rest-mass energy of electron (0.51 MeV)

1.6.3 Pair production

The pair production process becomes significant as the energy of the given gamma ray exceeds 1.02 MeV which is the energy required to create electron-positron pair.

This process must occur in the coulomb field of a nucleus. As a result of this process, the photon is completely absorbed and is replaced by an electron-positron pair. The electron-positron pair acquires kinetic energy if the incident gamma-ray energy exceeds 1.02 MeV this can be formulated as follows:

$$E_\gamma - 2m_0c^2 = E_{electron} + E_{positron} \tag{1.9}$$

The probability of pair production per nucleus is proportional to square of the absorber atomic number. This process is complicated since the positron will subsequently annihilate or combine with a normal electron in the absorbing medium.

1.7 Neutron interaction with matter

Neutron was first discovered by Chadwick in 1932. After ten years the first world's man-made nuclear reactor was constructed then neutron starts to play a significant role in the modern world of atoms and radiation. Neutrons can be found in tremendous amounts in nuclear reactors. Their energy can extend from few meV to several MeV, according to these values neutrons are classified into different categories. For example thermal and fast neutrons correspond to neutrons with energy about 0.025 eV and up to 10 MeV or 20 MeV respectively.

Neutrons like photons are uncharged therefore they can travel appreciable distances in matter without interacting. Depending on the energy of neutrons and the cross section of the used material, different interactions could take place. The two major types of interactions of neutron with matter are: scattering (elastic and inelastic) and absorption. In the latter case neutron is absorbed by a nucleus and a wide range of radiation could be emitted (such as gamma, proton, or alpha) or fission could be induced. However in the case of elastic scattering the total kinetic energy of the neutron and the target nucleus is conserved. The maximum energy transmitted by neutron of mass m to nucleus of mass M in a single head-on Collison is given by the following equation:

$$E_{max} = \frac{4mME_n}{(m+M)^2} \tag{1.10}$$

where E_n is the energy of a neutron. From equation 1.10 it is clear that using target nuclei with the lowest mass is preferable to reduce the neutron energy with few numbers of elastic collisions. That's why hydrogen is the proper moderator as the neutron loses all its energy in a single head-on collision.

Inelastic scattering is similar to the elastic scattering except that the nucleus is left in its excited sate. In this case the total kinetic energy is not conserved where a part of the neutron energy is used to place the nucleus in the excited state.

1.7.1 Thermal-neutron interaction

Being neutral neutrons cannot interact with matter through a Coulomb interaction which is the dominant mechanism through which charged particles and electrons lose their energy. Therefore mechanisms for detecting thermal neutrons are based on indirect methods where thermal neutrons interact with specific atomic nucleus to produce charged particles. Cross sections for the interaction of neutrons with atomic nuclei are complicated functions of neutron energy. Figure 1.8 shows the total cross sections for neutron interactions with boron, lithium and helium. The cross section for ^{10}B and ^{3}He is high compared to that of ^{6}Li in the low energy region. Table 1.2 lists the three most important nuclear reactions for thermal neutron detection [26].

The choice of the nuclear reaction that might be useful in the neutron detection depends on several factors such as the microscopic thermal neutron absorption cross-section, the Q-value of the reaction and the range of the charged particles in the target material. First the cross section for the reaction must be as large as possible in order to realize efficient detectors with small dimensions. The cross section decreases with increasing neutron energy, with dependence proportional to the inverse of the neutron velocity. Moreover, the Q-value of the reaction is also an important factor since it determines the energy liberated in the reaction following the neutron capture. The higher the Q-value is the greater the energy given to the reaction products and it is easier to discriminate them from gamma-ray events. The range of the produced charged particles has also important consequences on the design of the detector.

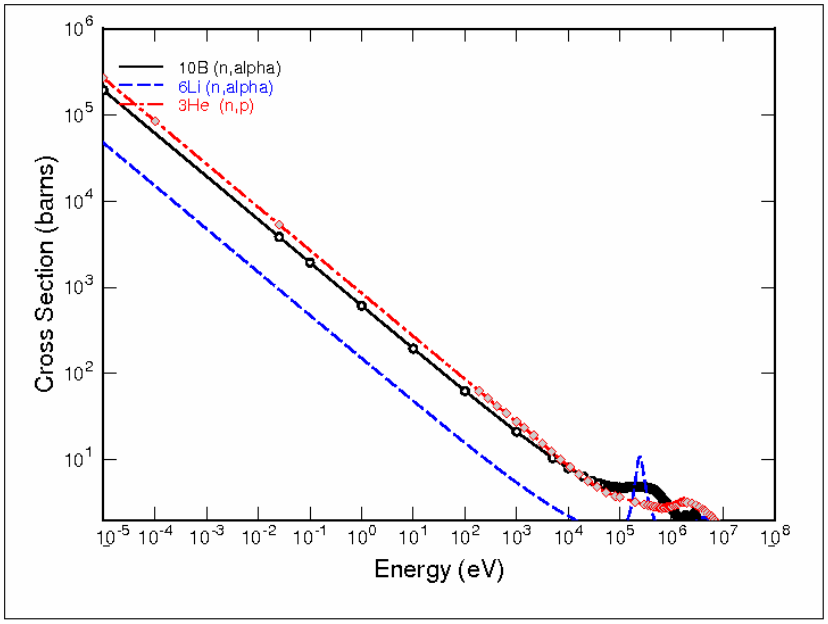

Figure 1.8 The total neutron cross section of ^{10}B and ^{6}Li as function of neutron energy. [27]

Table 1.2 The most used reactions for thermal-neutron detection

Reaction	Q-value (MeV)	Product Kinetic energy (MeV)	Cross section (Barns)	Natural abaundance (%)
$^{10}B + {}^{1}n \rightarrow {}^{7}Li^{*} + {}^{4}He$ (94%)	2.31	E_{Li}= 0.84 E_{He}= 1.47	3840	19.7
$^{10}B + {}^{1}n \rightarrow {}^{7}Li + {}^{4}He$ (6%)	2.79	E_{Li}= 1.01 E_{He}= 1.78		
$^{6}Li + {}^{1}n \rightarrow {}^{3}H + {}^{4}He$	4.78	E_{He}= 2.05 E_{H}= 2.73	940	7.42
$^{3}He + {}^{1}n \rightarrow {}^{3}H + p$	0.764	E_{3H}=0.191 E_{1H}=0.574	5330	1.3×10^{-4}

The most used neutron interactions for thermal neutron detection are $^{3}He(n,p)$, $^{10}B(n,\alpha)^{7}Li$ and $^{6}Li(n,\alpha)^{3}H$ reactions. As shown from table 1.2 for the reaction $^{10}B(n,\alpha)^{7}Li$ the cross section is 3840 barns for thermal neutrons which is higher than that for $^{6}Li(n,\alpha)^{3}H$ reaction (940 barns). This high cross section means high sensitivity of the detector to the incident thermal neutrons. The ^{10}B isotope is 19.7 %

abundant while the ^{6}Li is just 7.42 % abundant. The higher Q value for the $^{6}Li(n,\alpha)^{3}H$ reaction makes this reaction more favorable for better gamma-ray discrimination. Proportional counters with boron trifluoride gas (BF_3) or with ^{3}He are most widely used for thermal neutron detection and lithium scintillators are frequently used for detecting thermal neutrons.

1.7.2 Fast-neutron interaction

As the energy of the neutrons increases reaching the fast neutron region the probability of most neutron-induced reactions decreases. However, the importance of scattering becomes important. Typically fast neutrons lose energy in matter through elastic scattering. However if their energies are sufficiently high inelastic scattering could take place where the recoiled nucleus is elevated to one of its excited states. Following each scattering event the neutron loses its energy and then it is moderated or slowed to lower energy. Typically hydrogen is the most efficient moderator where the neutron can lose all its energy in a single collision with a hydrogen nucleus. The response of fast neutron detectors rely on scattering process where the recoiled nucleus is detected revealing the presence of fast neutrons.

After reviewing the way different types of ionizing radiations interact with matter, we will summarize the way different SiC-based radiation detectors are realized and characterized as we will see in the following sections.

1.8 SiC radiation detectors:

Generally solid state radiation detectors are based on semiconductor materials. Such detectors are based on the use of p-n junction or Schottky diode where the active region of the detector is its depletion region also called the space charge region (SCR). Depending on the external applied reverse bias the active region could be enlarged leading to more collection of charge carriers. As the ionizing radiation interacts with the detector materials electron-hole pairs are created which then pulled apart thanks to the influence of the electric field. Consequently a current is created which is then amplified and recorded.

The best p-n or Schottky diodes are those with low leakage current density order of pA/cm^2 which reveals the high signal-to-noise ratio. The high leakage current is the

main restriction of the uses of silicon detectors at high temperature and germanium at room-temperature. As an alternative to such conventional semiconductor, silicon carbide (SiC) has been developed as alpha particle, beta, UV, X-ray detectors, and as radiation detectors in harsh environments [11] thanks to its wide band gap (3.26 eV), high radiation resistance and high thermal conductivity (4.9 W/cm.K).

1.8.1 SiC-based α-detectors

SiC has been used to manufacture different radiation detectors for monitoring neutron fluxes in nuclear reactors since several years. Babcock et al [28] were first to study the response of SiC diode to alpha radiation; even without an applied bias voltage they demonstrated the detection of alpha particles. The development of SiC radiation detectors was renewed by Tikhomirova et al. [29] in 1972, where a 6H-SiC p-n junction doped with beryllium with low leakage current was used as radiation detector.

Further developments of these detectors were limited by the lack of availability of high quality of SiC materials at that time. However the improvements in the crystalline quality of SiC materials renewed the interest in SiC radiation detectors. Using high-quality 4H-SiC epitaxial layer Ruddy et al. [30] were first to realize and test pn and Schottky diodes as alpha detectors with 400 and 200 μm diameters. For Schottky diode, Ni was used as a Schottky contact over the 4-8 μm n-epitaxial layer (with nitrogen dopant 10^{15} cm^{-3}) and as a back ohmic contact. For the p^+n diode, the n-layer was covered with a 1μm p^+ layer. Both types of detectors show robust responses to alpha radiation without applying any external bias voltage. The alpha signal was separable from the gamma signal and no significant change was observed at 90 °C. Similarly gold contact 4H-SiC schottky diode with 2 mm diameter have been realized using 30 μm n-epitaxial layer with net doping concentration ~$10^{15}cm^{-3}$ [31]. The charged particle detection properties have been evaluated using ^{241}Am as an alpha source. Even without applying external bias voltage robust signal was obtained with linear charge collection efficiency as function of the square root of the reverse bias.

Since SiC Schottky diodes with nickel as a Schottky contact showed limitation to temperatures lower than 300 °C it was necessary to study the possibility of realizing SiC detectors using another method. Beside Schottky diodes, detectors based on ion

implantation of aluminum into SiC in order to realize the p+ layer were fabricated and proved their reliability by their low noise level obtained even at elevated temperature (300 °C) [32][33] and their response was not affected at such temperature. This proves the reliability of this method if the process is properly annealed and doesn't worsen the performance of the detector which could lead to full charge collection.

The performance of radiation detectors is generally determined by the charge collection efficiency (CCE) and the full width at half-maximum (FWHM). The CCE is defined as the detected charges over the charge introduced by a detected particle. However the FWHM determines the energy resolution capability of the used detector. The low CCE may reveal the presence of charge-trapping centers which lead to the degradation of the detector which is also estimated by the high FWHM indicating worse resolution. The CCE was an indication of the improvement of the characteristics of p-n detector initially irradiated by 8 MeV protons at a fluence of 6×10^{14} cm^{-2} after heating up to 140 °C [34]. Moreover the low FWHM and the high CCE have confirmed the possibility of using p-n detectors at elevated temperature [32]. The CCE could attain its saturation at high reverse bias voltages which is related to full charge collection.

1.8.2 SiC-based gamma and x-ray detectors

For more than 50 years Ge-based detectors have been used for gamma-ray detection. As it is known, gamma-rays are more penetrative than other types of radiations requiring the use of detectors with thick active region up to several centimeters. In addition to the thick active region which was attained by high purity germanium (HPG) or lithium-drifted (Ge (Li)), the excellent energy resolution of Ge detectors over other scintillators for gamma-ray spectroscopy makes it a preferable material for decades. Despite its high energy resolution, Ge is classified as conventional semiconductor with low band gap (0.7 eV) this explains the impossible use of such detector at room-temperature due to the high leakage current. This requires the use of the cryostat for cooling the detector down to 70 K avoiding the high noise level at room-temperature which requires additional power, cost and place.

All the above-mentioned limitations for using Ge-based detectors have pushed to look for alternative semiconductor where no cooling systems are needed. Therefore the use of wide band gap semiconductors such as SiC thanks to its ultralow dark current allows its use at high-temperatures without cooling systems. Moreover the x-ray spectroscopy is the most challenging domain. This is because x-rays typically generate small electric signal requiring ultralow leakage current to obtain high signal-to-noise ratio.

Several works have confirmed the possibility of using SiC as x-ray spectroscopy with high-energy resolution dedicated for high temperature applications up to 100 °C [35][36][37]. Although SiC materials offer many advantages for radiation detection applications, there still some limits for this material for x-ray detections: the main limitation is related to the relatively thin active regions in the order of 100 μm.

Furthermore other works confirmed the tolerance of SiC-based detectors to high gamma doses. This was demonstrated by Ruddy et al. [38] where SiC detector maintains most of its initial energy spectrometry capabilities, after its exposure to high gamma doses up to 5.445 MGy, whereas Si radiation detectors show severe changes in their response after exposure to a lower gamma doses (0.01 MGy). Even higher gamma ray doses have been used where a 4H-SiC Schottky diode responses to alpha particles was unchanged by such huge dose of gamma (22.72 MGy) [39]. Also detectors based on SiC p-n structure showed no change in the CCE with gamma and beta irradiation up to 2.5 MGy and 2 MeV respectively [40]

It seems annoying that SiC with relatively thin active region and low Z material to be not so sensitive to gamma detection, however thanks to these properties the main task of discriminating gamma signal from neutron is likely possible using the pulse height discrimination techniques [41]. However if it is desired to increase the sensitivity of SiC to gamma irradiation this could be achieved by depositing a layer enriched with platinum on the top of SiC Schottky diode [42].

1.8.3 SiC-based neutron detectors

Beside its use as a charged particle detector, SiC has been also used to detect neutrons (fast and thermal). This wide interest in SiC as a radiation detector is attributed to its wide band gap, high radiation resistance and high thermal

conductivity. The first SiC neutron detector was demonstrated many years ago where such a detector showed its reliability up to 700 °C. Further work by Ferber et al. [43] with p-n SiC diode coated with ^{235}U showed a linear response to power reactor under thermal neutron fluxes. Furthermore the effect of thermal neutron damage on ^{235}U-coated detectors was studied by Tikhomirova in 1973. The detector showed a resistance to radiation damage up to 6×10^{13} n/cm^2 however a dramatic change in response beyond this fluence was obtained, which may be attributed to high dose of produced fission-fragments (10^8 cm^{-2}).

For fast neutron detection (E_n > 1 MeV), in this energy range neutrons interact primarily with Si and C atoms through elastic and inelastic scattering. Consequently ionizing particles (neutrons, protons and alpha particles) and recoiled Si and C ions are created within or close to the detector active region. Typically the response of the detector relies on the ionizations from these reaction products. Since the most abundant Si and C isotopes in SiC are: ^{28}Si (92.23 %) and ^{12}C (98.90 %), the reactions with these isotopes are considered dominant. Although similar reactions could take place with the less abundant isotopes, we list the most prevalent fast-neutron interactions with SiC as follows:

$$^{28}Si + n \rightarrow {}^{28}Si + n'$$
$$^{12}C + n \rightarrow {}^{12}C + n'$$
$$^{28}Si + n \rightarrow {}^{28}Al + p$$
$$^{12}C + n \rightarrow {}^{12}B + p$$
$$^{28}Si + n \rightarrow {}^{25}Mg + {}^{4}He$$
$$^{12}C + n \rightarrow {}^{9}Be + {}^{4}He$$

Typically the response of fast neutron detectors is based mostly on the above-mentioned reactions. Many SiC fast neutron detectors have been realized based on either p-n junction or Schottky devices [44][45] [46]. The sensitivity to fast neutron detection can be enhanced by juxtaposing a neutron converter layer with high concentration of hydrogen. A 100 μm polyethylene converter foil placed close to Schottky diode, can remarkably increase the neutron sensitivity [47]. This is explained by the high cross section of hydrogen with fast neutrons which generates protons according to the following reaction:

$$^{1}H + n \rightarrow {}^{1}H + n'$$

The produced protons create ionizations which in their turn increase the detector response.

Typical pulse height spectra of SiC to different fast neutron sources (^{252}Cf (2.15 MeV), ^{241}Am-Be (4.5 MeV) and D-T (14 MeV)) are shown in reference [48]. These spectra were obtained using a SiC Schottky diode with 10 μm active region at -80V. While using a detector with higher active volume [45] (90 μm obtained at -900V) results in higher response particularly if the projected range of the neutron-induced recoil ion is less than the width of the active region. Even though with the use of 90 μm thick sensitive region has increased the response, a thicker region is required to obtain more response peaks from different fast-neutron reactions especially for obtaining clearly the (n, p) reaction peaks.

Furthermore the use of the detectors in harsh environments requires the radiation hardness of the detectors under these irradiations. Neutron creates more damage with respect to other types of irradiations. Such damage may cause the degradation of the performance of the detector. It was found that the CCE of the 4H-SiC Schottky diode has been decreased by 1.3 % after neutron irradiation with energy of 1.42 MeV and up to 8.26×10^{14} n/cm^2 [49]. Additionally, in another work [50] it was shown that the leakage current of p+n diodes remains very low even after irradiated with neutrons 1 MeV up to 10^{16}cm^{-2}. However lower fluences of order of 3×10^{15} cm^{-2} causes remarkable decrease in charge collection. However annealing up to 200 °C may slightly recover the damage after neutron irradiation 10^{14} n/cm^2 [51].

As far as the thermal or epithermal neutron detections are concerned, a neutron converter layer (NCL) is crucial to enhance the neutron detection. As mentioned previously the choice of a NCL is based on some parameters mainly on the Q-value, and the thermal-neutron and epithermal-neutron cross section of the material used in the NCL.

As it is clearly shown in the following figure1.9 that the cross sections of ^{6}Li and ^{10}B in the low energy region (10^{-5} eV < E_n <10^{3} eV) are much higher than that of Si and

C atoms. Consequently using NCL with such material will remarkably enhance the response of a SiC detector.

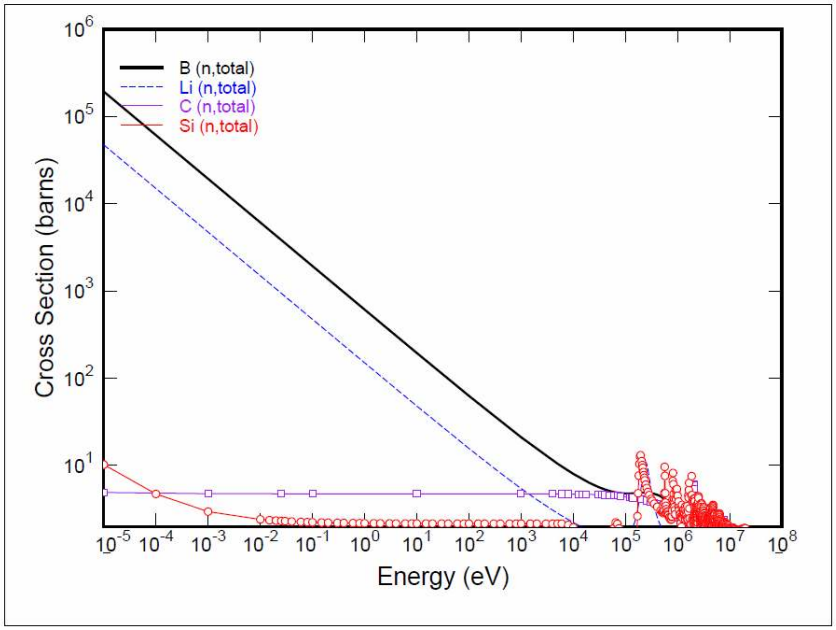

Figure 1.9 Variation of the total neutron cross section of ^{10}B, ^{6}Li, ^{12}C and natural Si as function of neutron energy [27]

One of the principles for monitoring thermal neutrons is based on detecting ionizing particles that are created as a result of nuclear reactions between thermal neutrons and specific isotopes such as ^{10}B and ^{6}Li. Moreover, the thermal neutron absorption cross section of ^{10}B is 3840 barns, leading to higher reaction probability than ^{6}Li (940 barns).

Specifically, thermal neutrons with energy of 0.025 eV interact with ^{10}B resulting in production of alpha particles and lithium ions and interacting with ^{6}Li resulting in the production of alpha particles and tritons, which are released in opposite directions according to the following reactions with different probabilities:

$$\begin{cases} {}^{10}B + n \rightarrow {}^{7}Li + {}^{4}He \ (Q = 2.72 \text{ MeV}) & 6\ \% \\ {}^{10}B + n \rightarrow {}^{7}Li^{*} + {}^{4}He \ (Q = 2.31 \text{ MeV}) & 94\ \% \end{cases}$$

$$^{6}Li + n \rightarrow {}^{3}H + {}^{4}He \ (Q = 4.78 \text{ MeV})$$

The produced charged particles generate electron-hole pairs as they lose their energy by Coulomb scattering. A rectifying junction has to be created aiming to harvest the carriers thanks to the corresponding electric field.

SiC thermal neutron detectors have been realized based on juxtaposing ^{6}LiF as a neutron converter layer (NCL) on small SiC Schottky diodes (200-400 μm diameter) [52][53], a linear counting rate with respect to the thermal neutron fluence rate was obtained. Aluminum foil was introduced between the detector and the NCL to reduce the damage within the active region which is primarily caused by the produced alpha. Moreover the thermal neutron response was unchanged by a previous irradiation to fast neutron up to 1.3×10^{16} cm^{-2}. This is again one of the advantages of SiC-based detectors that are dedicated for thermal neutron detection in an environment where fast neutrons are present.

On the other hand larger area SiC Schottky (20 mm^2) neutron detectors have been tested [54] based on the 100 μm external ^{6}LiF-based NCL. The neutron response was clearly resolvable from that of gamma, ensuring the reliability of using SiC-based detectors in environments where gamma-rays may exist [30][55]. Additionally another neutron detectors were realized [56][57] based on evaporation of ^{6}LiF and $^{10}B_2O_3$ onto the Au metal contact**.** Such detectors showed charge collection efficiency of over 80 % at self-biased voltage.

After reviewing the way different thermal-neutron detectors are realized, it is worthwhile to mention the novelty of our work. The main purpose of the present work is to demonstrate for the first time the reliability of new methods of realizing thermal neutron detectors. Such methods are based on ion implantation of ^{10}B in order to create the NCL and sometimes to create both the p+ junction and NCL in one process. In the following chapters we will show in detail the technological processes followed to fabricate such detectors, with a study of their electrical behavior and their responses under thermal neutron irradiations

In summary, the fabrication of semiconductor radiation detectors requires a number of critical steps. Typically the purity physical and electrical properties of the used semiconductor material are important parameters. In addition, for thermal neutron detection, additional requirements should be satisfied such as the high thermal-neutron cross section of a given material. Also the thickness of the used NCL should

be less than the projected range of the produced charged particles (charged particles that are generated as a result of the interaction between neutrons and NCL). Figure 1.10 summarizes the projected ranges of the produced charged particles (alpha, lithium and tritium) from different reactions. The ^{3}H ions are more penetrative in SiC than ^{7}Li and alpha particles.

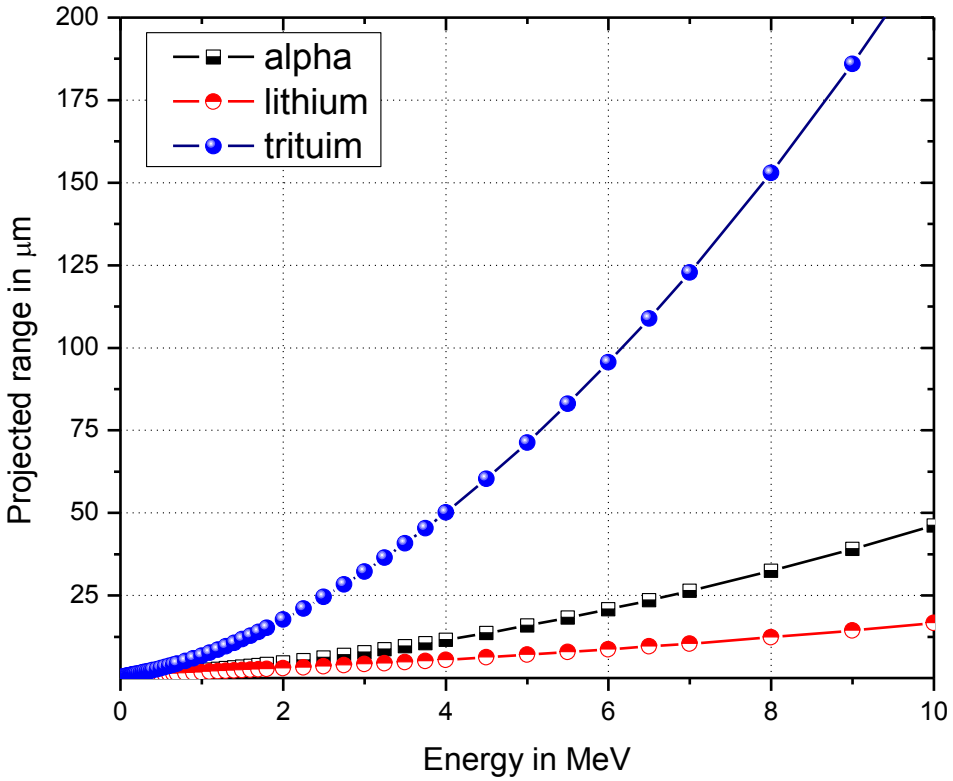

Figure 1.10 The projected range in SiC for different charged particles generated from $^{10}B(n, \alpha)^{7}Li$ and $^{6}Li(n, \alpha)^{3}H$ reaction as function of their energies in MeV.

Chapter 2. Simulation of the Detectors' Parameters

In this chapter we will explain what a basic unit of a semiconductor detector is, which is generally either a Schottky device or a p-n junction. Moreover we will list what techniques are used to develop such a device. This will be achieved by reviewing the theory of ion implantation techniques. In addition we will show the results of SRIM (Stopping and Range of Ions in Matter) simulations, which were performed in order to choose the proper parameters concerning the energy and the dose of the implanted species, required to obtain high ionization rates and to minimize the accumulation of damages within the active volume of the detector.

2.1 p-n junction

As previously explained in chapter one, most of the semiconductor detectors are based on either Schottky or p-n devices. Although in principle the Schottky barrier structure is easier to fabricate, the pn-junction is more suitable for high temperature applications because of its lower leakage current. Since our detectors are dedicated to high temperature application hence they are based on pn devices. In what follows a review of what a pn junction is and how it is constructed. Moreover the effect of an applied bias voltage on increasing the charge collection efficiency of some radiation detectors will be addressed.

A pn junction is created by juxtaposing regions with different doping types, one p-type and the other is n-type doped. A p-n device serves an essential role in modern electronic applications. It is used extensively in rectification and in other operations in electronic devices. It is also a key building block for many semiconductor devices.

In order to understand the operation of a pn junction, one may first imagine that both sides of the junction are originally separated, see figure 2.1 (a). Then a pn junction is constructed by connecting the p-type to the n-type region. The energy band diagrams of both cases (separated and connected) are also shown in figure 2.1.

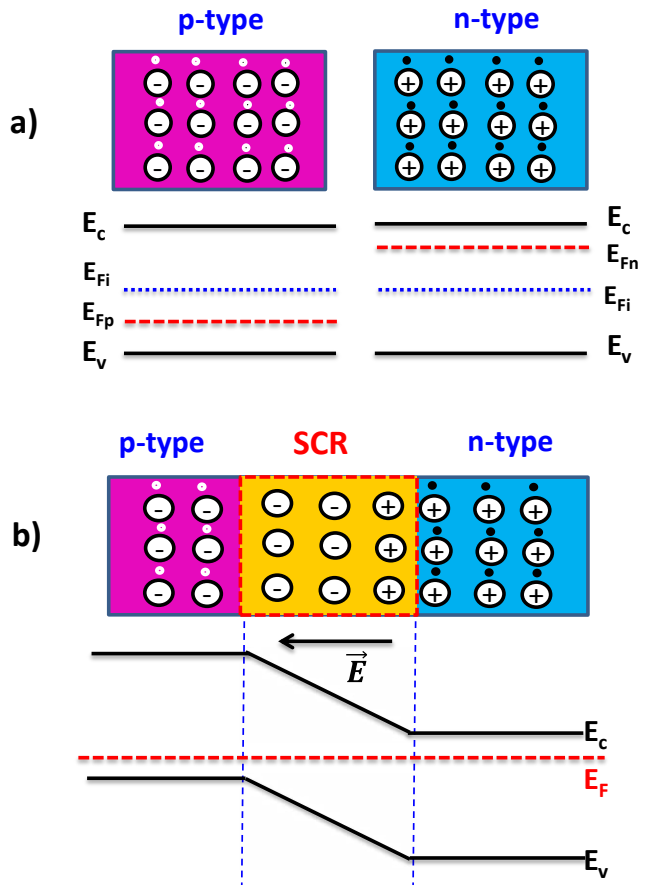

Figure 2.1 Pn junction separated (a) and in contact (b) with their corresponding energy band diagram

As the junction is constructed electrons diffuse from electron-rich region (n-type) to electron-poor region (p-type), similarly holes diffuse from p-type region into n-type region. Electron and hole that meet at the junction will recombine and as a result both will vanish. Consequently the donor and the accepter ions in the neighborhood of the junction lose their mobile carriers (electrons and holes). Thus a region depleted of mobile carriers is formed. This region is called depletion region or

the space charge region (SCR). In fact this region is the active region of a radiation detector since the charge carriers created in this region can be quickly and efficiently collected. The thickness of the SCR depends on the doping concentration on both sides. For instance if one of the junctions is less doped than the other one, the SCR extends further in the lightly doped side.

Since the p-side of the SCR is negative and the n-side is positive an electric field is established across the depletion region. This electric field is determined by charge distribution through the Poission's equation. Due to the presence of the electric field an internal built-in potential (V_b) is formed without any external bias voltage at the junction which can be formulated as follows:

$$V_b = \frac{K_B T}{q} \, ln\left(\frac{N_A N_D}{n_i^2}\right) \tag{2.1}$$

where N_A and N_D are the acceptor and the donor concentrations respectively. n_i is the intrinsic carrier concentration, K_B ,T and q are respectively the Boltzmann constant (1.38 $\times 10^{-23}$ J/K), the temperature and the electron charge respectively. Where $K_B T/q$ = 0.0259 V at 300 K.

As function of the built in potential the SCR width (W) is given as follows:

$$W = \sqrt{\frac{2\varepsilon_r \varepsilon_0}{q}\left(\frac{N_D + N_A}{N_D N_A}\right)(V_b + V_R)} \tag{2.2}$$

where ε_r is the dielectric constant of 4H-SiC (10.03) and ε_0 is the permittivity of vacuum (8.85$\times 10^{-12}$ F/m). V_R is the applied reverse bias and V_b is the built-in potential given by equation 2.1, the intrinsic carrier concentration of SiC, n_i is 1.3$\times 10^{-8}$ cm^{-3}, N_A and N_D are the acceptor and the donor concentrations respectively. Based on the donor and the acceptor concentrations the SCR extends further into either the p-side or the n-side. For instance the depletion region widths on the p-side (W_p) and n-side (W_n) are given as follows:

$$W_p = \frac{N_D}{N_D + N_A} W \tag{2.3}$$

$$W_n = \frac{N_A}{N_D + N_A} W \tag{2.4}$$

These equations explain the extension of the SCR further in the n-side for lightly doped n-region with respect to the p-type. Moreover the width of the depletion region is strongly dependent on the applied bias voltage; a forward bias voltage shrinks the width of the SCR while a reverse bias voltage results in a wider SCR.

Under irradiation the electron-hole pairs created within the SCR are swept out thanks to the electric field and hence their motion results in the output electrical signal. Typically an external reverse bias voltage is applied to the detector thus enlarging the electric filed and hence causing the charge carrier to move faster. Generally this will increase the charge collection efficiency of a semiconductor detector.

When a reverse bias voltage is applied to a pn junction, a small current of the order of nA is obtained. The origin of this leakage current is due to two mechanisms. The first is due to the diffusion of the minority carriers across the junction. The thermal generation of electron-hole pairs within the depletion region also contributes to the observed reverse current. Due to the internal electric field within the SCR the electrons and holes are separated and drifted away. Consequently a second current due to drift is obtained in addition to the current due to diffusion of minority carriers. Obviously such current increases with the volume of the SCR and could be reduced by cooling down the material. This is one of the main limitations of using germanium detectors at room temperatures due to its high thermal generation.

Assuming τ_g is the mean time to generate an electron-hole pair by thermal vibration of the lattice; in other words τ_g is the mean thermal generation time. The total reverse current density can be formulated as follows:

$$J_{rev} = J_{diffusion} + J_{generation}$$

$$J_{rev} = \left(\frac{qD_p}{L_p N_D} + \frac{qD_n}{L_n N_A}\right) n_i^2 + \frac{qWn_i}{\tau_g} \quad (2.5)$$

where L_n and D_n are the electron diffusion length and diffusion coefficient respectively similarly for holes. From equation 2.5, the reverse current appears to be predominantly controlled by the intrinsic carrier concentration (n_i). Since n_i depends strongly on $\exp(-E_g/2K_BT)$, thus the reverse current is strongly controlled not only by the temperature (T) but also by the energy band gap (E_g) of the used semiconductor. In other words the use of wide band gap ensures the lower leakage current which is an important parameter in realizing detectors. Generally the leakage current tends to obscure the small signal current that is a result of the ionizing event caused by any type of radiation also will cause a significant source of noise in many cases.

2.2 Ion implantation

After describing the basic unit of a detector it is worthwhile to understand the techniques used to realize such a device. Since SiC is a IV-IV compound semiconductor, its n-type doping is achieved by using group-V atoms while for p-type doping group-III atoms are used. Nitrogen and phosphorous are the most commonly used donors while Al and B are the major acceptor impurities into SiC. Both Al and B are considered as 'shallow" acceptors in SiC and substituting for Si lattice sites [58]. The ionization energies for Al and B are ~ 200 meV and ~300 meV in 4H-SiC respectively [59][60].

There are several methods that can be followed to fabricate several planar electronic devices. These techniques are used to introduce doping atoms by ion implantation, plasma immersion ion implantation, neutron doping or diffusion. The latter was mainly used for impurity doping until the early 1970s. However because of the extreme stability of SiC and the small diffusion coefficient of most impurities into SiC at temperatures lower than 1800 °C, it is not feasible to dope it by thermal diffusion as is commonly used in silicon processing [61]. At such high temperatures it is difficult to find a mask that is suitable for doping by diffusion. On the other hand, neutron doping is also used for low doping concentration and high uniformity. This is attained by submitting the wafer to be doped to a neutron fluxes in a nuclear

reactor. For example some Si atoms from a Si wafer are transmuted into P according to the interaction of neutron with Si and thus doping is achieved.

Despite the wide variety of methods used for doping, ion implantation technique seems to be more effective and reproducible where the dopant concentration and profile are accurately controlled. Therefore this method became the method of choice for realizing different integrated circuits.

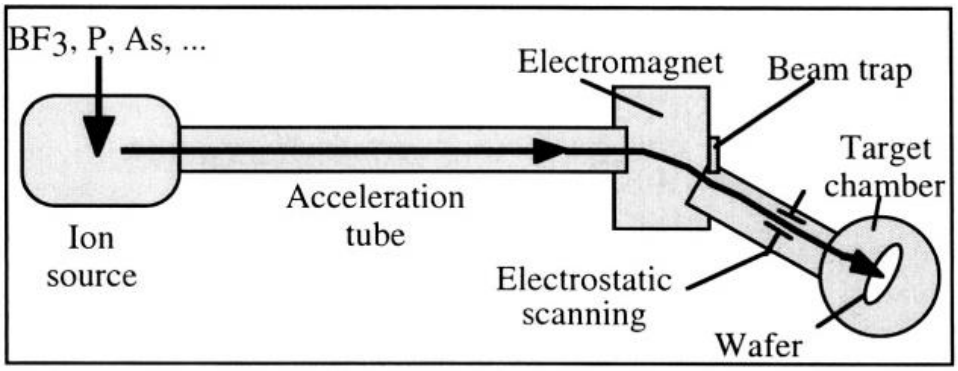

Figure 2.2 Schematic of an ion implanter

Ion implantation is the introduction of energetic charged particles into a given substrate such as SiC. It is a method used to dope the semiconductor to create p-type or n-type regions. Figure 2.2 shows schematically an ion implanter. First the ion source is heated and hence the used source gas (such as BF_3) is broken up into charged ions (such as B^+). A voltage is applied to move the charged ions out of the ion-source chamber. Then the charged ions move into a mass analyzer where a magnetic field exists. The magnetic field is chosen such that only the desired ions with specific mass-to-charge ratio are free to pass through it without being filtered. Consequently the selected ions are accelerated to the required implantation energy and then directed at a given substrate. Typically the implantation energy ranges between 10 keV and 1 MeV and the number of implanted ions in 1 cm^2 which is known as the dose can vary from 10^{12} ions/cm^2 to 10^{18} ions/cm^2. The ion dose can be controlled by adjusting the ion current during ion implantation.

As the implanted ions enter the crystal lattice several collisions take place with the target atoms until finally they come to rest. Elastic collision with the nuclei and inelastic collision with electrons in the target occur depending on the energy and the

atomic number of the implanted ions as illustrated in figure 2.3. At low energies the nuclear stopping dominates until some intermediate energy. It is known that heavier ions lose more energy per unit distance than lighter ions. As the ion energy is higher the nuclear stopping becomes weaker with respect to the electronic stopping. This fact is due to the insufficient time for the incoming swift particle to interact with the target atoms. At very high velocity the Bethe-Bloch stopping formula applies which was explained explicitly in chapter one.

Both the electronic and the nuclear stopping are regarded as being independent from each other. Thus the total energy loss per unit path length is the sum of the energy loss through collisions with electrons and nuclei. This expression can be written as follows:

$$\frac{dE}{dx} = \left(\frac{dE}{dx}\right)_{nuclear} + \left(\frac{dE}{dx}\right)_{electronic} \tag{2.6}$$

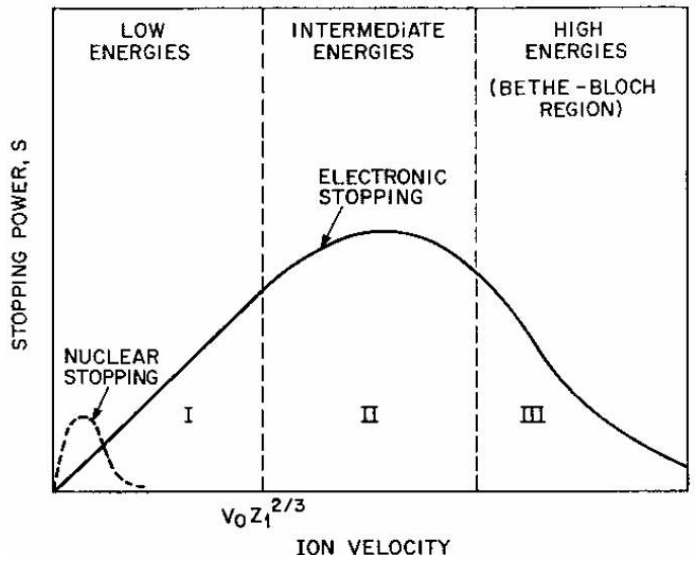

Figure 2.3 Nuclear and electronic components of the ion stopping power as function of ion velocity. The quantity v_0 is the Bohr velocity [62]

The rate at which a charged particle loses its energy determines the distance it travels. After the energetic ions lose all their energy they come to rest at some depth

within the lattice. The total distance the ion travels is called range while the projection of this distance on the axis of the incidence is called the projected range R_p as shown in figure 2.4. Since a beam of ions enter the target not all of them will rest at the same depth there is a fluctuation from the projected range which is known as range struggling.

Typically during ion implantation the target is tilted by a small angle with respect to the beam of ions in order to minimize the ion channeling effect [63]. The latter is not a favorable event where the implanted ions come to rest deeper than the predicted range with an exponential tail in the doping profile. Channeling occurs when the implanted ions are guided between rows of atoms in the crystal where the channeled ions experience low electronic and nuclear energy loss. Thus channeling implants results in a reduced damage.

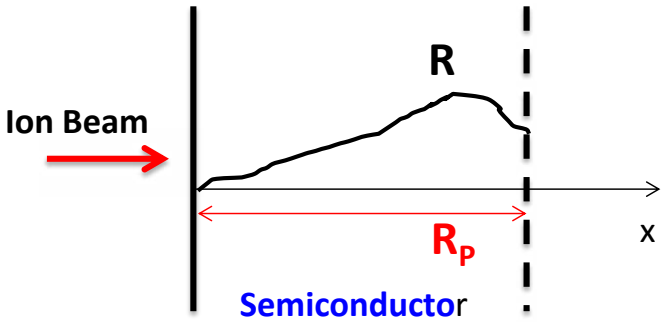

Figure 2.4 Schematic representation of the ion range (R) and the projected range (R_P)

2.3 High temperature implantation and annealing

Although ion implantation is one of the ideal methods for introducing dopants in a semiconductor, the major drawback of this method is the induced damage after the ion implantation process. This damage could range from point defects to a complete amorphization at high doses. This is explained by the nuclear collisions between the implanted ions that enter the semiconductor substrate and the target nuclei, resulting

in a sufficient energy which is transferred to the lattice causing the displacement of the atoms from their original positions. Moreover the displaced atoms may require enough energy hence they in turn cause cascades of secondary displaced atoms. If the density of the displaced atoms approaches the atomic density of the used semiconductor, the material becomes amorphous.

In addition to the damage created by the implanted ions, these ions occupy interstitial sites after the implantation and they are not electrically activated. Therefore to reduce the damage and to activate the dopants, post implantation annealing of the implanted sample should be performed at temperatures as high as 1700 °C. Moreover for optimum implant dopant electrical activation during post implantation annealing, it is necessary first to avoid the amorphization during implantation, this can be achieved by implanting at elevated temperatures. It was found that SiC implanted by Al at room temperature at high-fluence (2×10^{15} cm^{-2}) could not be recrystallized even after annealing at a temperature as high as 1700 °C, which is not the case for those implanted at temperature higher than 200 °C [64]. Therefore heating the SiC target during implantation to enough high temperature especially for high fluences, could repair partially or completely the damages as they are produced due to the self-annealing process [64].

The annealing conditions depend on the target and the implanted species. For instance the post-implantation annealing for Al and B acceptors occurs at higher temperatures (1600-1700 °C) with respect to N and P donor ions where lower temperatures (1200-1500 °C) are enough to obtain reasonable activations [65]. Different dopant impurities cause different disorder accumulation which increases with ion mass and ion dose [66] but decreases with the ion implantation temperature [67]. In general, this atomic disorder increases with a sigmoidal trend with the used ion doses and decreases with the implantation temperature due to simultaneous damage recovery processes. This is because when implanting at high temperatures, the point defects created by this process migrate, recombine and annihilate with a fast rate causing a reduced damage accumulation. Moreover it is possible that these implant-induced point defects can also aggregate to form stable defect clusters which need much higher temperatures to be annealed.

2.4 Plasma immersion ion implantation

Plasma immersion ion implantation (PIII) was first used in 1963 at the Shockley Laboratory for doping Si [68]. Furthermore PIII is a technology which is widely investigated for shallow junction doping beyond 0.15 μm and for low cost implantation. As we shall see in the following section, this technique has been used in this work to realize a shallow p+ layer of orders of nanometers.

The principle of PIII is illustrated schematically in figure 2.5. The sample under treatment is placed on a sample holder in a vacuum chamber. This sample is biased with a pulsed negative voltage. By means of an efficient ionization source the plasma is generated. When the sample is negatively biased the ions from the plasma are accelerated and implanted into the sample from all sides simultaneously. Typically the used dose-rates and the ion implantation energies in PIII ranges between 10^{15} to 10^{16} $cm^{-2} \cdot s^{-1}$ and from 10 eV to 100 keV respectively [69].

This technique is preferable for economic considerations, high dose rate and large area treatment. Some drawbacks concerning this method are the problems of the absence of mass analysis and hence the possibility of contamination. However in the case of conventional ion implantation the control of the dose and the implanted ions energy are the most important features of this process.

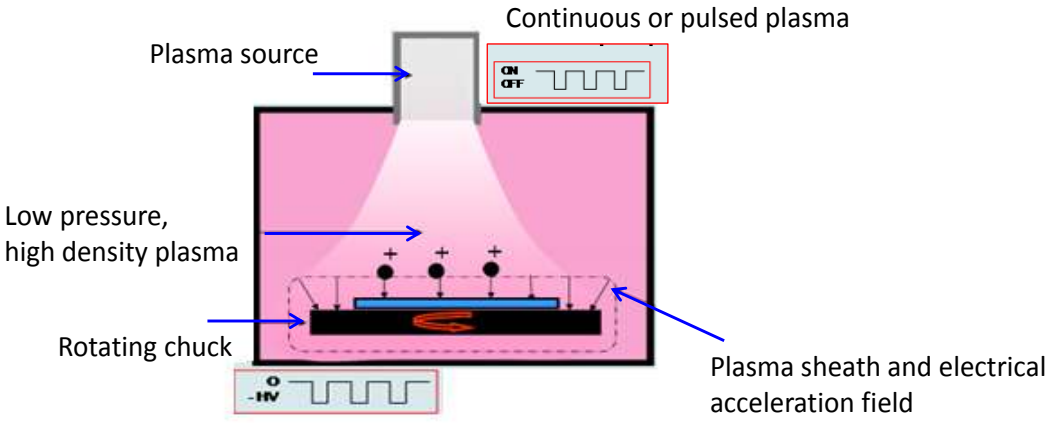

Figure 2.5 Schematic representation showing the principle of the PIII

2.5 Stopping and range of ions in matter

After reviewing the way the implanted ions lose their energy in the target, and how nuclear collisions correspond to the displacement of atoms from their lattice site, and how electronic stopping corresponds to either excitation or ionization. It should be pointed out here that also the mass of the implanted ions play an important role in determining the accumulated damage in the target crystal. In order to realize a detector and to choose the proper energy and depth of an implanted species, SRIM (Stopping and Range of Ions in Matter) has been used to compute the stopping and the range of ions.

This simulation code has been introduced by F. Ziegler et al. [70] in 1985 and it can be downloaded from the Web [71]. SRIM is a Monte Carlo computer program which calculates the interactions of energetic ions with complex targets made of compound materials with different layers. In the present work SRIM has been used to estimate the profile of implanted species such as Al and B into SiC substrates. It has been used to estimate the distribution of the ionizations and vacancies produced by different charged particles such as alphas inside the different sensor layers.

Generally the SRIM-calculated vacancies are referred as the number of atoms displaced from their original position and the number of atom positions left vacant per impinging ion. The threshold displacement energy E_d is an input of the simulation code that, in the case of SiC, differs for Si and C atoms [10]. This is the minimum value required to move an atom from its original position creating the displacement damage. The output of the program for vacancies produced by the ions and recoils is in units of vacancies/Å-ion. By multiplying this value by the experimentally used ion doses (cm^{-2}) the vacancies concentration is obtained in vacancies/cm^3. An example of such an analysis is illustrated in figure 2.6 where the vacancies concentrations caused by 1.47 MeV ^{4}He ions are calculated as the ions pass into the SiC. Three different doses of helium were used.

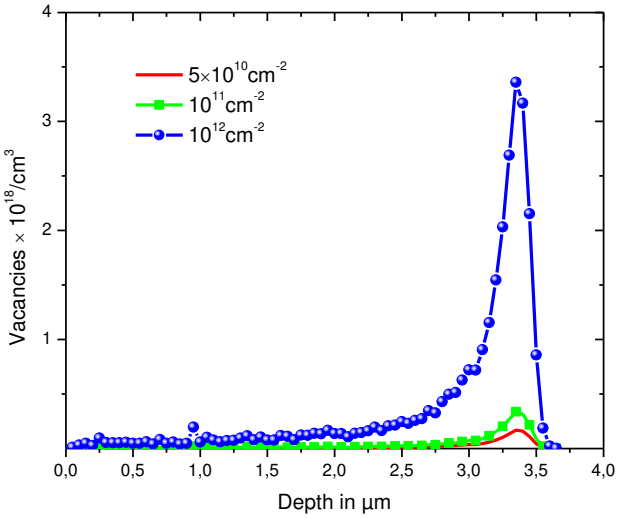

Figure 2.6 Simulated distribution of target vacancies calculated using SRIM for different doses of 1.47MeV He in SiC.

2.6 Secondary ion mass spectroscopy

To estimate the profile of the implanted species (Al or B in our case) inside SiC secondary ion mass spectroscopy (SIMS) measurements are used. It is a widely used technique to analyze for trace elements in solid materials, especially semiconductors and thin films. Such a powerful technique which is the most sensitive analysis technique relies on bombarding the surface with specific ions usually Cs^+, O_2^+, Ar^+, and Ga^+ at energies between 1 and 30 keV.

The basic principle of the SIMS technique is that a small area of the studied sample (~0.01–0.1 mm^2) is bombard by a beam of primary heavy ions. Consequently atoms and molecules are ejected from the topmost atomic layers due to the energy lost by the primary species in the material. A fraction of these sputtered particles is ionized (secondary ions) and finally detected by a mass spectrometer. SIMS is carried out in ultra-high vacuum in order to avoid the spread of primary and secondary ions along their path, and to inhibit the interference of the gases that are deposited on the surface to investigate. The principle of SIMS is illustrated in figure 2.7. The ultimate output of this technique is the concentration of the analyzed ions as function of their depth.

The most important feature of SIMS is its high sensitivity in detecting most elements of the periodic table even the lightest. Another important feature is its ability to distinguish different isotopes (^{11}B and ^{10}B in our case) followed by a remarkable depth resolution. All these features together make SIMS an attractive analytical method. SIMS is a destructive analytical technique; however, in most cases only a small part of material is required.

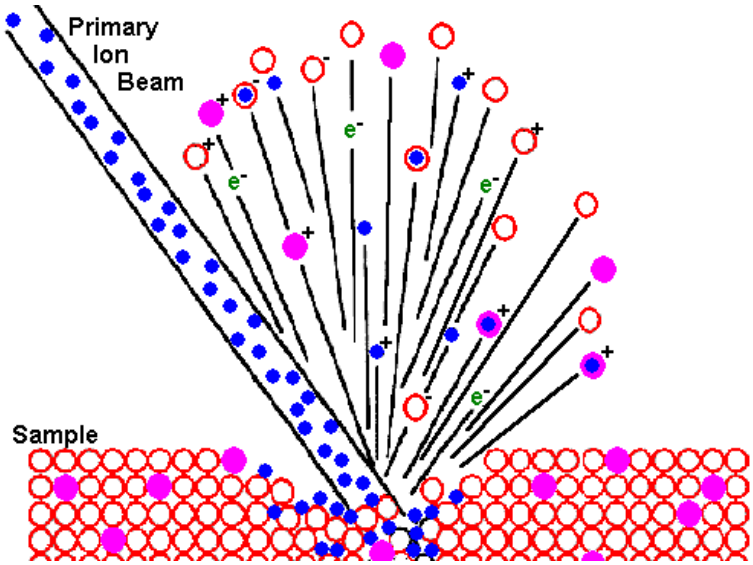

Figure 2.7 Principle of secondary ion mass spectroscopy

2.7 The fabricated detectors

The purpose of this work is to demonstrate the possibility of three new methods for realizing thermal neutron detectors based on ion implantation of ^{10}B. In the first type of detectors (D1) we implanted aluminum into 4H-SiC to create the p+ layer followed by ^{10}B implantation to create the neutron converter layer (NCL). For the second type of detectors (D2) it was demonstrated for the first time the possibility to realize thermal neutron detectors based on NCL and the p+ layer using a single ion implantation process. For the third type of detectors (D3) we demonstrated for the first time the possibility to convert 4H-SiC power diodes into thermal neutron detectors by standard ion implantation of boron into the metallic contact layer to realize the NCL. Another geometry was also realized by depositing a layer of boron

on the top of the Al metallic contact of a p-n junction. The technological processes followed to finalize these detectors will be discussed in detail in the next chapter with a study of their electrical behavior, and the responses of these detectors under different types of irradiation will be presented in chapter 4.

It was illustrated in the previous chapter that the neutron cross section of ^{10}B in the low neutron energy region is much higher than that of Si and C atoms. Therefore using a NCL based on such a material will remarkably enhance the response of a SiC detector. For this purpose a NCL based on ^{10}B was created. Using SRIM we calculated the distributions of ionizations and the vacancies of both Si and C atoms caused by the incoming charged particles (^{4}He and ^{7}Li). The thickness of the space charge region (SCR) and its position with respect to the NCL are important parameters which should be taken into consideration while fabricating any detector. Properly chosen, these parameters enable the collection of most of the electron-hole pairs (high ionization rate region) produced by the charged particles and to minimize the radiation damage (low vacancies region) within the detector sensitive area. This can be achieved by adjusting properly the dose and the energy of implanted species.

2.7.1 D1-Geometry

2.7.1.1 Realizing D1-diodes

For this geometry, aluminum has been used to create the p+ layer. Al as a dopant is known to have several advantages for fabricating heavily doped *p*-type layers in SiC by implantation. It is easier to activate Al than boron as a *p*-type acceptor in the SiC lattice during post-implantation annealing [72]. Moreover an Al acceptor is preferred for forming a low resistance p-type SiC because of its low ionization energy in SiC with respect to other acceptors such as B and a natural tendency to occupy electrically active Si sites [73]. However B ion implantation is more preferable for forming a deep junction and less implantation damage. Because of its lower mass than Al atoms B ions have a longer projected range. To facilitate the following discussion an illustration of the D1 geometry is shown in figure 2.8.

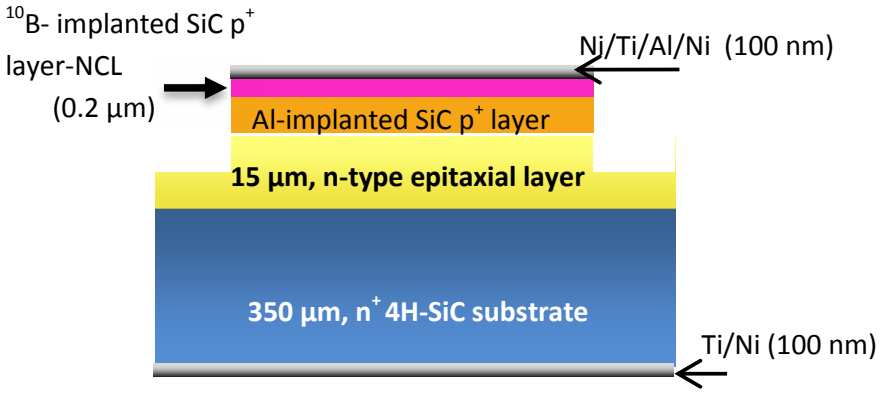

Figure 2.8 The final schematic configuration of the D1 geometry

However during ion implantation the used doses of Al or B ions are conducted with limits referring to their solubility limit in SiC. This is related to how many ions can be incorporated in the SiC lattice as dopants. If very high doses of dopants are used, they tend to form precipitates rather than occupying substitutional sites and hence the thermal stability and performance of SiC devices could be affected. This is a problem especially for acceptor doping, because of the high ionization energies of most of the used acceptors which requires very high concentrations of implanted atoms.

This value differs if the used material is epitaxial or initially implanted and the results from epitaxially doped material are considered as an ideal upper limit. It was found that the solubility for Al is ~2 $\times 10^{20}$ Al/cm^3 at 1900 °C [74]. In our case Al has been implanted at a fluence of 10^{15} cm^{-2} and at an energy of 280 keV respecting this solubility limit as indicated in figure 2.9 where the Al concentration is about 5×10^{19} cm^{-3} lower than the Al solubility limit in SiC. This figure indicates a deeper Al profile compared to B profile, and hence two successive layers are created.

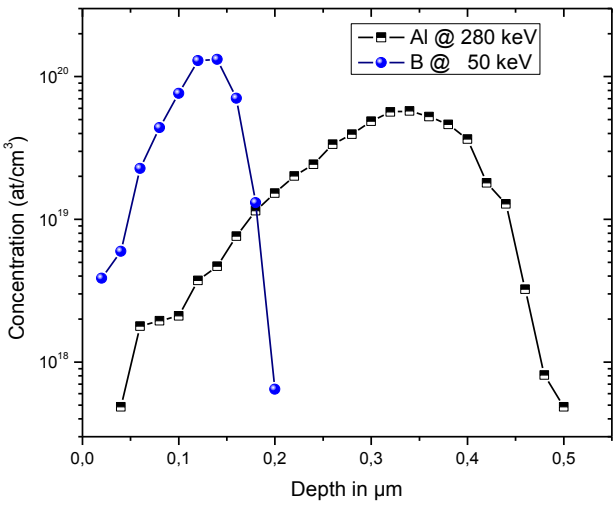

Figure 2.9 The B and Al profiles as obtained by SRIM

The Al implantation was carried out by ZnOrdic-Sweden at high temperature (400°C) in order to reduce the induced damage during implantation and to reduce the resistivity. It was found that as the implantation temperature increases from RT up to 1000 °C the resistivity and the surface roughness of the Al implanted 4H-SiC decreases. The decrease in the resistivity, especially when implanting at temperatures higher than 200°C, was attributed to the increase in the hole mobility rather than the change in the free carrier concentration [75]. Furthermore especially for high fluencies implanting at high temperature is critical; otherwise post-implantation annealing is not efficient to reduce the accumulated damage.

After the Al implantation, annealing step was carried out to activate the dopant and to create the p+ layer. Annealing at a temperature higher than 1600 °C can remarkably improve the sheet resistance of the Al implanted layer [76]. Furthermore, many parameters can affect the performance of the annealing step. For example this depends on the furnace and the heating and cooling rates. Such conditions should be taken into consideration to reduce the surface roughness and the resistivity. For instance a high heating-up rate improves the sheet resistance and preserves the surface roughness of the Al implanted 4H-SiC [77].

For the D1-diodes the annealing step was performed at 1700°C during 30 minutes under vacuum with a carbon cap layer in order to protect the SiC surface and to

avoid Si sublimation and step bunching formation. This carbon cap is a pyrolyzed photoresist film which is removed after post-implantation annealing [78]. This annealing step results in no diffusion of Al implanted species. Therefore the maximum Al concentration is 5×10^{19} cm^{-3}.

Then the NCL was realized by standard beam line implantation of ^{10}B ions at 50 keV and a dose of 1×10^{15} cm-^{2}. This step was not followed by any post-implantation annealing since no activation of the dopant is needed.

Based on the donor and the acceptor concentrations and using equation (2.2) the SCR width is about 1μm for the D1-diodes (at zero bias). According to SRIM simulations, we choose the thickness of the SCR and its position with respect to the NCL. This was achieved by adjusting the proper dose and energy of the implanted B and Al.

2.7.1.2 SRIM simulations of D1-diodes

As the neutron arrives at the ^{10}B based-NCL, interaction between neutron and ^{10}B will take place generating ^{7}Li and ^{4}He charged particles in opposite direction as shown in figure 2.10. These charged particles interact with the electrons and nuclei of the detector. The interactions with the electrons can lead to ionization and hence the creation of electron-hole pairs which are important for the signal formation. On the other hand, interactions with the nuclei lead to the displacement of the atoms from their original sites, which affects the performance of the detector by increasing leakage current and decreasing charge collection efficiency. For high energy charged particles, the ionization is the predominant mode of energy loss; however as the particle energy decreases, displacement damage becomes important. Thus most of the displacement damage occurs at the end of the range of the moving particles. Therefore the best detector configuration is the one with high ionization and low vacancy rates within its active region.

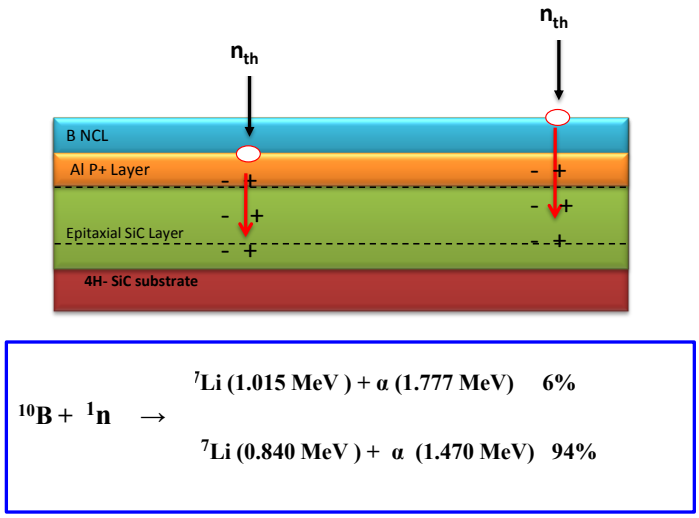

Figure 2.10 Schematic representation of the interactions between neutrons and ^{10}B at the upper and lower parts of the ^{10}B-based NCL

The energy of the alpha and ^{7}Li ions at each point along their normal trajectories into SiC is illustrated in figure 2.11. This gives information on the range of each particle. Being lighter than ^{7}Li, an alpha particle loses its energy more slowly than the ^{7}Li ion. Such curves as in figure 2.11 demonstrate that as the active region of the detector increases, more energy is deposited within it. This can be achieved by increasing the reverse bias across the detector under irradiation. However active regions thicker than 3.5 μm will no longer show the increased energy deposited by the 1.47 MeV alpha particles.

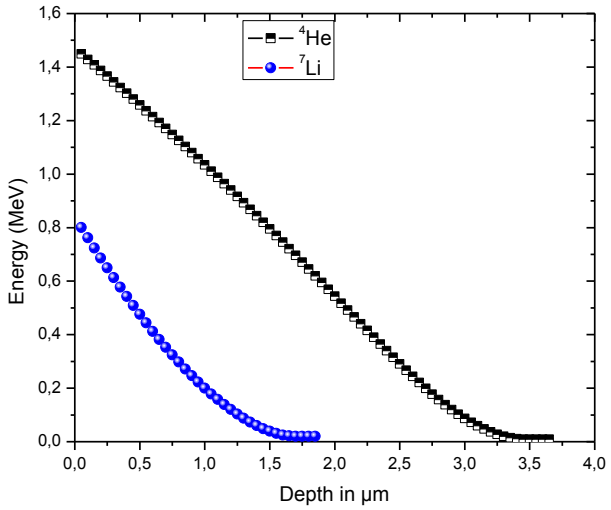

Figure 2.11 Energy loss of 1.47 MeV ^{4}He and 0.84 MeV ^{7}Li as a function of their penetration depth in SiC

Studying the distribution of vacancies caused by these charged particles is important to reduce the radiation damage within the active region of the detector. In addition, the distribution of ionizations gives information on the intensity of the output signal. Therefore using SRIM code, the energy deposition curves for charged particles in the detector is estimated revealing the proper thickness of the active region of the detector. Since two interactions with different probabilities are taking place between neutrons and B, the one with 6% of the total interaction is assumed low and hence it has not been included into our calculations.

The distribution curves for ionizations and vacancies produced by normally incident ^{10}B reaction products into the NCL followed by Al implanted SiC layer have been calculated. However for the sake of clarity, we first show separately the distribution of ionizations and vacancies for each charged particle alone (see figures 2.12 to 2.15). These curves correspond to the lower part creation of the charged particle which explains the absence of the 0.2 µm ^{10}B based-NCL. Then in what follows all these curves together are superimposed on the same axes in order to determine the best position for the SCR with respect to the ^{10}B-based NCL. The Bragg curves for ^{7}Li and alpha are shown in figure 2.12 and 2.13 respectively where the area under each curve represents the initial energy of each particle.

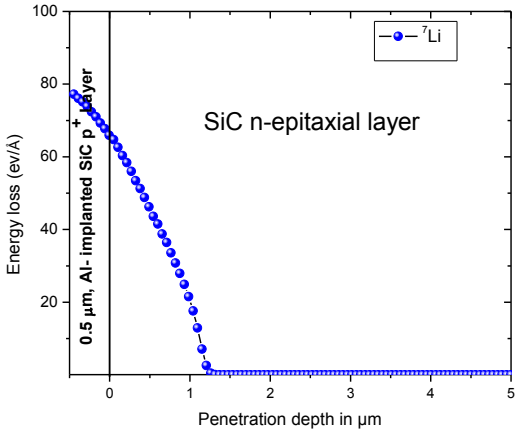

Figure 2.12 Distribution of ionizations generated by ^{7}Li (0.84 MeV) as they impinge normally the Al-implanted SiC p^{+} layer followed by SiC n-type epitaxial layer

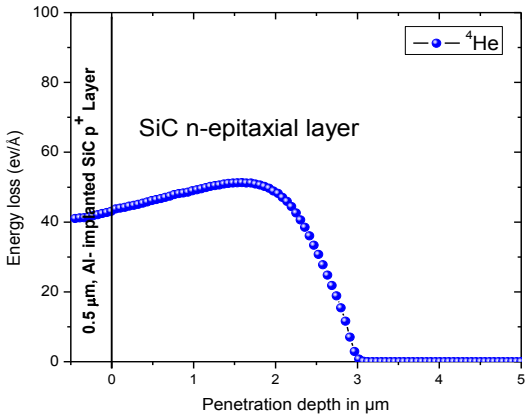

Figure 2.13 Distribution of ionizations generated by the ^{4}He (1.47 MeV) as they impinge normally the Al-implanted SiC p^{+} layer followed by SiC n-type epitaxial layer

The displacement damage caused by each charged particle ^{7}Li or alpha occurs near the end of their range. This explains the vacancy peak at the end range as shown in figure 2.14 and 2.15. Owing to its relatively higher mass, ^{7}Li stops before alpha inside SiC and causes higher displacement damage within the SiC detector.

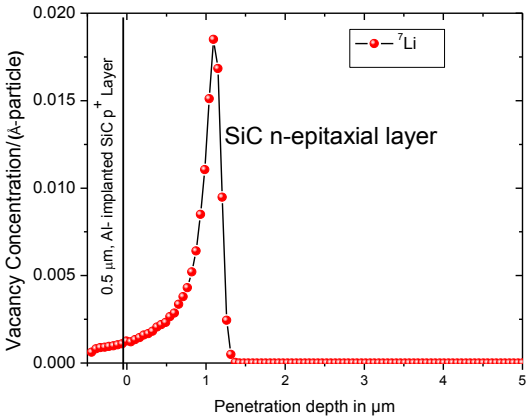

Figure 2.14 Distribution of vacancies generated by ^{7}Li (0.84 MeV) as they impinge normally the Al-implanted SiC p^{+} layer followed by SiC n-type epitaxial layer

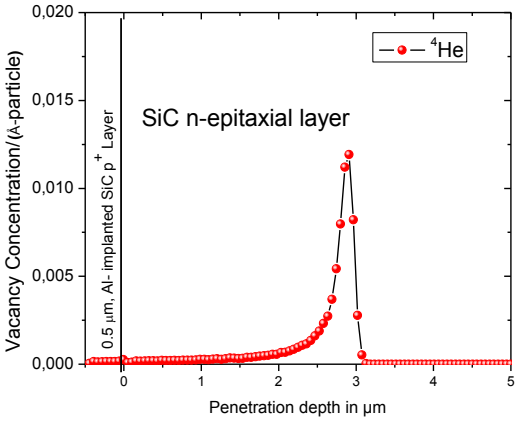

Figure 2.15 Distribution of vacancies generated by ^{4}He (1.47 MeV) as they impinge normally the Al-implanted SiC p^{+} layer followed by SiC n-type epitaxial layer

In the D1-diodes to collect most of the ionizations and to minimize the radiation damage caused by alphas inside the SCR, according to figures 2.16 and 2.17 the distance between the NCL and the SCR should be less than 1μm or at a distance between 1.5 μm and 2.5 μm. Choosing the former case, aluminum has been implanted to a depth of 0.5 μm and ^{10}B to a depth of 0.2 μm. This was done by choosing the proper energies of implantation for Al (280 keV) and B (50 keV) which correspond to the above mentioned depths.

In these simulations we assumed first that the charged particles are created in the upper part of the NCL (see figure 2.16) which explains the presence of the 0.2 μm of ^{10}B-based NCL. Then another possible option was taken into consideration by assuming that these charged particles are generated in the lower part of the NCL as shown in figure 2.17.

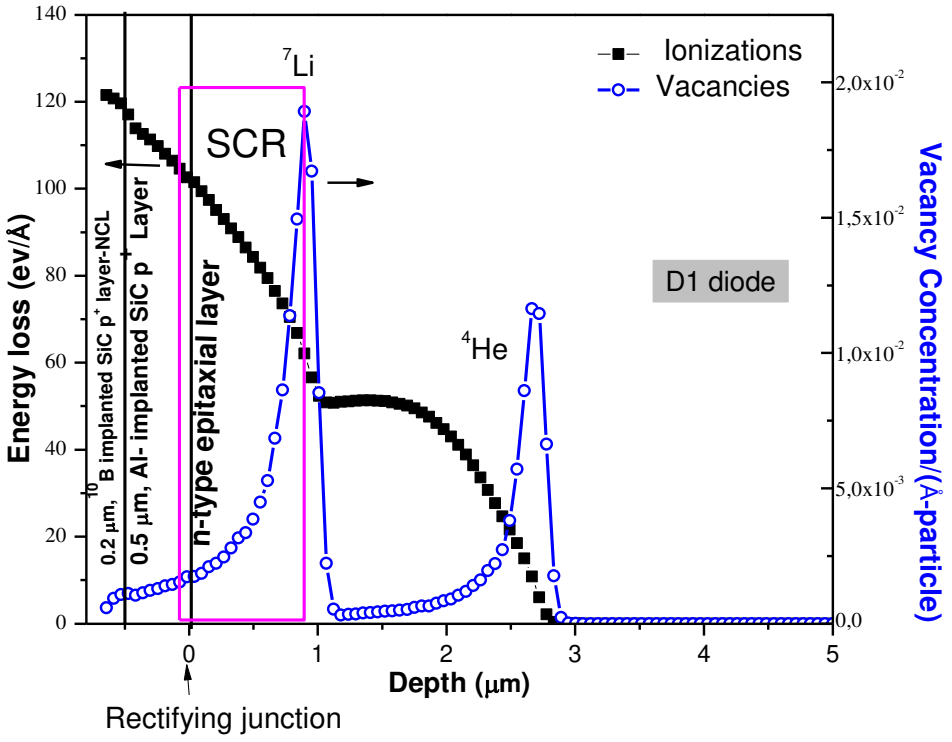

Figure 2.16 Distributions of vacancies and ionizations generated by the ^{4}He (1.47 MeV) and ^{7}Li (0.84 MeV) for the D1-diodes as they impinge normally the NCL and the Al-implanted SiC p^{+} layer followed by SiC n-type epitaxial layer. The position of the SCR is indicated by a rectangle.

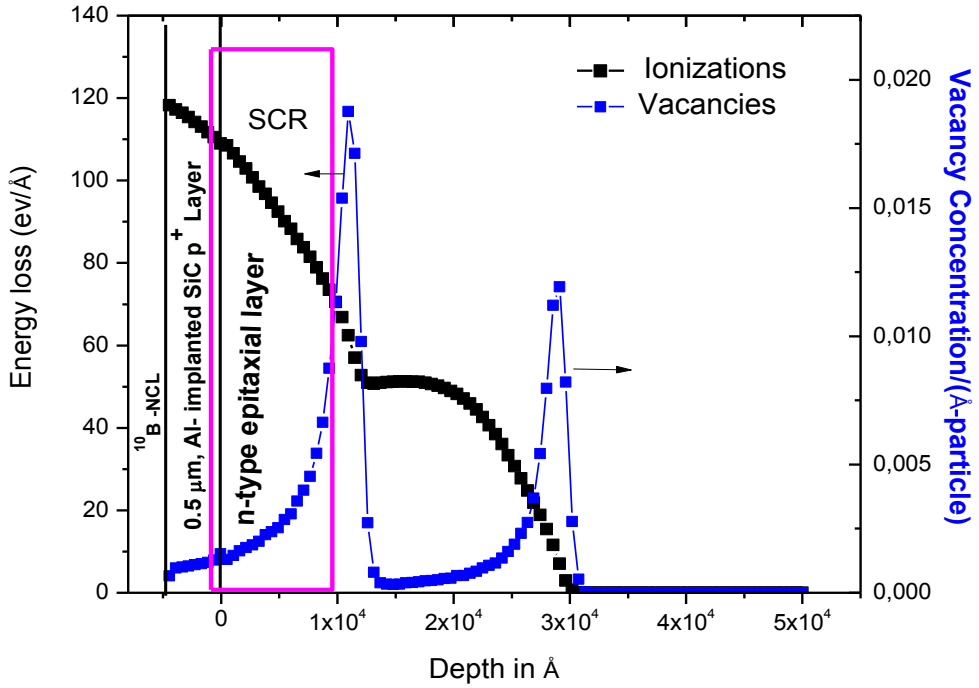

Figure 2.17 Distributions of vacancies and ionizations generated by the ^{4}He (1.47 MeV) and ^{7}Li (0.84 MeV) for the D1-diodes as they impinge normally on the Al-implanted SiC p^{+} layer followed by SiC n-type epitaxial layer.

As the reverse bias is applied to the detector, the width of the depletion region is increased permitting more charge collection. In figure 2.18 the SCR increases with the reverse bias voltage until the maximum n-type epitaxial layer is reached at 15 µm. It should be pointed out here that the maximum charge collection could be attained at -50 V when the SCR is thick enough to collect all the generated electron-hole pairs assuming that SRIM simulations confirms well with the experimental profile as was demonstrated by Ahmed et al. [79].

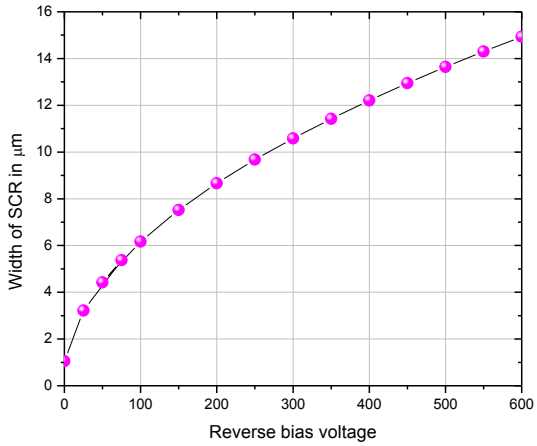

Figure 2.18 SCR width with respect to the reverse bias voltage

2.7.1.3 Full angle SRIM simulations

Refereeing to the fact that the produced charged particles are generated in all directions, we calculated the distribution of ionizations caused by alpha and ^{7}Li ions as they pass into SiC. Such simulations were established just to compare the best position of the NCL in the case of an isotropic angular distribution and a normal incidence. Figure 2.19 shows the distributions of ionization in both cases on a semilogarithmic scale. The SCR in both cases could still be positioned in the first 1 µm where the ionization rate is high.

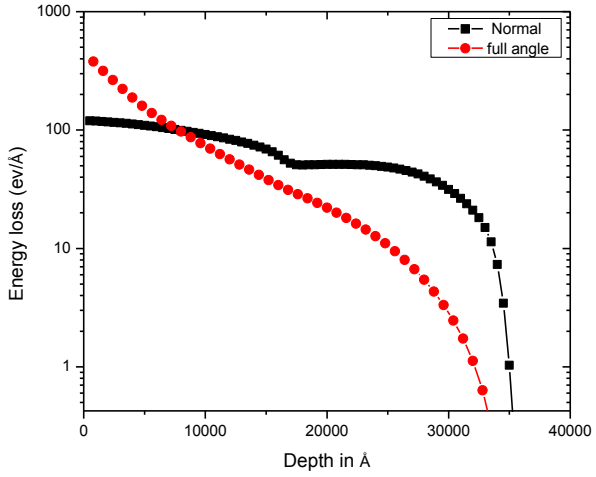

Figure 2.19 Distribution of ionizations caused by both alpha (1.47MeV) and Li (0.84 MeV) ions as they pass into SiC either at normal incidence or in an isotropic angular distribution

2.7.2 D2-Geometry

The D2-diodes correspond to diodes that have been implanted with ^{10}B to realize the NCL and the p+ layer in one single process which is the core of our patent[80]. Two types of D2-geometry have been fabricated, for the first type (D2-plasma) both the p+ layer and the NCL have been realized by Plasma Immersion Ion Implantation (PIII) while for the second type (D2-standard) standard ion implantation has been used instead of PIII.

2.7.2.1 D2-plasma

These diodes have been fabricated with plasma immersion ion implantation process. The main advantage of this process is the realization extremely shallow junction with thin ^{10}B- based NCL. This allows the placement of the active region of the detector within, or as close as possible, to the position where the charged particles are created. Recently PIII has been carried out on SiC material. L.Ottaviani et al. [81] used this method for N doping into SiC. A comparison between PIII and a beam-line implantation at 7 keV demonstrated the out diffusion of N after annealing at 1600 °C in case of PIII. However implanting N at 700 eV in both cases results in an important channeling effect. Moreover, plasma implanted samples show fewer point defects than beam implanted samples [82].

For the D2-plasma diodes natural boron (20 % of ^{10}B and 80 % of ^{11}B) has been used instead of the pure ^{10}B. Using BF_3, PIII has been performed at an energy of 8 keV and the dose was adjusted to get a peak concentration of few 10^{19} cm^{-3}. This allows the creation of a thin junction, and placing the 1 μm thick SCR in a location where the ratio of ionization energy loss to the displacement damage is maximized.

In order to activate the dopants, post-implantation annealing step was carried out at 1650 °C for 30 minutes. The impurity-atom profiles were analyzed after the post-implantation annealing by SIMS using a1 keV O_2^+ primary beam. The profile of ^{11}B and ^{10}B obtained by SIMS are shown in figure 2.20. The implantation depth is estimated to be 10 nm, revealing a very shallow junction. Such diodes showed high leakage current which may be due to the deposition of the ohmic contact over the p+ layer rather than depositing it on the edges leaving a window as presented in [83] [84]. Such a window area has been elaborated to allow the detection of the UV

photons. In addition, S. Biondo et al. [83] showed that 4H-SiC p-n diodes implanted with B by PIII processes reveal a low current density under reverse bias even after thermal annealing at 1650°C or 1700 °C, showing the interest of this method.

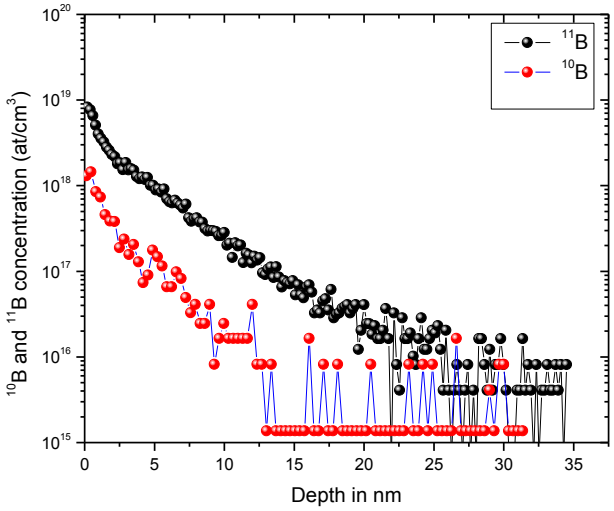

Figure 2.20 SIMS profiles of ^{10}B and ^{11}B

2.7.2.2 D2-standard

Comparison between deep boron-implanted diodes and aluminum-implanted diodes show that the former have a lower resistance [76] and at least an order of magnitude lower leakage current due to less implantation damage [85] [86]. Although as-implanted ^{10}B layers indicate a lower lattice damage compared to as-implanted Al layers [87] the annealing conditions should be taken into consideration in the case of boron to avoid their diffusion since B atoms are strong diffusing species in SiC at temperatures higher than 1400 °C.

For the D2 geometry, standard ^{10}B ion implantation processes were performed to realize both the p+ layer and the NCL. Unlike the D2-plasma, the D2-standard diodes have been implanted by pure ^{10}B ions. The energies and doses used to create a box-like profile are summarized in table 2.1. The ion energies used are selected to give a mean projected range of 0.5 µm of ^{10}B inside the SiC n-epitaxial layer. The multiple-energy ion implantation is used here to obtain a uniform doping concentration depth profiles in SiC. The doses were adjusted to obtain a flat

concentration of the order of 10^{20} cm^{-3} as shown in figure 2.22. Figure 2.21 below shows a schematic representation of the final D2-standard diodes.

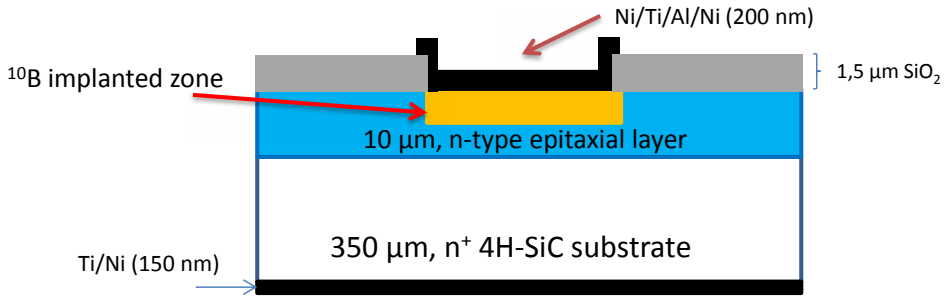

Figure 2.21 The schematic representation of the D2-standrad p+n diode

Table 2.1 Energies and doses of ^{10}B used to create the p+layer

Implanted element	**Ion energy (keV)**	**Dose ($\times 10^{14}$ cm^{-2})**
^{10}B	20	3,5
	50	5
	90	6,3
	140	7,4
	180	8,5

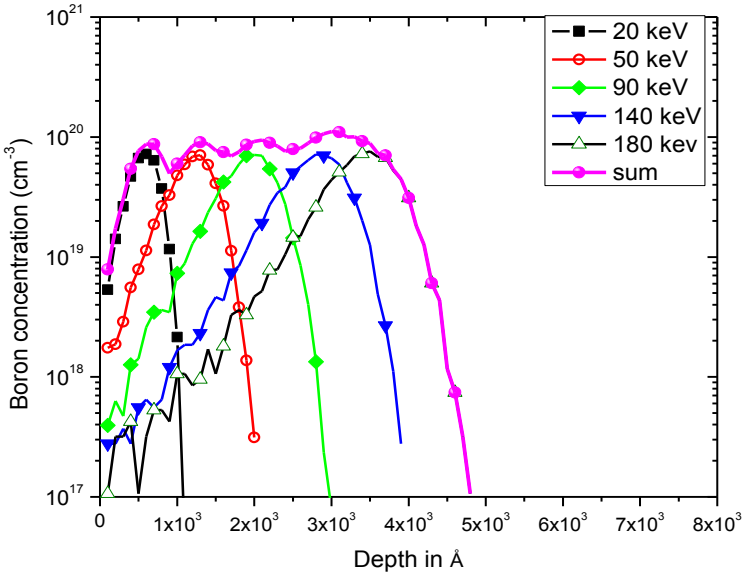

Figure 2.22 Box-shaped ^{10}B profile obtained by SRIM for different implantation energies as listed in table 2.1

After the ^{10}B ion implantation and in order to activate the dopant and hence to create the p-n junction, two annealing steps have been followed to reduce the diffusion of B. It is known that diffusion of B should be suppressed to avoid a change in the conductivity of the implanted sample. It was found that during the annealing step at temperatures higher than 1750 °C remarkable diffusion of B atoms occurs leading to a decrease in the B concentration and an enlargement of the p-n junction [64]. Although annealing at 1500 °C results in no diffusion of B, a low activation rate of the B dopant was found [88] which requires increasing the annealing temperature above 1500 °C. A complete activation of B implanted into 4H-SiC could be obtained by annealing at 1750 °C for 30 min [65].

The annealing steps for all the D2-diodes were carried out at IM2NP (Institut Materiaux Microelectronique Nanosciences de Provence) using a resistive furnace. Such a prototype furnace (purchased from VEGATEC^{TM}) consists of a vertical resistive reactor joined with a lift system. This permits a high precision control of the heating and cooling rates up to 20°C/s [77]. The importance of such a fast heating rate (20°C/s) has been studied in [77] demonstrating a high activation in the 4H-SiC Al-implanted layer. The maximal attainable temperature in this furnace is 1800 °C. To prevent Si sublimation from the samples during annealing, a silicon partial pressure is imposed inside the reactor.

Although ion implantation of B into SiC is an interesting process for forming p-type region, the main limitation is the B diffusion during post-implantation annealing. However this mechanism could be suppressed by co-implantation of C or by a pre-annealing step at 900°C. It was found that silicon-self interstitial control the diffusion of B in SiC rather than the silicon vacancies [89]. Therefore in order to suppress the enhanced diffusion of B, first the diffusion of Si interstitial should be avoided. This is achieved by two different methods: (1) two annealing steps; the first at 900°C followed by an additional annealing at elevated temperatures. With these two annealing steps, it has been demonstrated that low diffusion profiles of B could be attained [90]. This is because at 900 °C the Si interstitials move and recombine with Si vacancies. At this temperature the diffusion of B interstitials is still negligible, until the temperature is elevated to a limit which allows the movement of the B ions on the Si lattice site. (2) C/B co-implantation where the C and Si interstitial pairs are

formed which fix the Si interstitial. Such methods indicate an increase in the hole concentration and a decrease in the resistivity of the implanted sample [91].

For the D2-standard diodes the annealing process was divided into two annealing steps in order to minimize the diffusion of B. This was achieved by annealing at 900 °C for long time 120 minutes and then at 1650°C for 30 minutes under argon. Figure 2.23 shows the profiles of B after implantation as obtained by SRIM, and after annealing as obtained by SIMS measurement. Thanks to the specific characteristics of the used furnace and to the two annealing steps, a low diffusion of B was obtained. Thus the position of the SCR is the same before and after annealing in this case, this is in a good agreement with our simulations.

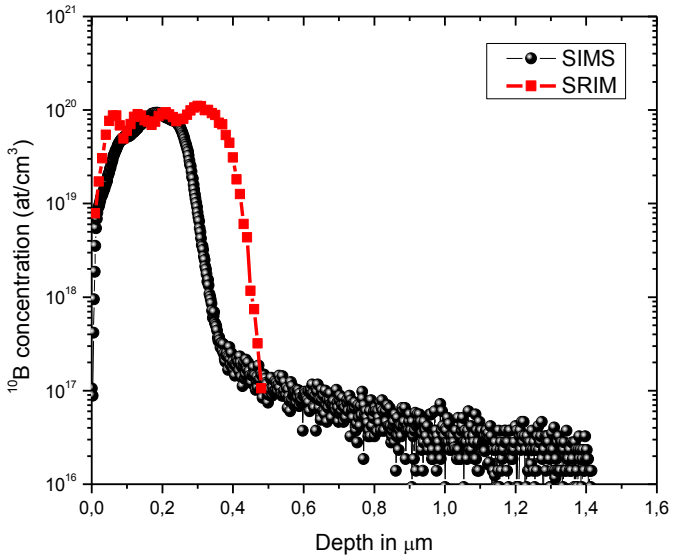

Figure 2.23 Profile of B obtained by SIMS compared with the SRIM-simulated profile

Figure 2.24 shows the distribution of ionizations and vacancies created by the charged particles (^{4}He (1.47 MeV) and ^{7}Li (0.84 MeV)) that are generated as a result of the interaction between ^{10}B and neutrons at the lower part of the NCL. The width of the SCR is 0.8 μm which is thin enough to be located in a position of high ionizations, and outside the region of high vacancies generated as a result of the interactions between ^{7}Li and SiC.

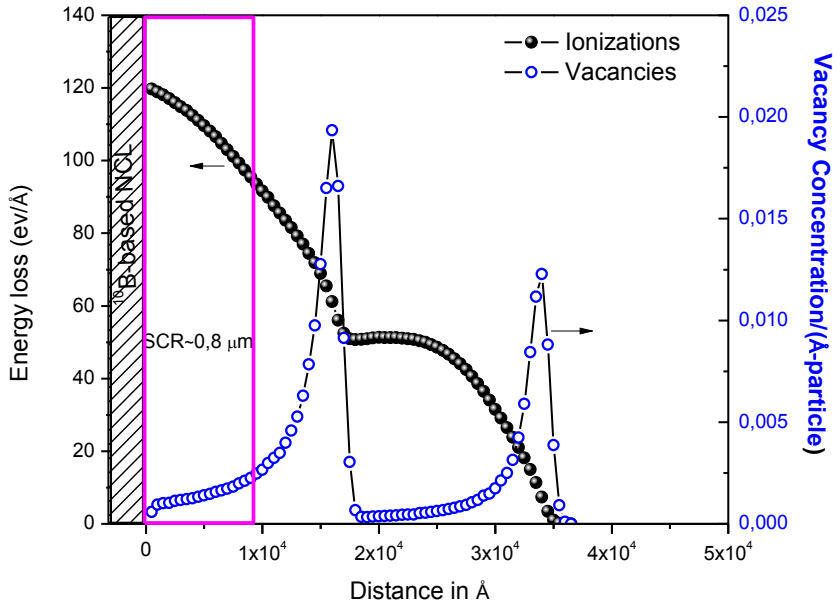

Figure 2.24 Distribution of vacancies and ionizations in D2-standard diodes caused by ^{7}Li and ^{4}He as they pass in a normal direction into SiC. The position of the SCR is illustrated by a rectangle

2.7.3 D3-Geometry

The D3-geometry is the geometry where ^{10}B ions have been implanted directly into the Al metallic contact to create the NCL within the metallic contact. This Al layer has been sputtered on the top of the ohmic contact as shown in figure 2.25 and figure 2.26. Two series of this geometry (D3-a and D3-b) have been realized. In the first geometry(D3-a) the diodes have been implanted by ^{10}B into the 4 µm Al layer whereas in the second type (D3-b) the used Al layer thickness was reduced into 1 µm. The D3-b diodes are realized on 4H-SiC wafer with one single p+epitaxial layer whereas for the D3-a two p+ and p++ epitaxial layers have been used. This is illustrated in figure 2.25 and figure 2.26 which provide a direct comparison of the parameters used in D3-a and D3-b diodes. The D3-b geometry is an improvement of the initially realized D3-a geometry.

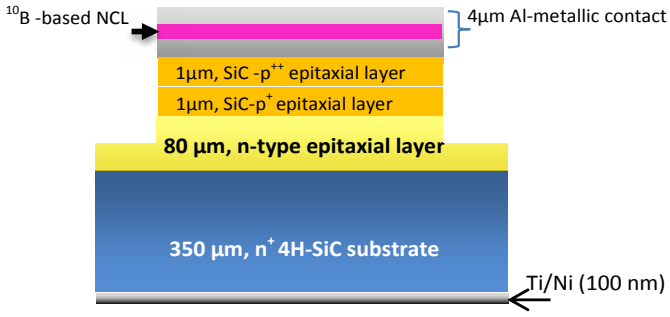

Figure 2.25 Schematic representation of the D3-a diode

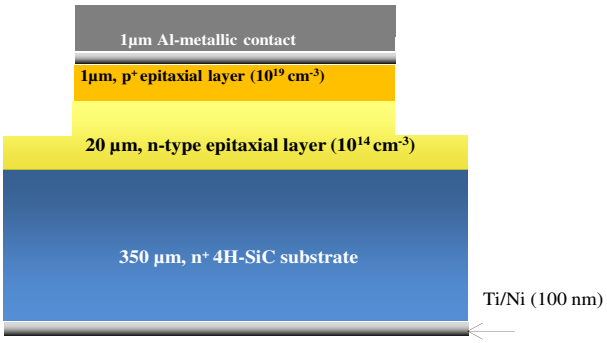

Figure 2.26 Schematic representation of the D3-b diode

2.7.3.1 D3-a and D3-b

The D3-a diodes were implanted with ^{10}B at 2 MeV which was the maximum available energy and at a dose of 5×10^{15} cm^{-2} into the thick Al contact layer for thermal neutron detection. The implantation process was performed at high temperature (400 °C).

Since the Al metallic contact in D3-b diodes is thinner than that for D3-a diodes, ^{10}B has been implanted at much lower energy (180 keV) and at the same dose of 5×10^{15} cm^{-2}. The Gaussian profiles of B for D3-a diodes and D3-b diodes are shown in figure 2.27 and 2.28 respectively. The implantation energy has been chosen to get a NCL as close as possible to the active region of the detector.

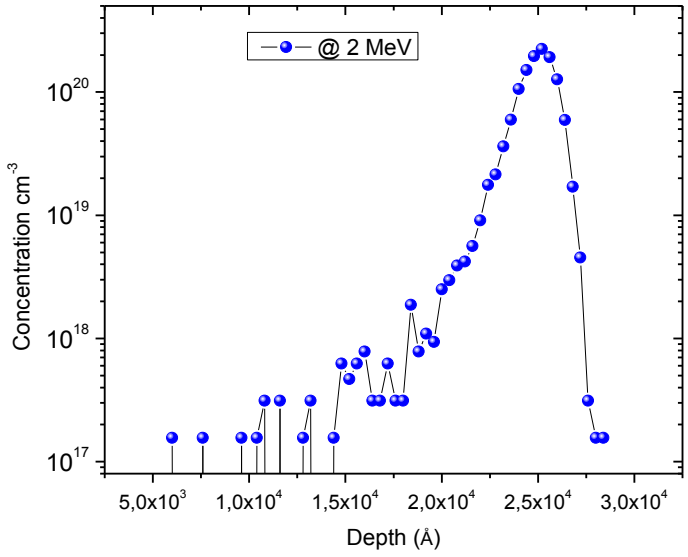

Figure 2.27 Distribution of ^{10}B implanted profile into Al (4 µm) at 2 MeV

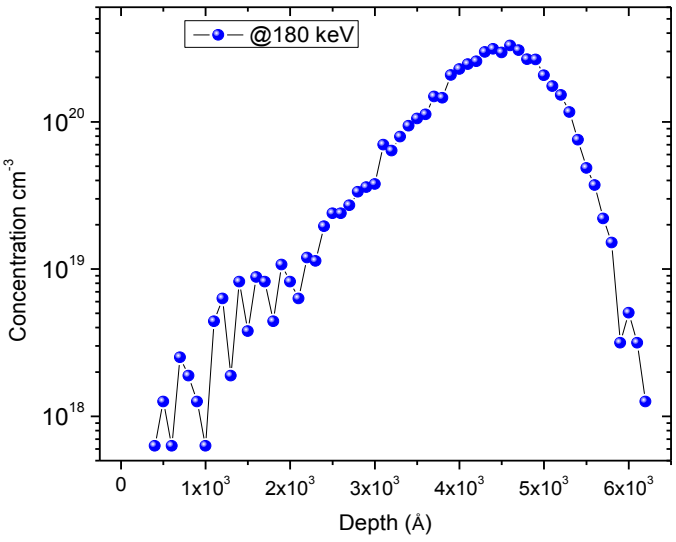

Figure 2.28 Distribution of ^{10}B implanted profile into Al (1 µm) at 180 keV

Figure 2.29 shows the B profile obtained for D3-a diodes after B implantation by SRIM (simulated profile) and SIMS. There is a clear diffusion of ^{10}B beyond the Al layer deep into the SiC epitaxial layer. This could be attributed to the high temperature (400 °C) used while implanting B. The drawback of this diffusion was clearly seen by the high leakage current of B implanted diodes with respect to non-

implanted ones, this will be discussed in the next chapter. However there is no diffusion in the D3-b diodes where they show the same electrical behavior before and after the B implantation which has been performed at room temperature.

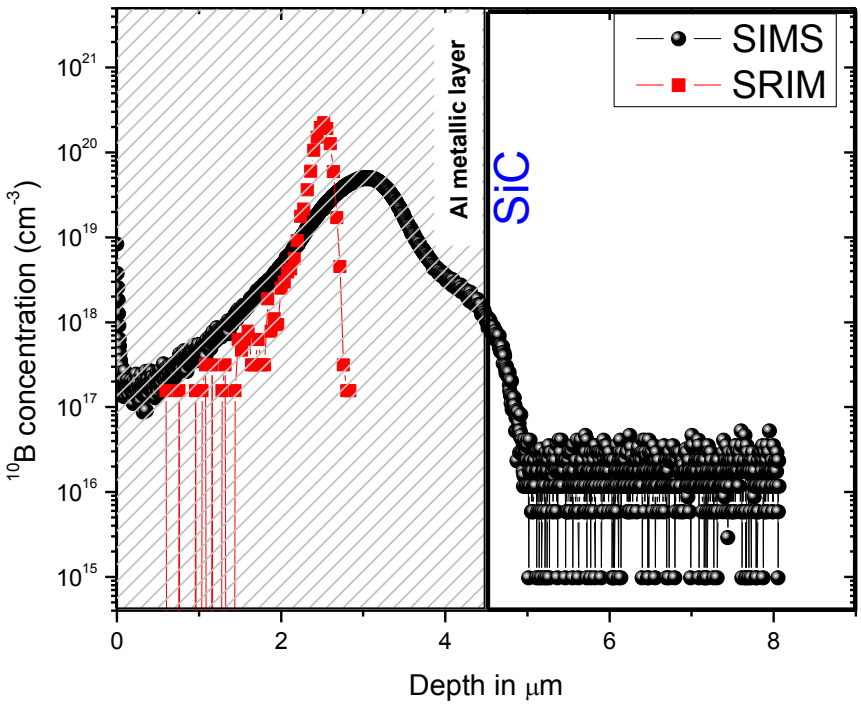

Figure 2.29 B profile in Al and SiC as obtained by SIMS and SRIM

After estimating the B profile inside the Al metallic contact, the distributions of ionizations and vacancies of both Si and C atoms caused by the charged particles (^{4}He and ^{7}Li) have been calculated. The SCR should be positioned in a high ionizations region and in a low vacancies region. This can be achieved by adjusting properly the dose and the energy of the implanted species. A comparison between the energy loss of 1.47 MeV alpha particles in Al and SiC has been calculated by SRIM as shown in figure 2.30. Since the density of Al is less than that of SiC, the energy loss of alpha particles in Al is lower than in SiC. This explains the longer range of the 1.47 MeV alpha particles in Al than in SiC.

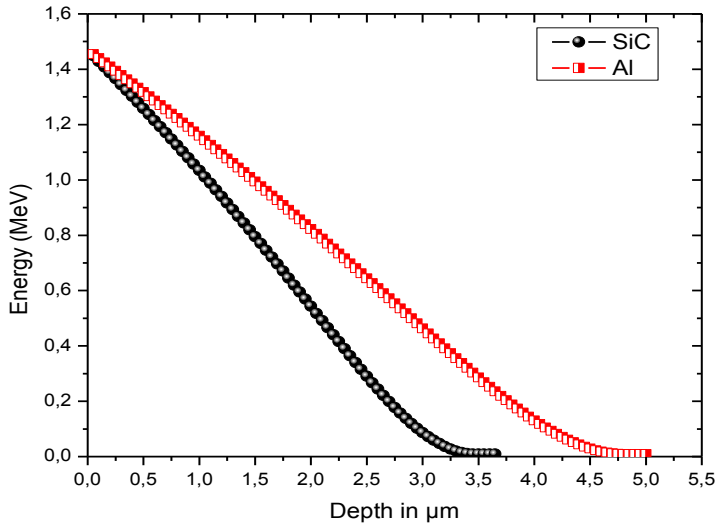

Figure 2.30 Energy loss of alphas with energy 1.47 MeV in Al and SiC

Figures 2.31 and 2.33 show the distribution of ionizations and vacancies caused by ^{7}Li and alpha particles, as they are injected inwards, perpendicular to the device surface for D3-a and D3-b diodes respectively. As shown for the D3-a diodes the distance between the NCL and the SCR is 3 µm, which is too long for ^{7}Li ions to reach the active region. This minimizes the radiation damage caused by the ^{7}Li charged particles. Although in figure 2.32 this distance has been reduced referring to the fact that B ions have been diffused further than their expected range, there is still no contribution from ^{7}Li. This is because the projected range of ^{7}Li into SiC is less than 2 µm which is the total thicknesses of the two epitaxial layers. However, for the D3-b diodes this distance has been reduced to around 1.35 µm. This allows both charged particles to contribute to the overall detector signal.

It should be pointed out that in both types of the D3 diodes the SCR is thick enough to collect the electron–hole pairs created by the charged particles at zero bias. Thus increasing the reverse bias will not reveal higher energy deposit in the thermal neutron-induced peak [92] as we will see in chapter four. This behavior confirms the simulated results.

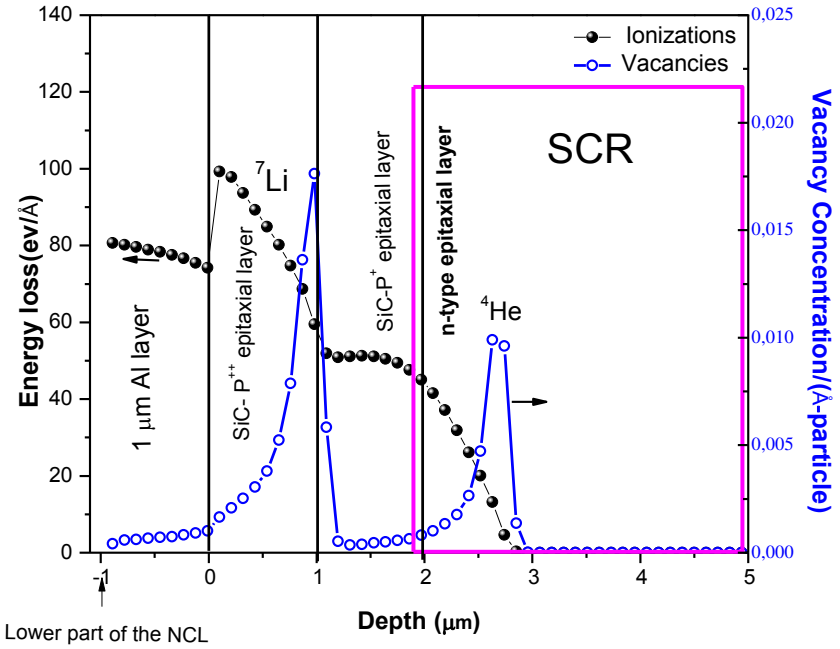

Figure 2.31 Distribution of vacancies and ionizations in D3-a diodes caused by ^{7}Li and ^{4}He as they enter in a normal direction into the device. Based on SRIM profile of B

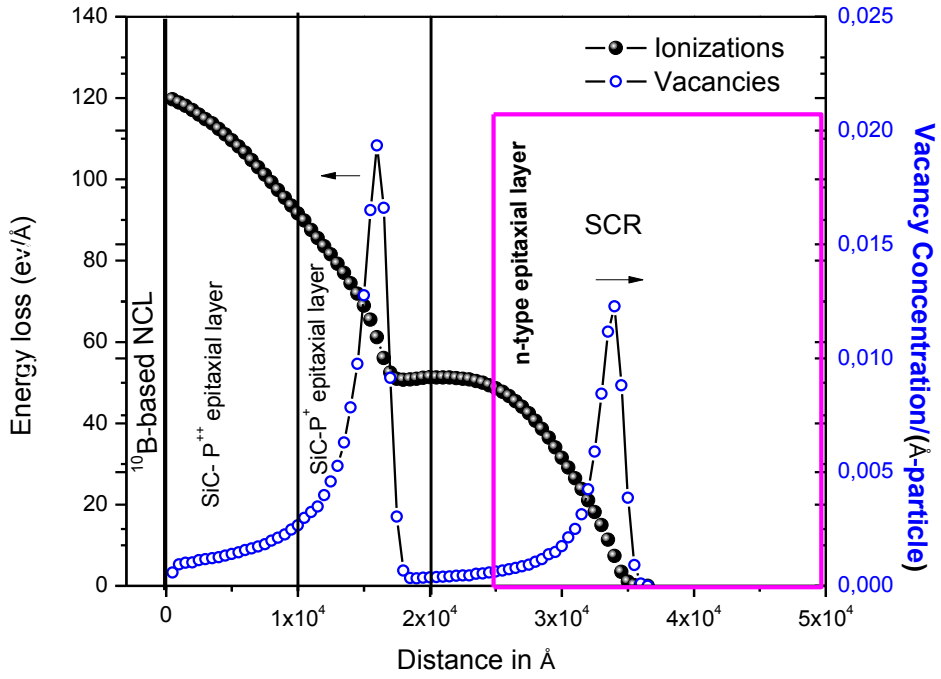

Figure 2.32 Distribution of vacancies and ionizations in D3-a diodes caused by ^{7}Li and ^{4}He as they enter in a normal direction into the device. Based on SIMS profile of B

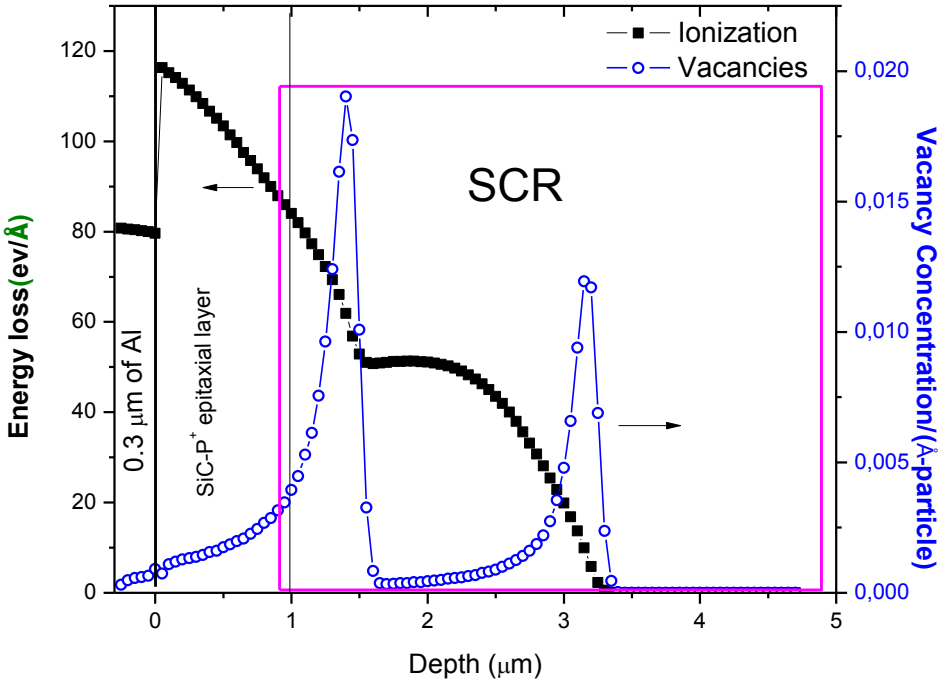

Figure 2.33 Distribution of vacancies and ionizations in D3-b diodes caused by ^{7}Li and ^{4}He as they pass in a normal direction into the device.

2.7.4 D4-Geometry

Although so far we have considered ion implantation as a method of choice for doping and creating ^{10}B-based NCL, other methods could be interesting such as depositing a layer of boron-containing film on a Schottky or a pn device. For example thin films of titanium boride (TiB_2) were deposited by reactive sputtering to a thickness of 120 nm on a silicon substrate [93], or depositing B_2H_6 a nano-layer by chemical vapor deposition on Si substrate [94].

The same structure as for the D3-a diodes has been used here for sputtering a 100 nm thick B_4CN layer on the top of the 4 μm Al layer as shown figure 2.34. However as shown in figure 2.35 that the SCR is located so far from the NCL leading to no contribution from the created charged particles. In such geometry where no thermal neutrons were detected could confirm the validity of the simulated result.

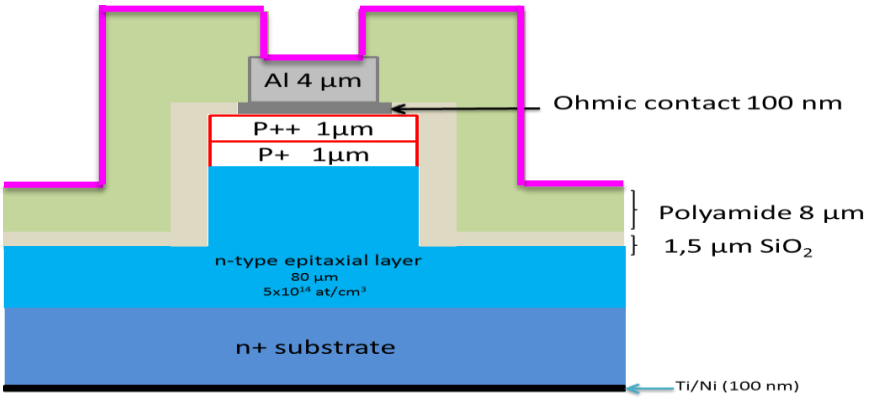

Figure 2.34 Schematic presentation of the D4- diode

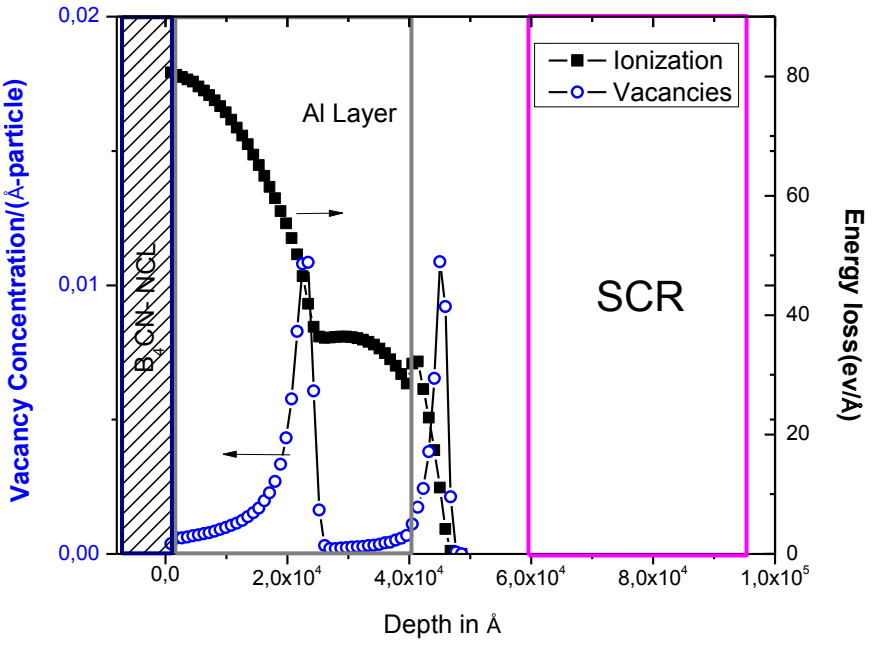

Figure 2.35 The distribution of vacancies and ionization in D4 diodes caused by ^{7}Li and ^{4}He as they pass in a normal direction into the device.

In summary, realizing thermal neutron detectors based on ion implantation of ^{10}B is a challenging task. This is because the thickness and the position of the active volume of the detector with respect to the NCL could be controlled. As mentioned previously, this was attained by adjusting the proper energy and dose of the

implanted species. It should be pointed out that not only the placement of the active region of the detector in a high ionization rates means a detector with high signal. This is because the electrical behavior of the detector should be taken into consideration in order to avoid noise and trapping of the created electron-hole pairs. The electrical behaviors of the fabricated detectors of this work are presented in the next chapter.

This page intentionally left blank

Chapter 3. Fabrication of SiC Detectors

Based on the SRIM simulations presented in chapter 2, different types of detectors have been fabricated. Detailed study of the implantation parameters (energy and dose) have to be made to obtain detectors with high signal to noise ratios and with high ionization rates. This was attained by a proper position of the SCR with respect to the NCL. In the present chapter we will focus on the way different geometries are realized starting from the initial 4H-SiC wafer up to the finalized detector. After realizing the detectors electrical characterizations were measured in order to select the best diodes to be irradiated. All the detectors in this study have been fabricated in a clean room in INSA-Lyon with cooperation with Pr. M. Lazar. In the present work, four 4H-SiC wafers with different parameters have been used. Two of the wafers were purchased from Cree [95] and the others from Ascatron with different parameters as summarized in the following table.

Table 3.1 The 4H-SiC used wafers with their specific parameters

	Realized diodes	**Wafer supplier**	**Epitaxial layer 1**	**Epitaxial layer 2**	**Epitaxial layer 3**
Wafer 1	D1 D2-plasma	Cree	n-type, 15 µm 3×10^{15} cm^{-3}		
Wafer 2	D2-standard	Ascatron	n-type, 10 µm 5×10^{15} cm^{-3}		
Wafer 3	D3-a	Cree	n-type, 80 µm 5×10^{14} cm^{-3}	p-type, 1 µm 2×10^{17} cm^{-3}	p-type, 1µm 2×10^{19} cm^{-3}
Wafer 4	D3-b	Ascatron	n-type, 20 µm $1\text{-}2\times10^{14}$ cm^{-3}	p-type, 1 µm 1×10^{19} cm^{-3}	

3.1 D1-Geometry

3.1.1 Technological processes

For realizing the D1 and D2-plasma geometries, n^+-type 4H-silicon carbide wafer (8° off-axis) purchased from CREE Research have been used. As shown in figure 3.1 two quarters have been used for patterning the D1 and D2-plasma diodes. Each quarter contains around 400 diodes with different diameters. The used wafer is with n^+-type substrate 350 μm thick. The nitrogen doped n-type epitaxial layer has a concentration $3\times10^{15}cm^{-3}$ and a 15 μm thickness.

For the D1 diodes the p^+ layer was created by a standard beam line ion implantation of aluminum ions at 280 keV and a dose of 1×10^{15} cm^{-2}. This doping step was realized at 400°C to limit the implantation defects. The implanted zone was defined by a mask.

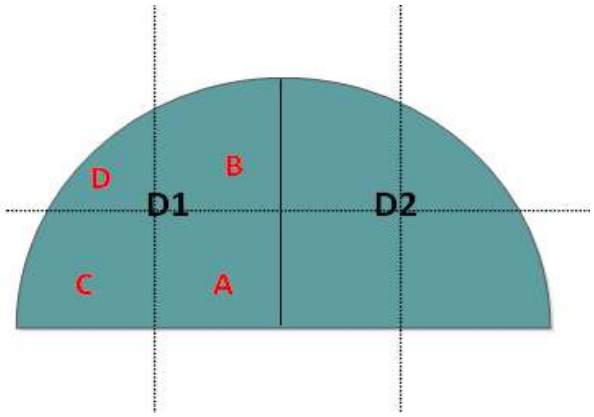

Figure 3.1 Two quarters of the wafer 1 used to pattern the D1 and D2-plasma diodes

Activation annealing was performed at 1700°C for 30 minutes under vacuum with a carbon cap layer and results in no diffusion of Al. Therefore the maximum Al concentration is about 5×10^{19} cm^{-3}. Then the NCL was realized by standard beam line ion implantation of ^{10}B ions at 50 keV and a dose of 1×10^{15} cm^{-2}. In the case of Schottky diodes, Ni/Ti/Al/Ni Schottky contacts were subsequently evaporated onto the n-type epitaxial layer.

The pattern used to create D1 and D2-plasma diodes is presented in figure 3.2. Diodes with three different diameters were realized (1 mm, 0.4 mm and 0.25 mm).

The dashed rectangles represent the Schottky diode structures. Ti/Ni was used as a back ohmic contact for both the p-n and Schottky diodes with 100 nm thickness. Such contacts have been successfully used in the fabrication of ohmic contacts on n-type SiC layers [96] [97]. The ohmic contacts were then annealed with JIPELEC rapid thermal annealing at 900 °C for 90 s. This annealing step is accomplished by an interaction between the Ti/Ni metallization and SiC which is necessary for obtaining thermally stable contact with low contact resistance [98] .

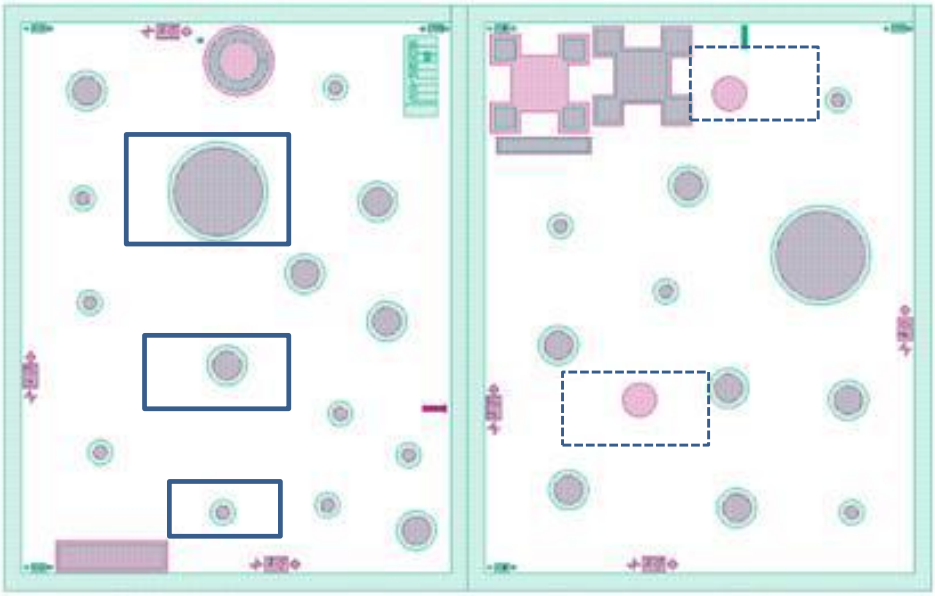

Figure 3.2 Pattern used to realize pn (solid rectangles) and Schottky (dashed rectangles) SiC detectors.

All the technological processes start by cleaning up the wafer which is important to prepare the surface before each technological step. The cleaning process is achieved by using a cleaning solution of H_2SO_4:H_2O_2 in a 1:3 ratio to remove organic materials, including remaining photoresist from the wafer surface. Typically this step is applied first in a cleaning sequence; it is known as "piranha" or "caro" clean.

Note that masks such as SiO_2 or heavy metals such as nickel could be used during ion implantation at high temperatures. The different sequences followed to realize the D1-diodes are summarized as follows.

3.1.1.1 Alignment marks

After cleaning the surface of the SiC wafer, alignment marks should be performed which are necessary for the subsequent lithography steps. The alignment marks were defined with a negative lithographic photoresist followed by electron beam evaporation of Ti/Ni layer. After depositing the metal, it is possible to remove the photoresist by lift-off.

Then a reactive ion etching (RIE) was performed with sulfur-hexafluoride (SF_6) in combination with O_2 gas to etch the 4H-SiC. After the alignment is finalized the deposited metal is removed by a "Caro" clean followed by immersion in HF solution to remove the surface oxide.

3.1.1.2 Al ion implantation

Again a cleaning step is performed then the wafer is ready to be defined by a negative lithographic photoresist (see figure 3.4). This step is followed by electron beam evaporation of a Ti/Ni layer to a 345 μm thickness (see figure 3.5). The choice of using Ni as a mask layer for implantation is due to its high density and thus its high stopping power for the implanted ions. Moreover the choice of the thickness of the Ni layer and the ion implantation energy should be well chosen to avoid the implantation beneath the used mask.

Then to remove the photoresist with its adhesive metallic layer a lift-off was applied as illustrated in figure 3.6. After this step the sample is ready to be implanted by Al in the patterned zone as shown in figure 3.7. After the implantation, the Ti/Ni layer should be removed from the SiC surface (figure 3.8). For this a caro clean is applied. Then a post-implantation annealing is performed in order to activate the dopants.

Figure 3.3 The initial wafer

Figure 3.4 Definition of the implantation zone by photoresist

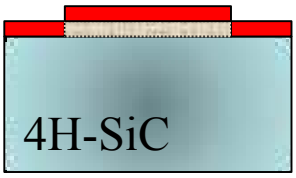

Figure 3.5 Ti/Ni deposition

Figure 3.6 Lift-off

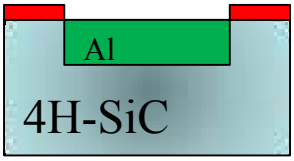

Figure 3.7 Al ion implantation

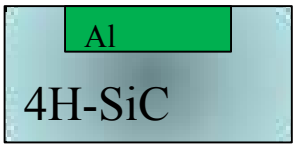

Figure 3.8 Caro clean

3.1.1.3 B ion implantation

To create the NCL similar technological processes performed to define the Al implantation zone are also followed in the case of ^{10}B ion implantation. Again Ti/Ni is used as a mask for ^{10}B ions implantation. The last two steps after the ^{10}B implantation are shown in figures 3.9 and 3.10.

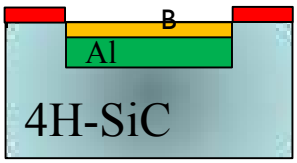

Figure 3.9 B implantation

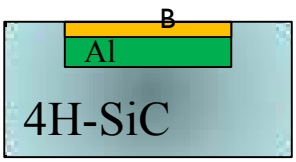

Figure 3.10 Caro clean

3.1.1.4 Metallization

After the Al and ^{10}B ion implantations are performed and before depositing the anode and the cathode contacts on the front and back of the wafer respectively, a mesa structure is realized. This is done by etching the edges of the sample by RIE to form a mesa structure in order to prevent leakage current along the sample's sides and electrically isolate them from the n-type epilayer (figure 3.11). Next, the metallization (Ni/Ti/Al/Ni) is chosen such that a low resistive ohmic contact on silicon carbide is obtained [99] [100]. The importance of ohmic contacts relies on carrying electrical current ideally with no parasitic resistance. Diode patterns were defined by lift-off of Ni/Ti/Al/Ni (100 nm total thickness) layer on the SiC wafer as shown in figure 3.12. This was done by electron beam evaporation in a high-vacuum chamber where the base pressure was kept below 1×10^{-7} mbar, and the pressure during the deposition was below 5×10^{-7}mbar. The ohmic contacts were then annealed under Ar atmosphere with JIPELEC rapid thermal annealing (RTA) on a graphite holder at 800 °C for 90 s. The final structure of the D1 detector is illustrated in figure 3.13.

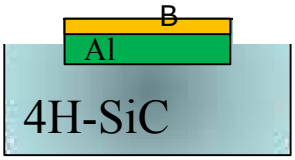

Figure 3.11 Mesa structure

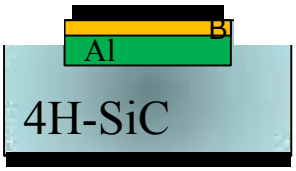

Figure 3.12 Cathode and anode deposition

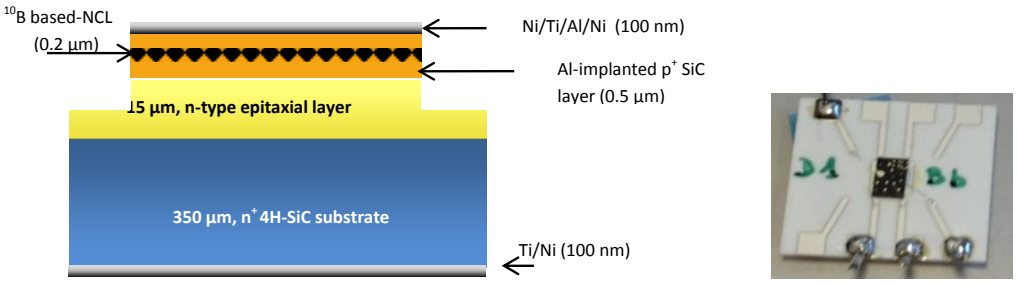

Figure 3.13 Schematic structure of the D1-pn diode (left) and a picture of D1-diodes glued to an alumina support (right)

3.1.2 D1-Current density voltage measurements

After finalizing all the detectors, electrical measurements were performed to characterize them. Leakage current density with respect to the reverse bias is one of the principal properties of semiconductor radiation detectors. It gives information about the defects concentration present in the SCR and estimation about the signal-to-noise ratio during the irradiation of the detectors. Current-voltage measurements were carried out at room temperature in a Faraday cage shielding the detector from electrical noise and light. The main results of the current-voltage measurement of the D1-diodes are presented in figure 3.14. The low leakage current density indicates that the boron implantation at 50 keV did not introduce a high defect concentration, demonstrating the strength of this method of realizing thermal neutron detectors. At -40 V, we measure a current density of few nA/cm² for each diode. Moreover such diodes show low signal-to-noise ratio during the irradiation test.

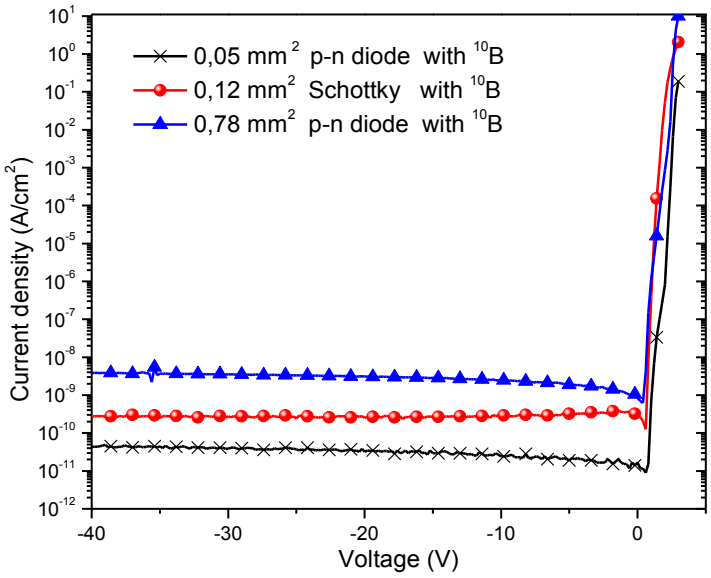

Figure 3.14 Current density of the pn and Schottky diodes (D1-diodes) with different surface areas after ^{10}B ion implantation

3.2 D2-Geometry

The D2-diodes are those implanted by ^{10}B to create the p+ layer and the NCL in one single process. The same wafer and masks which have been used in realizing the

D1-diodes have been also used to finalize the D2-plasma diodes therefore the diodes' diameters are the same (1 mm, 0.4 mm and 0.25 mm). Similar technological processes followed to finalize the D1 diodes are followed as well here. Using BF_3 PIII has been performed at an energy of 8 keV followed by post implantation annealing step which was carried out at 1650 °C for 30 minutes in order to activate the dopants. Then the ohmic contacts were defined by a lift-off of Ni/Ti/Al/Ni layer on the SiC wafer by electron beam evaporation.

The pattern used to create the D2-standard diodes is presented in the figure 3.15 with the diodes' diameters in micrometers. These diodes have been fabricated on a 100 mm 4° off-axis 4H-SiC n^+-type wafer with a substrate of 350 µm thickness, on which n-type epitaxial layer has been grown with a nitrogen doping concentration of 5×10^{15} cm^{-3}. The 10 µm n-epitaxial layer has been implanted by ^{10}B ions at different energies and doses as presented in the previous chapter. A 1.5 µm thick SiO_2 layer has been used as a mask of ion implantation. Then two annealing steps have been carried out in order to activate the dopants (at 900 °C for 120 minutes then at 1650°C for 30 min)[91]. Next, Ni/Ti/Al/Ni 400 µm thick ohmic contacts were deposited by ultrahigh vacuum e-beam evaporation followed by a short annealing step at 800 °C. The final structures of both D2-standard and D2-plasma diodes are illustrated in figure 3.16 and 3.17 respectively.

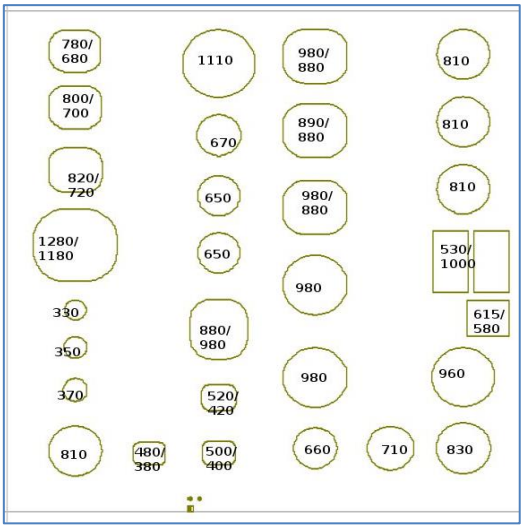

Figure 3.15 Pattern used to realize p-n diode (D2-standard and D3-b diodes). Their diameters are shown in µm

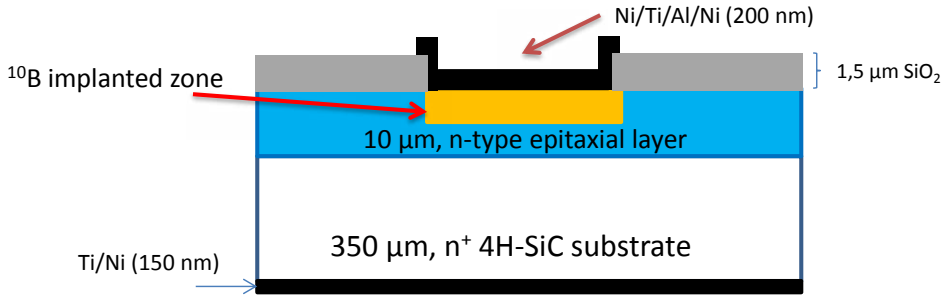

Figure 3.16 Schematic representation of the D2-standard pn diode

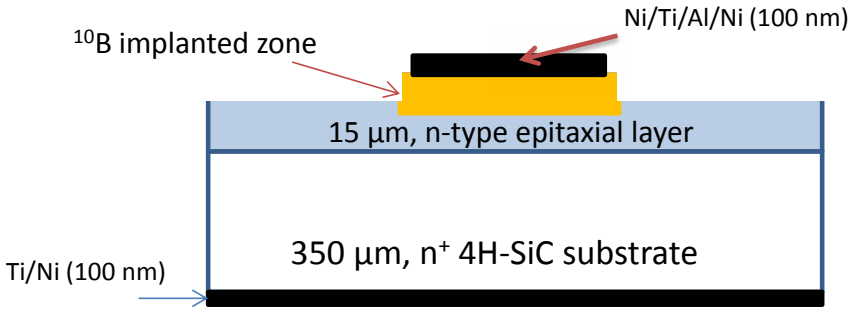

Figure 3.17 Schematic representation of the D2-plasma pn diode

In contrast to the D1-diodes the D2-plasma diodes donot exhibit a junction like *I-V* characteristics as shown in figure 3.19. This can be due to the deposition of the ohmic contact on the whole p+ layer rather than depositing it on its edges leaving a window as it was presented in [83] [84]. From the SIMS analysis done in [84] it was shown a Schottky diode structure under the ohmic contact due to the disappearance of boron whereas a p-n diode structure was shown in the window area . Due to their electrical characteristics such diodes were irradiated only under fast neutrons revealing a non-resolvable signal.

On the other hand, the electrical characterizations of the D2-standard diodes are shown in figure 3.18. It is clear that such diodes possess high leakage current density beside their high resistivity. Although such diodes have high leakage current density they have been irradiated under thermal neutron fluxes revealing resolvable signals.

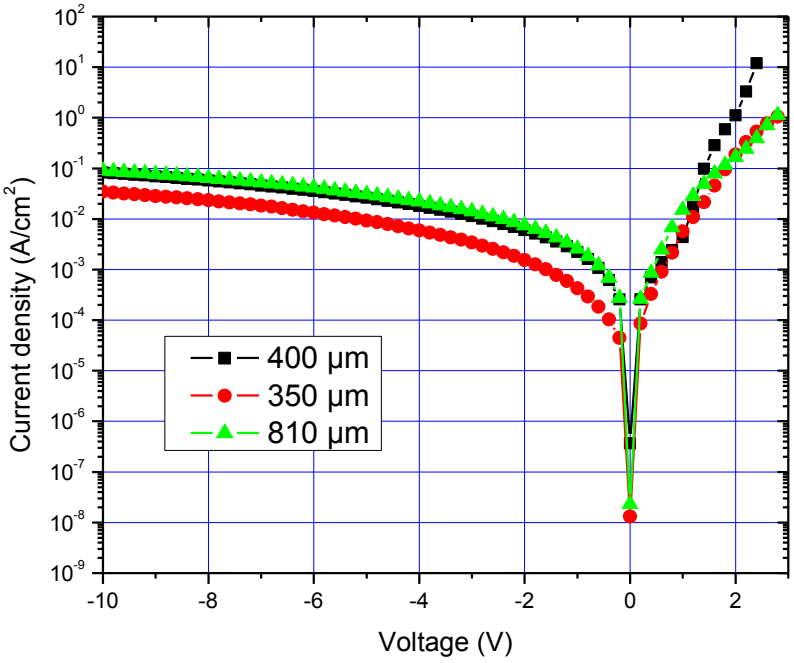

Figure 3.18 Current density of the pn diodes (D2- standard diodes) with different diameters after ^{10}B ion implantation

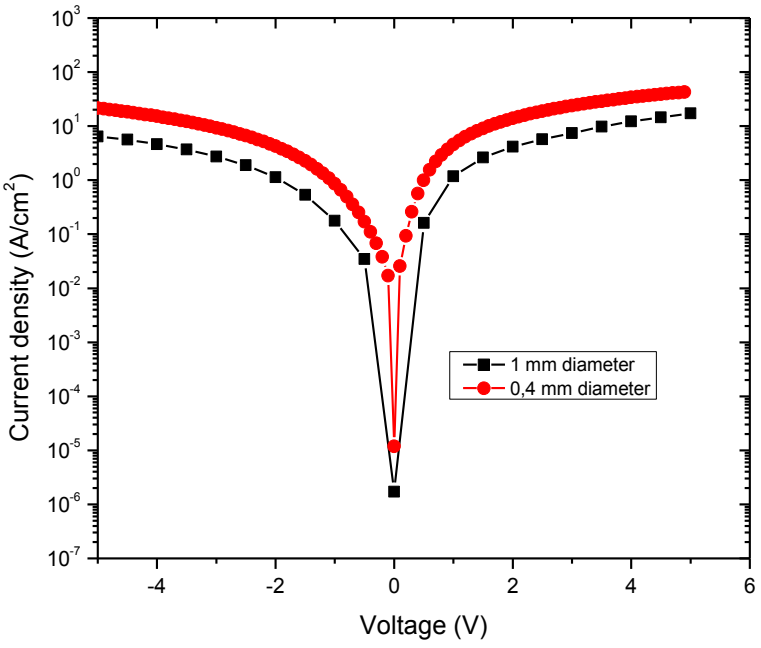

Figure 3.19 Current density of the pn diodes (D2- plasma diodes) with different diameters after ^{10}B ion implantation

3.3 D3-geometry

For the D3 diodes different 4H-SiC wafers have been used. Two types of detectors were realized (D3-a and D3-b) both based on 4H-SiC p^+n junction (see figures 3.20 and 3.21). For D3-a detectors, the p^+n diodes were fabricated with three different areas (4, 10 and 25 mm^2) on commercial 4H-SiC n^+ wafers purchased from Cree Research, where several epitaxial layers have been grown by chemical vapor deposition (CVD). Here we use an 80 µm n-type epitaxial layer with a low nitrogen doping concentration of ~2×10^{14} cm^{-3} covered with a two p-type epitaxial layers p^+ and p^{++} doped with Al, with a thickness of 1 µm each and concentrations of 2×10^{17} cm^{-3} and 2×10^{19} cm^{-3}, respectively. The 4 µm Al metallic contact was sputtered at room temperature on the ohmic contact metallization layer (Ni-Ti-Al-Ni alloy with ~100 nm total thickness).

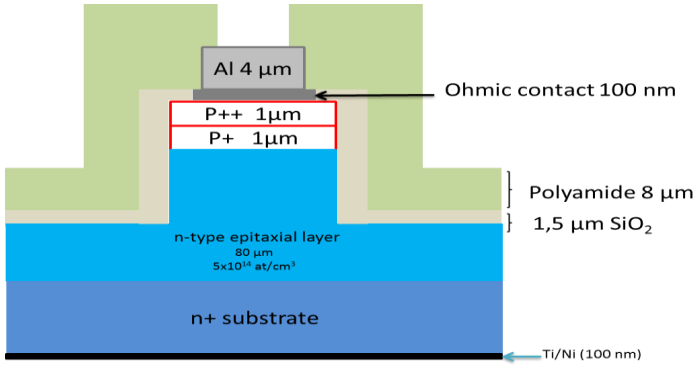

Figure 3.20 Schematic representation of the D3-a pn diode (not drawn to scale)

For the D3-b diodes, the surface area is much smaller than the D3-a diodes in fact as shown in figure 3.15 the same pattern used to realize the D2-standard is also used here. These diodes have been fabricated on a 4H-SiC n^+ wafer purchased from Ascatron with a substrate of 350 µm thickness, on which n-type epitaxial layer has been grown with a low doping concentration of ~2×10^{14} cm^{-3}. The 20 µm n-epitaxial layer is covered by a 1 µm p^+-epitaxial layer with high aluminum doping concentration ~10^{19} cm^{-3}. The individual devices are then defined by etching away the p^+ layer outside the masked areas to form mesa structures. The edges of the sample were etched to a depth of 1.5 µm by reactive ion etching to form a mesa structure. Next the anode ohmic contact (Ni/Ti/Al/Ni) with 200 nm diameter has been deposited by ultrahigh vacuum electron beam evaporation. Finally a 1 µm Al

metallic contact has been deposited by ultrahigh vacuum electron beam evaporation on the top of the anode ohmic contact. A 1.5 μm SiO_2 layer has been used as a masked layer for ^{10}B ion implantation.

Both types of detectors have been implanted by ^{10}B directly into the Al metallic contact in order to create the NCL. The D3-a diodes were implanted by ^{10}B at 2 MeV and a dose of 5×10^{15} cm^{-2} at 400 °C into the thick Al contact layer for thermal neutron detection. Since the Al metallic contact in D3-b diodes is thinner than that for D3-a diodes, ^{10}B has been implanted at lower energy (180 keV) and a dose of 5×10^{15} cm^{-2} in this structure. Finally both types of the 4H-SiC diodes were fixed on alumina substrates and wire bonded to contact pads with 50 μm thick wires to extract the electrical signal.

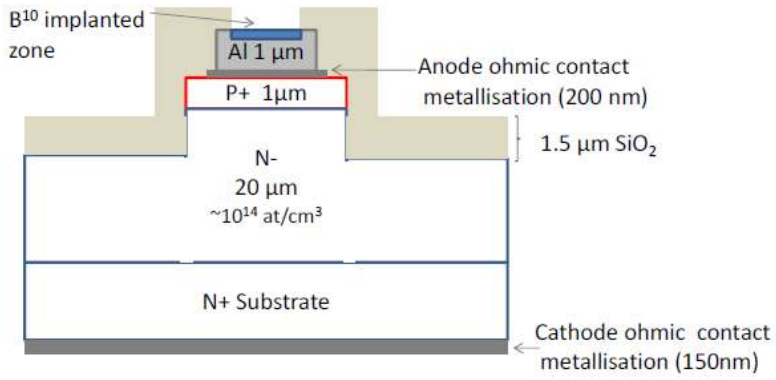

Figure 3.21 Schematic representation of the D3-b pn diode

3.3.1 D3-current voltage measurements

After realizing the D3-detectors the leakage current of each diode as function of bias voltage was measured. The leakage current with respect to the reverse bias, may give an estimation of the signal-to-noise ratio during irradiation of the detectors. The main results of the current-voltage measurement of the D3-a diodes are presented in figure 3.22. The high leakage current density (10^{-4} A/cm^2) indicates that the boron implantation at 2 MeV at 400 °C has induced a considerable amount of leakage due to its diffusion into the SiC epitaxial layer which was confirmed by the SIMS measurement presented in the previous chapter. It is clear that the leakage current density increases with diodes area. This can be attributed to a higher probability of

defects in the active zone for bigger areas. However, the D3-b diodes with and without ^{10}B show a low leakage current density around 2×10^{-8} A/cm^2(see figure 3.23), which means that the ^{10}B ion implantation process at room temperature has not induced a significant leakage.

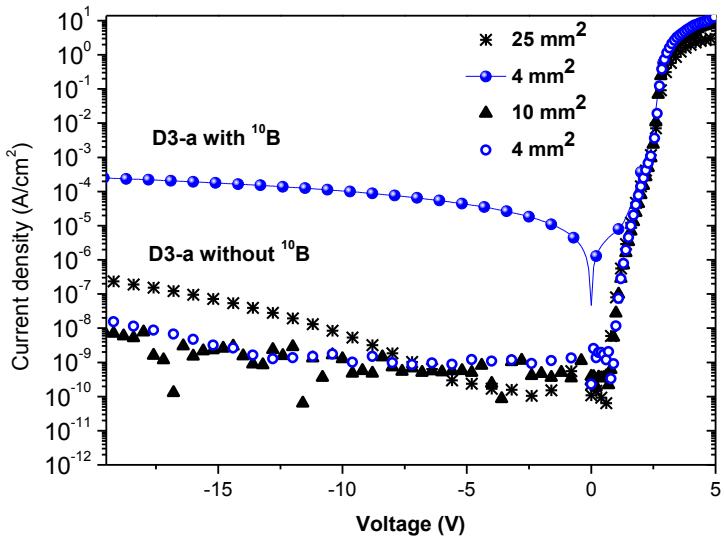

Figure 3.22 Current density of the pn diodes (D3-a diodes) with different areas (before and after ^{10}B implantation)

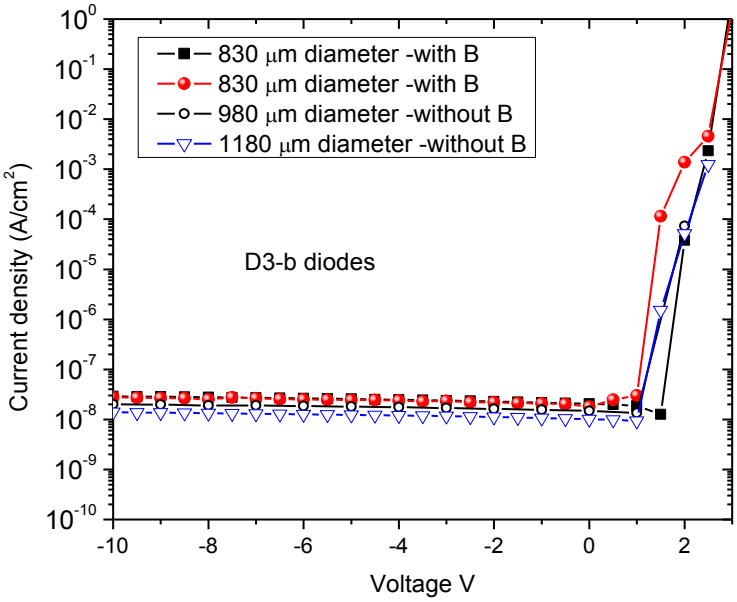

Figure 3.23 Current density of the pn diodes (D3-b diodes) with different areas (before and after ^{10}B implantation)

3.4 D4-geometry

In order to realize the D4 diodes the same technological processes followed to finalize the D3-a diodes are performed here. The only difference for the D4 diodes is that a layer of B_4CN has been sputtered on the top of the Al metallic contact instead of implanting ^{10}B directly into Al layer. The electrical characterizations of these diodes are shown in figure 3.24. The low leakage current of these diodes provides a good evidence for this method in realizing thermal neutron detectors taking into consideration the distance between the NCL and the SCR.

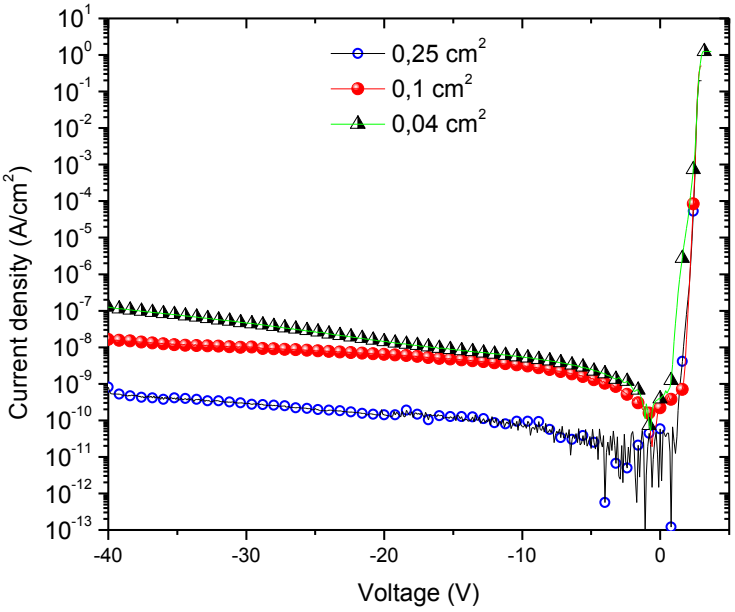

Figure 3.24 Current density of the pn diodes (D4-diodes) with different areas after depositing a 100 nm of B_4CN layer

So far we have presented four new methods of realizing SiC radiation sensors. The first method was based on ion implantation of Al into the 4H-SiC n-type epitaxial layer to create the p+ layer followed by ^{10}B ion implantation to realize the NCL. For the second method, ^{10}B ions have been implanted directly into the n-type SiC epitaxial layer to create the p+ layer and the NCL in a one single process. However ^{10}B ions have been implanted directly into the Al metallic contact to fabricate the D3-detectors. Other than ion implantation, sputtering a NCL based on B_4CN could also be a possible solution to avoid the consequences of the ion implantation process into

a semiconductor. To summarize, all the diodes (except the D2-diodes) show low leakage current density in the reverse bias voltage revealing the interest of such methods in realizing ^{10}B-based NCL. Regardless of the type of the realized detector, it should be pointed out here that good detectors are those not only with low leakage current density but also with resolvable signals indicating a selective radiation detection as it will be illustrated in the next chapter.

This page intentionally left blank

Chapter 4. The Irradiation Tests

As mentioned in the previous chapters the main aim of this work is to prove the feasibility of new methods of realizing SiC-based radiation detectors. However in this chapter and after realizing our diodes we should confirm their performance as radiation detectors. For this purpose the diodes with the best electrical characteristics from each geometry were tested under different types of irradiations. For thermal neutron detection those with ^{10}B-based NCL were used. This ^{10}B-based layer is essential for thermal neutron detection thanks to the high neutron cross section of ^{10}B (3840 barn) with thermal neutrons. The mechanism of thermal neutron detection relies on the charged reaction products (alpha and lithium) that deposit their energies within the detector active volume.

We used the facilities at the BR1 nuclear reactor at SCK·CEN (Belgium) to irradiate the diodes under thermal neutrons. The diodes with ^{10}B respond to thermal neutrons by showing an additional spectral component at high channel numbers which is not the case for diodes without ^{10}B. Such a spectral component disappears immediately as the reactor power reduced to zero indicating the prompt response of such detectors. Furthermore a study of the behavior of each type of detector with bias voltage changes and the effect of the area on the pulse height spectrum are addressed here. In addition as we will see in this chapter thanks to the SRIM simulations performed in this work the D3-diodes have been improved showing a higher signal-to-noise ratio revealing a well-structured pulse height responses with either thermal or fast neutrons.

Besides the thermal neutron irradiations, the diodes were irradiated under fast neutrons at different temperatures up to 150 °C. Such diodes detect fast neutrons where a typical fast neutrons response for SiC detectors was obtained. For the

above-mentioned irradiation tests, four facilities with different irradiation sources were used: the BR1 at the SCK·CEN for thermal neutron irradiations. For the fast neutron irradiations at different temperatures the D-T neutron generators at the Technical University of Dresden (Germany) and at Schlumberger (France) were used. For gamma irradiations, the Linac Mini-Linatron source at CEA Cadarache (France) was used.

4.1 Modes of detector operation

The operation of any radiation detector basically depends on the way the radiation to be detected interacts with the detector itself. In other words, the response of a detector depends on the different interactions which were discussed in chapter 1. Therefore in order for a detector to response to radiation, interaction between the latter and the detector must take place. This will result in an amount of generated electric charges which will be collected to form the basic electrical signal. The charge collection is enhanced by the presence of the electric field inside the detector's active volume which drift the generated positive and the negative charges in opposite directions. The time for fully collecting the charges varies from one detector to another. For instance, the time of collection in semiconductor detectors is of order of nanoseconds which is much faster than that in ion chambers where the time is as long as milliseconds [1]. This is related to the mobility of the charge carriers within the detector's active volume and the average distance that must be travelled before arriving at the collection electrodes.

Typically there are two different modes for measuring nuclear detector signals, current mode and pulse mode. Pulse mode is the most commonly used. However the current mode is used when the event rates are very high; at this stage pulse mode operation becomes impractical. In current mode, the total current of the detector is measured ignoring the pulse nature of the signal. On the other hand, the pulse mode operation allows the individual pulses generated by the particles to be recorded and counted. When operating a detector in pulse mode, the amplitude of each individual pulse carries important information regarding the charge generated by that particular radiation interaction in the detector. The amplitude of each pulse is proportional to the energy deposited in the detector by the interaction causing that pulse [101].

By using an appropriate electronic threshold, one can select and count only amplitude-selected pulses that one intends to observe. Thus in a pulse mode, one can register a pulse height spectrum (PHS) which contains a large amount of information. This is done by the appropriate electronics setup that registers the signal in a predefined energy window. These pulses are digitized and sent to a computer. The computer displays the results as histograms.

However, the most challenging point in the electronics is the presence of noise and the ability to eliminate it from small signals. The threshold level should be set above the noise level. In signal processing, noise is any random signal that is not due to the physical process one intends to measure. Thus the sensor and the electronics should be designed to minimize electronic noise.

4.2 Electronics for radiation detectors

Typically the signal of a semiconductor radiation detector is too small to be detected directly so it must be amplified with low noise electronics. The sequence of detector functions is illustrated in figure 4.1. The detector is connected to a preamplifier which extracts the signal from the detector without degrading the signal-to-noise ratio (SNR). Thus it is preferable that the preamplifier to be as close as possible to the detector to reduce input capacitance caused by cabling and to decrease radio frequency pickup, all of which are sources of noise for the charge-sensitive preamplifier (CSP) [102][103] . The detector current is momentarily integrated on the capacitance of the CSP. Then the capacitance will discharge through the resistance of the CSP, returning the voltage across the load resistance to zero. The output voltage from the preamplifier has an amplitude V_{max} which is given by the expression:

$$V_{max} = \frac{Q}{C} \tag{4.1}$$

It can be seen from the above equation that the amplitude of the signal pulse is directly proportional to the corresponding charge generated (Q) within the detector. This is true because the feedback capacitance (C) of the CSP is constant. Because

CSP integrates the charge on the feedback capacitor, its gain is not sensitive to a change in the detector capacitance.

Therefore detector operation in the pulse mode consists of a sequence of individual signal pulses where each pulse reflects the interaction of a single quantum of radiation within the detector. Furthermore, measuring the rate at which these pulses occur gives the corresponding reaction rate within the detector. Moreover, the amplitude of each individual pulse is proportional to the charge generated (Q) within the detector which is related to the energy deposited due to each individual interaction through the following expression:

$$Q = \frac{E}{\varepsilon} e \tag{4.2}$$

where E is the absorbed energy within the detector active volume, ε is the energy required to create an electron-hole pair which is 7.78 eV in SiC and e the electron charge. Therefore recording the distribution of the pulse amplitudes gives information on the energy of the incident radiation. This is achieved by displaying the pulse amplitude information through a PHS.

To accelerate the decay time of the pulses, the CSP output is connected into a shaping amplifier which amplifies and reshapes the output pulses. The preamplifier output is fed into an amplifier not only for further amplification but also for reshaping the output signal from a detector. Signals that may be buried in the noise appear clearly above the noise after the shaping stage. The frequency spectra of the signal and the noise are different, so one can improve the SNR ratio by applying a filter that tailors the frequency response to favor the signal, while attenuating the noise. Then by using an analogue-to-digital converter (ADC) which is one of the basic components of a multichannel analyzer (MCA) [1] the analogue signal (pulse amplitude) is digitized. The ADC has a specific number of bins into which the pulses are sorted. These bins are the channel numbers in the PHS.

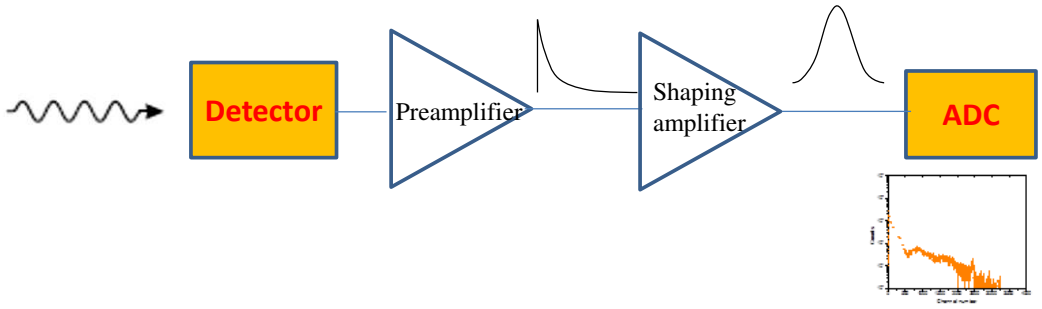

Figure 4.1 Basic detector functions: Radiation interacts with the detector and is converted into an electrical signal. This low-level signal is integrated by the preamplifier, then fed into a pulse shaping amplifier and digitized for storage and analysis.

4.3 Thermal neutron irradiation

In order to study the response of the realized detectors under thermal neutron flux, we used the facilities at the BR1 nuclear reactor at SCK·CEN. It is a gas-cooled research reactor. It has been in operation since 1956 and it is based on natural uranium with a graphite moderator and can provide a thermal power up to 4 MW.

Four diodes were placed in an aluminum box for electromagnetic shielding (see figure 4.2). Then each diode was connected into its own coaxial cable of 3 m length, allowing the connection of each diode to a charge sensitive preamplifier located on the top of the reactor. Then the aluminum box was placed into the spherical cavity of the BR1 reactor through an aluminum tube. This was installed such that the 4×3×10 cm^3 aluminum box with four diodes will be positioned in the center of the cavity when resting on the closed bottom of the tube as shown in figure 4.3. At this location, the gamma dose rate is about 1 Gy/h, the fast neutron flux is negligible compared with the thermal neutron flux which is 7×10^8 n/cm^2s at 700 kW reactor power. The temperature is around 25 °C. The diodes were irradiated at different reverse bias voltages from 0 to -250 V. The output signal from the preamplifier was fed to a spectroscopic amplifier and the pulses were recorded with a multichannel analyzer system and with a digital oscilloscope.

Figure 4.2 The aluminum box used to irradiate four diodes attached to their alumina plate. Each diode is connected into its own coaxial cable

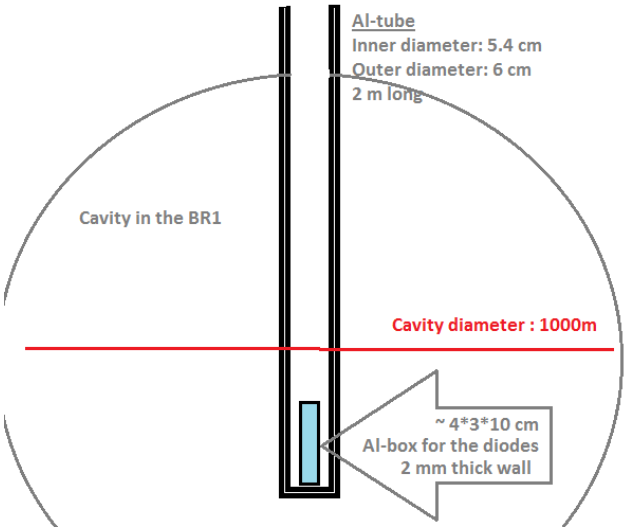

Figure 4.3 Schematic presentation of the spherical cavity used to irradiate the diodes within their aluminum box [104]

4.3.1 First acquisition system

The D1 and D3-a diodes were tested under thermal neutron irradiation in the BR1 reactor [105]. The diodes were placed inside an aluminum box for reducing the noise contribution. Then each diode was connected to CSP from GSI Darmstadt through a coaxial cable of 3 m length. Then the CSP is connected to a shaping amplifier. A CAEN N471 dual high voltage supply is located on the top of the reactor. The

preamplifier output was sent to a CAEN desktop digitizer (DT5720) which serves as a multichannel analyzer.

4.3.1.1 Influence of the external reverse bias

The diodes with and without ^{10}B were irradiated at different reverse bias voltages and at different reactor powers. The PHS of the D1-diodes without and with ^{10}B at different reverse bias voltage are shown in figures 4.4 and 4.5 respectively. The diodes with ^{10}B show an additional spectral component at higher channel number which is not observed in the case of the diodes without B this is clearly related to the reactions induced in the NCL. However for D1-diodes with and without B there are two spectral components at the lower channel number (below channel number 500). The first spectral component could be attributed to some noise and gammas. The gammas are referred to the radiative capture of thermal neutrons by Si and C atoms (as well as with Al atoms of the surrounding box). The second component is independent of the bias voltage (beyond -50 V) which means that it is not related to gamma or beta detection as these radiations have long projected ranges. More detailed discussion on this component will be addressed in the next sections.

A comparison between the PHS of the D3-a diodes with and without ^{10}B at different bias is shown in figure 4.6. The features of the PHS of the D3-a diodes are not well defined as these diodes have shown higher noise. Thus two peaks appear for the diodes with ^{10}B and one single component for the diodes without ^{10}B. The first component could be related to gammas because it is bias voltage dependent.

It is known that the active layer thickness of a diode increases with the external reverse bias until the maximum thickness is reached, resulting in maximum collection of charges. This explains the increase of the count rate in the low-energy channels as function of the external reverse bias as shown in figures 4.5 and 4.6. The effect is not well observed in the thermal neutron-induced peak, since at zero bias voltage the active layer is thick enough to detect nearly all the alpha particles. This is not the case for the D1-diodes as was shown in chapter 2 from SRIM simulations (figures 2.16 and 2.17) where the SCR increases with the reverse bias leading to more charge collection. However due to the parameters of this used acquisition system the relevant higher channels are truncated, which is not the case in the secondly used acquisition system as will be seen later.

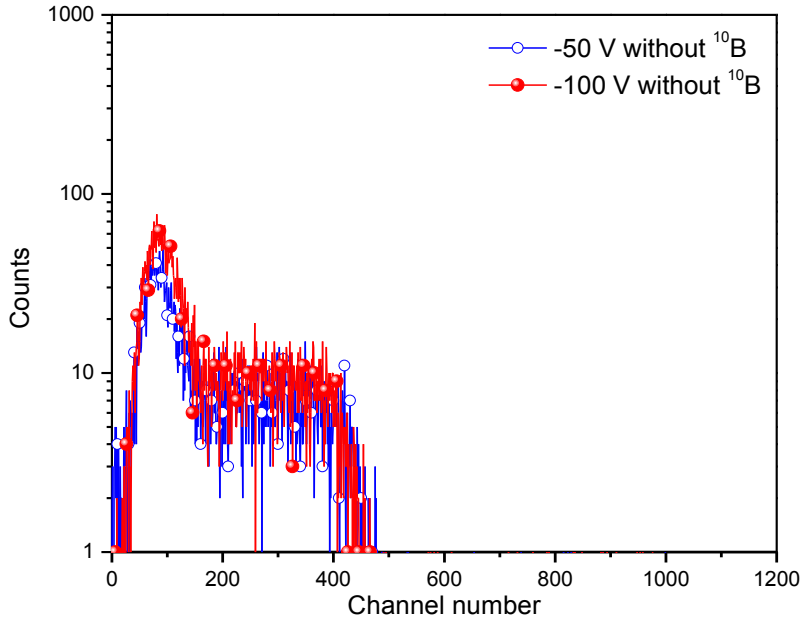

Figure 4.4 Output spectra under thermal neutron irradiation for the D1-diodes of 0.4 mm diameter and without ^{10}B-based NCL

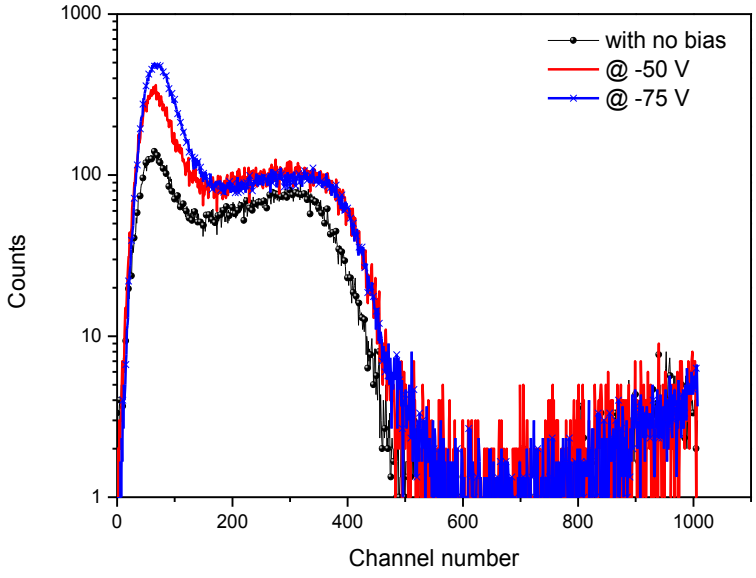

Figure 4.5 Output spectra under thermal neutron irradiation for the D1-diodes of 1 mm diameter and with ^{10}B-based NCL

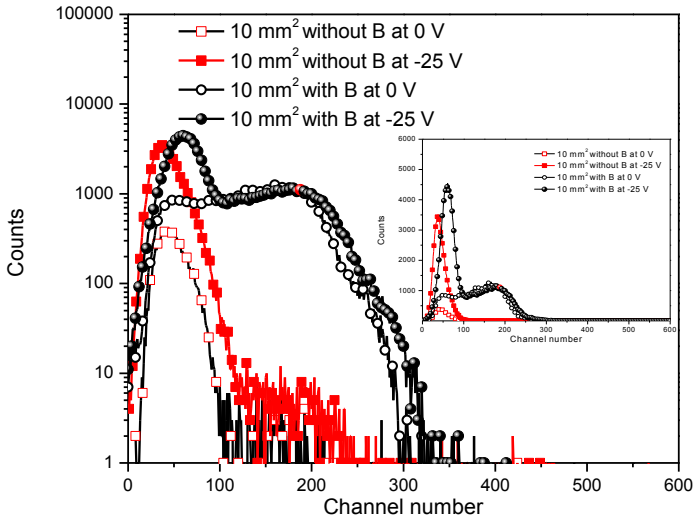

Figure 4.6 Thermal neutron detection spectra measured using D3-a diodes (10 mm^2) with and without ^{10}B-based NCL at 0 V and -25 V

4.3.1.2 Influence of the diodes' area

It is obvious that as the area of the diode increases, the count rate in the thermal neutron-induced peak increases due to higher reaction rate as shown in figures 4.7 and 4.8. Moreover, it is expected that the counting rate in the thermal neutron-induced peak is linear with the nuclear reactor power as well as with the thermal neutron fluxes as shown in figure 4.9. It is noticeable that the diode with ^{10}B based-NCL shows higher counting rate compared with the diode without ^{10}B based-NCL.

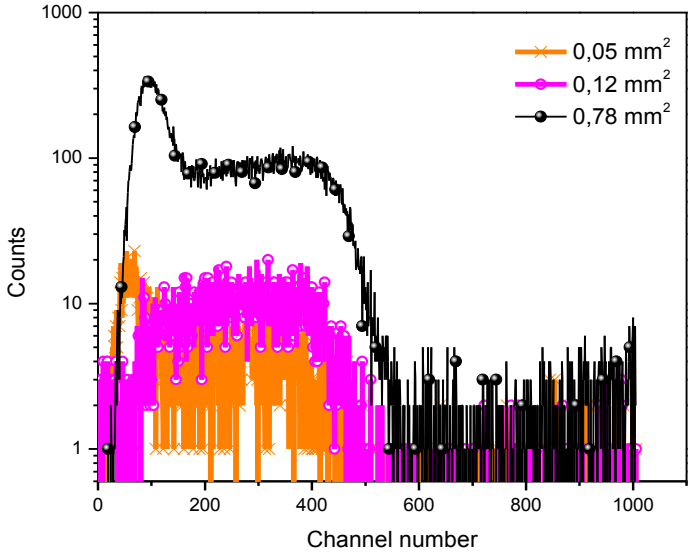

Figure 4.7 Thermal neutron detection spectra measured with D1-diodes(with ^{10}B based-NCL) having different areas at -25 V

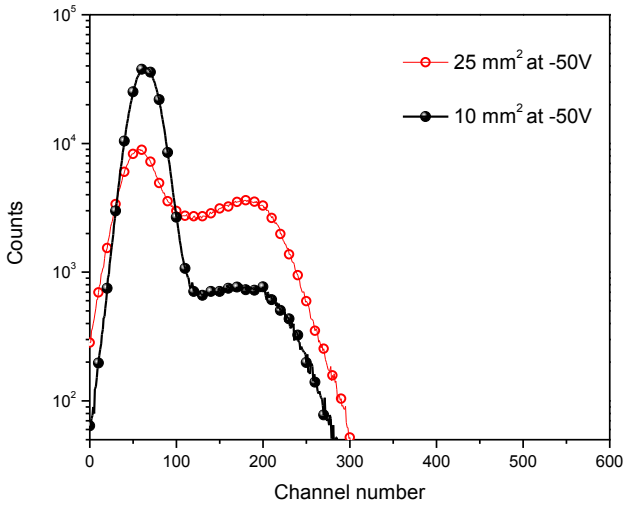

Figure 4.8 Thermal neutron detection spectra measured using D3-a diodes of different areas (10 mm² and 25 mm²), having ^{10}B-based NCL at -50 V

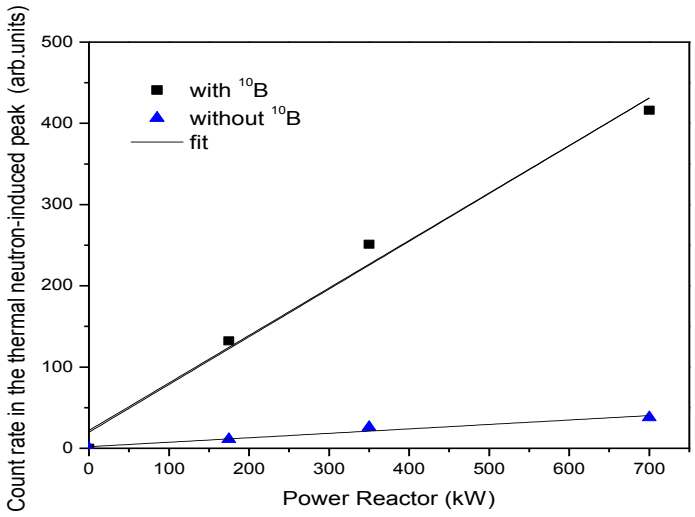

Figure 4.9 Linear response obtained at 0V for the 4H-SiC D3-a diodes with and without ^{10}B-based NCL, both diodes are of 10 mm²

4.3.2 Second acquisition system

Using a new acquisition system with lower noise and better adapted for processing the signals of our detectors we were able to improve the features of the PHS. Using this system the pulses were analyzed by an integration procedure based on the pulse

shape (more specifically the pulse decay time that is determined by the CSP). In this manner the noise components in the PHS are significantly reduced

For this setup we used one Lemo cable for each diode, which made a 50 Ω connection between the diodes and the 4-channel CAEN charge-sensitive preamplifier A1422 (400 mV/MeV for Si). The preamplifier output was sent to a 2-channel CAEN desktop digitizer (DT5780), which provides also the voltages to bias the diodes via the preamplifier. The DT5780 was controlled by CAEN computer software, which also served as a multichannel analyzer. Using this acquisition system, most of the realized diodes were tested and a comparison between the D3-a and D3-b diodes was studied concerning the improvement parameters in realizing such detectors. Although the D2-standard diodes show high leakage current density, they were also tested. A study of the PHS under different bias voltages and with different diode areas and reactor power are addressed here.

It should be pointed out here that the used parameters of the data acquisition system are crucial to be well adjusted otherwise the interested pulses will be lost. For example the threshold level is one of these parameters in the acquisition system. It is defined as the level at which the amplitude of the preamplifier output signal should reach to be triggered. The threshold level is expressed in LSB which is the voltage in a one channel number which is in this case and for thermal neutron irradiation was adjusted to 0.085 mV. It can be noticed that different threshold levels with the same detector irradiated under the same conditions result in PHS with different structures especially in the lower channel numbers as illustrated in figures 4.10 and 4.11. For example in figure 4.10 a very high threshold level (500LSB) results in a truncated PHS at low channel number. On the other hand, using very low threshold level in this case 200 LSB, the acquisition system will be overloaded with noise leading to a lower count rate in the pulses of interest. It is worth noting that the optimal threshold level can differ from one diode to another depending on the noise level of the measured diode. In what follows the PHS drawn on the same figure were obtained with a same threshold level in order to remove any confusion in analyzing the data. All the PHS were measured within an accumulation time of 600 s.

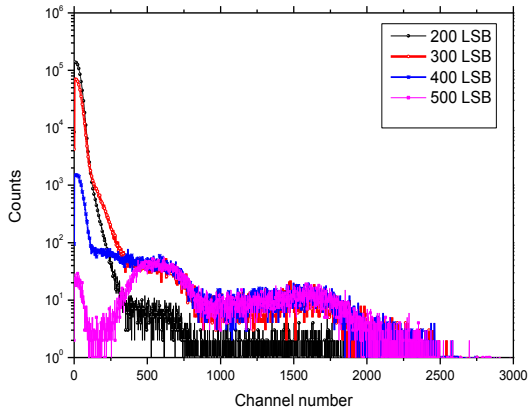

Figure 4.10 PHS with different threshold levels used for the D3-b diode (with ^{10}B- based NCL) irradiated under the same conditions at 0V

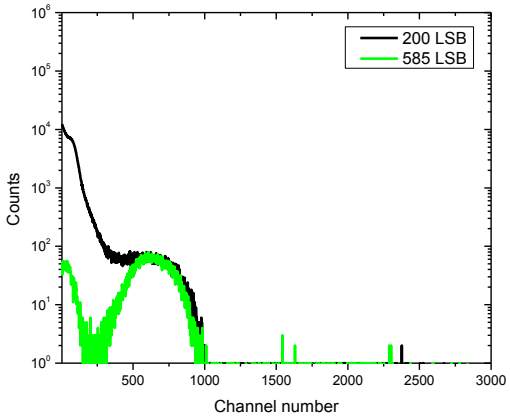

Figure 4.11 PHS with different threshold levels used for the D3-b diode (without a layer of boron) irradiated under the same conditions

4.3.2.1 Influence of external reverse bias

The PHS of D3-a diodes tested under thermal neutrons for 10 minutes at different bias voltages without and with B are shown in figure 4.12 and 4.13 respectively. The PHS of the D1 diodes with ^{10}B are shown in figure 4.14. Although the measured diodes are with different geometries, the features of their PHS are somehow comparable.

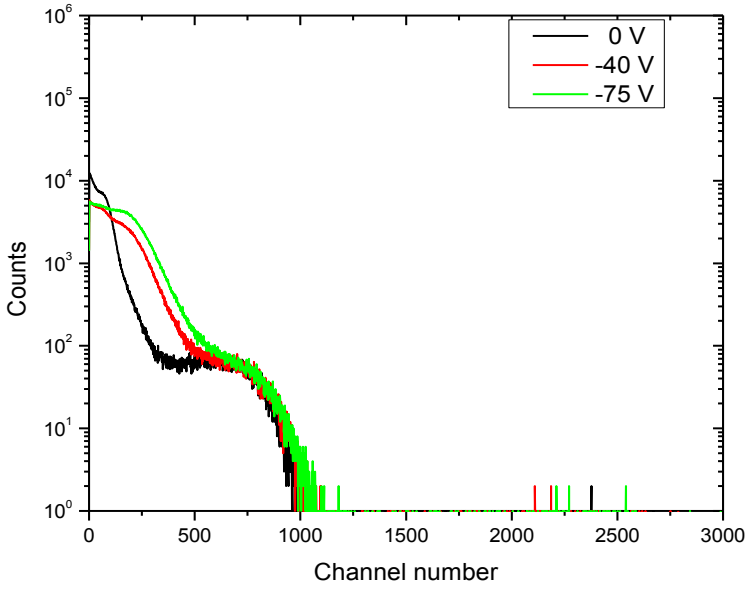

Figure 4.12. PHS measured with D3-b-diodes without ^{10}B based-NCL at different bias voltages (200 LSB)

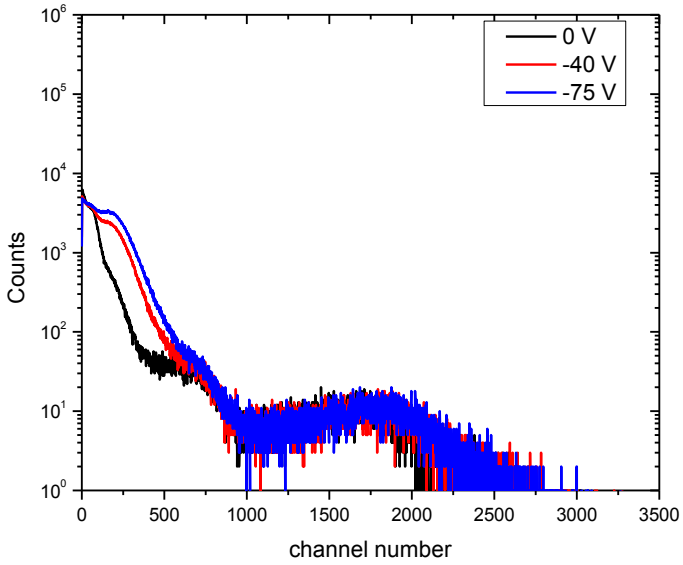

Figure 4.13 Thermal neutron detection spectra measured with D3-b diodes with ^{10}B -based NCL at zero bias, -40 V and -75 V bias.

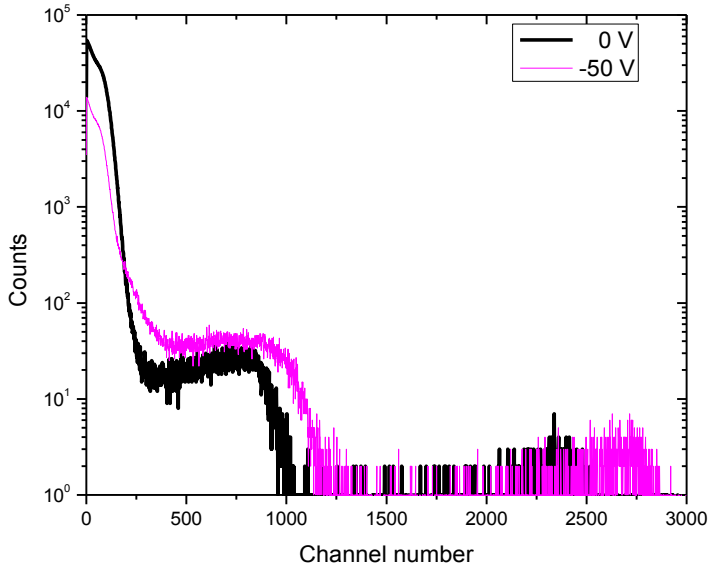

Figure 4.14 Thermal neutron detection spectra measured with D1 diodes with ^{10}B based-NCL at zero bias and -50 V

It can be seen that three spectral components are obtained in diodes with and without B. An additional component at higher energy (higher than channel number 1000) exists only in diodes with ^{10}B. The first component which is at low energy up

to channel number 80 (this value depends on the noise level of each diode) is attributed to noise. This component does not increase with the applied reverse bias voltage. However in some diodes it is seen that increasing the reverse bias voltage results in an improvement of the SNR.

Depending on each diode, the second component is roughly between channel numbers 80-600, and it can be contributed to gammas or betas. This is due to neutron capture by ^{27}Al (aluminum from the box or the 2 m long Al tube) which decays by beta emission (energy between 0 and 2.9 MeV) and gamma rays (1.78 MeV). Both of these emissions could contribute to the second component of the PHS. This can also be confirmed by the dependence of this component on the bias voltage because betas and gammas are highly penetrative. Thus increasing the width of the SCR will result in a higher energy deposited in the SCR as it is the case here. This component clearly increases with the applied bias voltage as shown in figures 4.12, 4.13 and 4.14. It is increasing linearly with the width of the SCR until it saturates at the border of the n-type epitaxial layer. The SCR thickness is dependent on the bias voltage (see figure 4.15) according to the following formula:

$$W = \sqrt{\frac{2\varepsilon_r \varepsilon_0}{q}\left(\frac{N_D + N_A}{N_D N_A}\right)(V_b + V_R)} \tag{4.3}$$

where V_b is the built-in potential given by:

$$V_b = \frac{K_B T}{q}\, ln\left(\frac{N_A N_D}{n_i^2}\right) \tag{4.4}$$

where N_A and N_D are the accepter and the donor concentrations respectively. n_i is the intrinsic carrier concentration, K_B ,T and q are the Boltzmann constant (1.38×10^{-23} J/K), the temperature and the electron charge respectively.

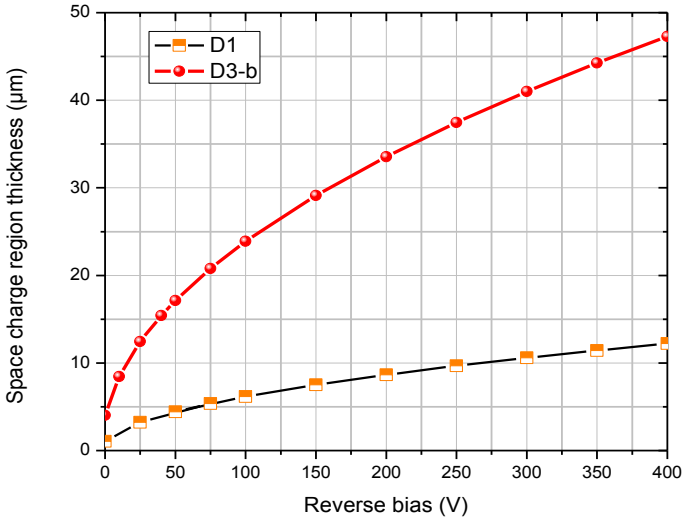

Figure 4.15 Width of the SCR in D1and D3-b diodes as a function of the applied reverse bias voltage

If we count the events between channel numbers 50-700, a linearly dependent count with the SCR is obtained for the D3-b diodes. Moreover the counts increase with applied bias voltage until the 20 μm n-epitaxial layer is reached, this explains the no more increase above this value. On the other hand, the last two spectral components are not affected by the applied voltage as illustrated in the inset of figure 4.16. This indicates that the last two components are related to charged particles with a specific range shorter than 4 μm.

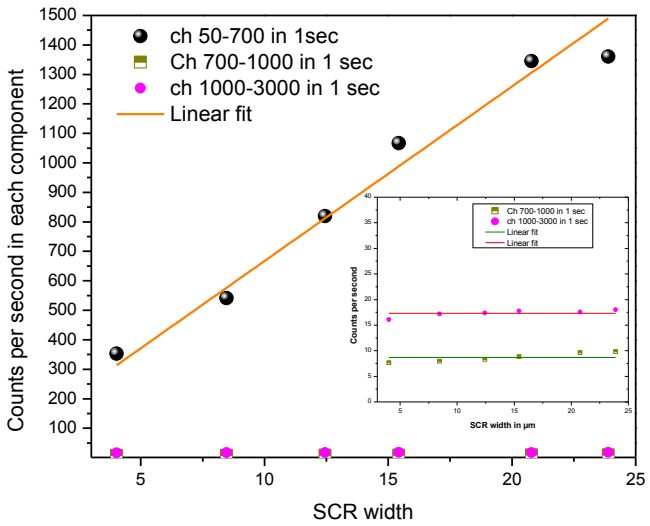

Figure 4.16 The counts per second as function of SCR thickness for pulses in the three components of the PHS

The third component lies roughly between channels 700-1000. This component exists in diodes with and without B. Thus it is not attributed to charged particles produced via ^{10}B interactions. Moreover this peak is independent of the applied bias voltage only in D1 diodes where the SCR is already thin (~1 μm) with no bias voltage. This excludes the possibility that this component is gamma or beta-related. Thus it should be related to charged particles with a specific range where no more energy can be deposited even within a wider SCR. Further measurements were performed on such diodes but without the Al box, and this component still exists. This proves that it is not induced by the used box. Although thermal neutrons could be detected via the boron-rich layer, very few reactions (scattering) could take place with Si and C atoms (low cross section) which excludes the possibility that this component is based on the direct interactions with the diode compositions. As we will see later, such a component disappears immediately after the reactor SCRAM (immediate shutdown of the reactor) which means it is something not related to the electronics.

The fourth component (higher than channel 1000) is obtained only in diodes with ^{10}B revealing the thermal neutron detection. For the D1 diodes this component is bias voltage dependent. In fact in the D1 diodes the SCR is about 1μm at zero bias so increasing this thin SCR to 4.42 μm at -50 V leads to more charge collection and to a shift of the peak into higher channel numbers. Further increase in the width of the SCR (6.17 μm at -100V) results in no more energy deposited in this component because the thickness of the SCR is greater than the range of the charged particles (3.9 μm for alphas at 1.78 MeV).

However, this is not clearly seen in the D3-b diodes where the SCR is already thick enough (~4.02 μm) without any external bias to collect most of the produced electron hole pairs. Due to the larger distance between the SCR and the NCL (about 1.3 μm) in the D3-b diodes, the charged particles from the ^{10}B-based NCL-related interactions enter the SCR with a wide distribution of energies leading to a wider component. This is in contrary to the D1 diodes where the NCL and SCR are closer to each other (~0.5 μm). This could explain why the different components in the D1 diodes are well separated.

Although the PHS of the D2 diodes show more or less the same features of the D1 and D3-b diodes (four components), the behavior of all the observed peaks is not affected by the applied bias voltage. This is maybe due to the higher leakage current with the applied bias voltage as was shown in the previous chapter. Also such diodes showed higher noise level than the D1 and D3-b diodes during the measurements. In addition, the D2 PHS (see figure 4.17 and 4.18) are not exactly reproducible as it was the case in other diodes.

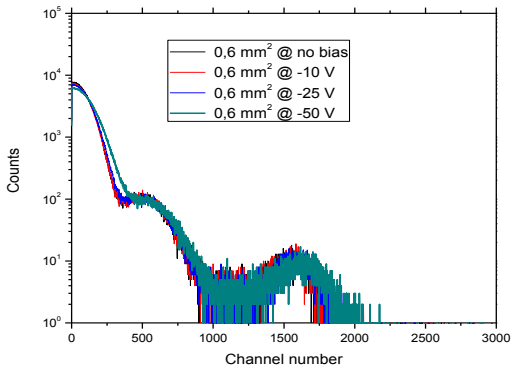

Figure 4.17 PHS measured with D2-standard diodes at different bias voltages (0.6mm^2)

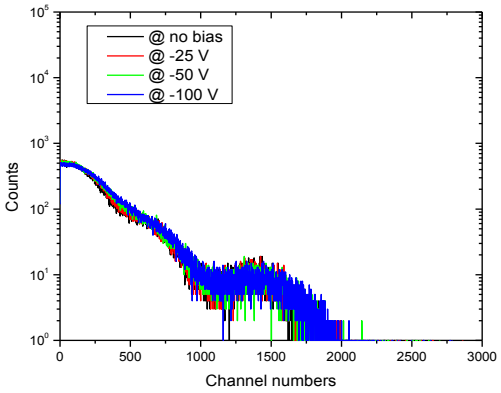

Figure 4.18 PHS measured with D2-standard diodes at different bias voltages (0.5 mm^2)

The D3-a diodes have been measured under thermal neutron fluxes at different bias voltages (see figure 4.19). During the measurements the D3-a diodes show a lower signal-to-noise ratio compared to D3-b and D1 diodes. This can be attributed to the higher leakage current density. If we compare the D3-a and D3-b pulse height spectra it is clear that the signal from D3-b diodes is more readable and with more features, reflecting the high quality of these diodes (low leakage current and low noise level). Thanks to the SRIM simulations performed in this work the D3-diodes have been improved to show well defined components and a high SNR [106] [107].

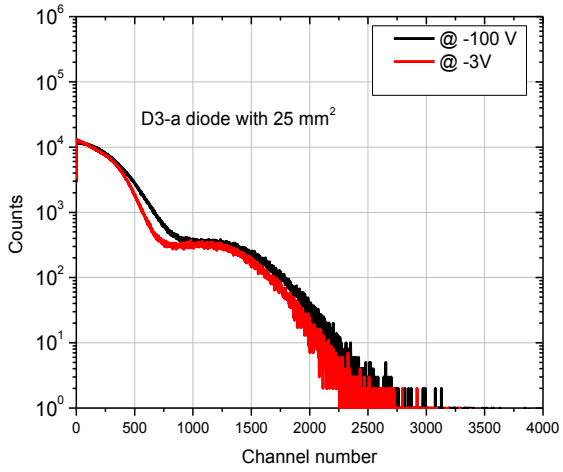

Figure 4.19. Thermal neutron detection spectra measured with D3-a diodes with ^{10}B based-NCL at -3V and -100 V.

As mentioned in the previous chapter that some diodes (D4-diodes) were realized by sputtering a layer of B_4CN on the top of D3-a diodes. These diodes are initially either containing a boron implanted layer or not. The PHS of such diodes under thermal neutron irradiation are shown in figures 4.20 and 4.21. It can be seen that the diodes with two NCL show higher counting rate beyond the channel number 1000 (figure 4.21). However the diodes with only one layer of B_4CN show low counts at channel numbers 1000-2000. This is related not only to the thin boron layer used but also to the distance between the NCL and the SCR which is already greater than the range of alpha and lithium ions in the diodes' material.

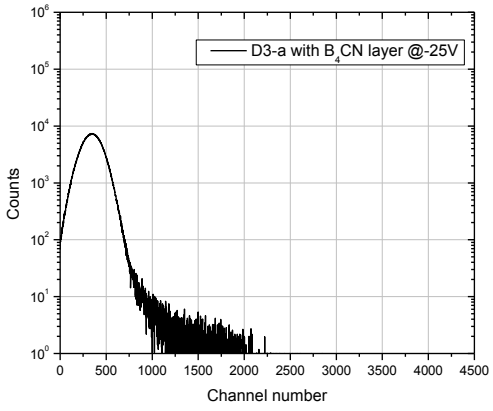

Figure 4.20 PHS measured with D4 diodes (4 mm^2)with a layer of B4CN

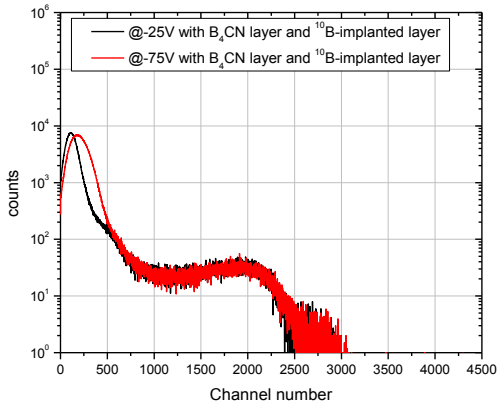

Figure 4.21 PHS measured with D4 diodes (4 mm^2) with ^{10}B based-NCL and a layer of B4CN

4.3.2.2 Influence of the diodes' area

Additional measurements on D3-b diodes with different areas and D1 diodes with different diameters (1 or 0.4 or 0.25 mm) indicate that the count rate scales with the area of the diode. This confirms the sensitivity and feasibility of the realized detectors. The PHS of the D3-b diodes with different areas (0.75 and 0.33 mm^2) are shown in 4.22 indicating a higher counts with a bigger area. The count rates for three diodes with different areas are shown in figure 4.23. The total number of counts increases with the applied bias voltage. Similar behavior observed in D1 diodes with different areas is shown in figures 4.24 and 4.25.

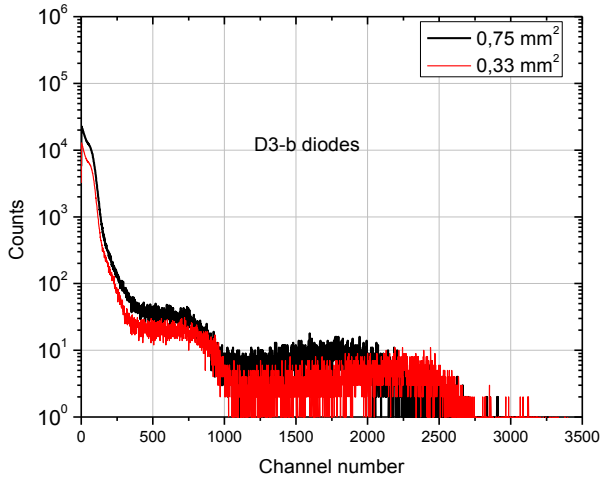

Figure 4.22 Thermal neutron detection spectra measured with D3-b diodes (with ^{10}B based-NCL) with different areas without applying external bias

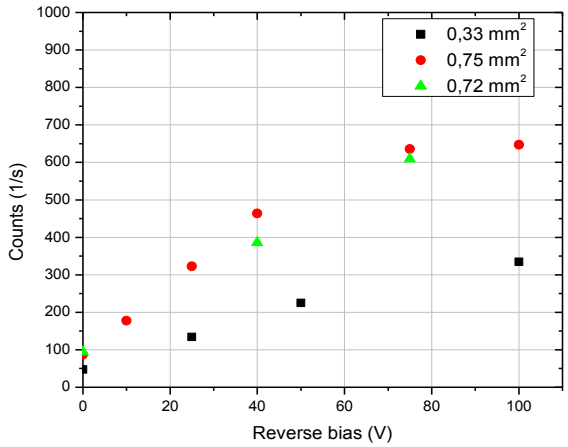

Figure 4.23 Total count rate of D3-b diodes with different diameters above the threshold level as function of an external bias voltage

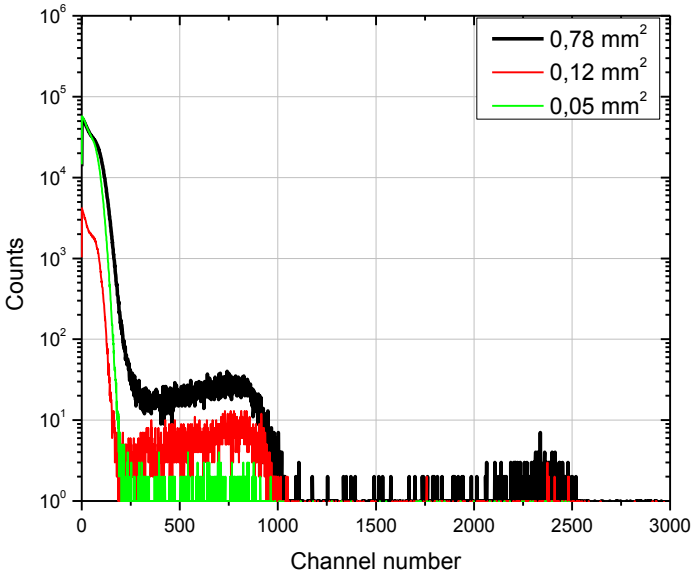

Figure 4.24 Thermal neutron detection spectra measured with D1-diodes (with ^{10}B-based NCL) having different areas without an external bias

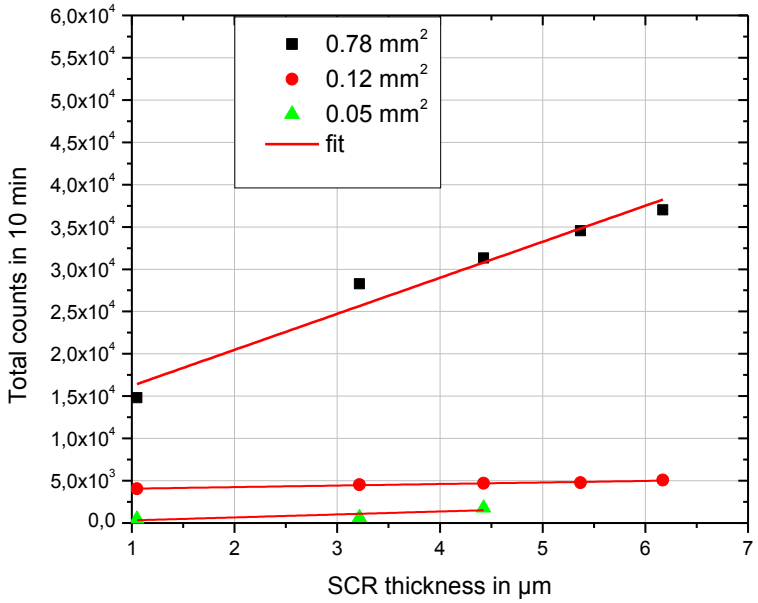

Figure 4.25 Total counts above the threshold level (300 LSB) in D1 diodes over 10 min with diodes having different areas as function of the SCR thickness

4.3.2.3 PHS at different reactor power

To study the sensitivity of the D3-b diodes with respect to the variation of the thermal neutron fluxes such diodes have been irradiated at different reactor powers either at 700 kW or 350 kW (3.5×10^8 n/cm^2·s) or even at 0 kW. Furthermore, a study of the variation of the counts in each spectral component during the reactor shutdown was done. This was achieved by taking time differential data immediately after a sudden stop of the reactor.

The PHS were recorded each one minute before and after reactor SCRAM. It was noticed that the noise component drops very slowly after the SCRAM. However the second component consists of two parts one disappearing immediately when the reactor power goes to zero. This could be referred to gammas which are generated either by the reactor or as a result of some neutron capture within the detector or its surroundings. The second part decays with half-life of 2.25 minutes. This is attributed to the half-life of ^{28}Al. In fact ^{28}Al is formed after neutron capture by ^{27}Al (^{27}Al from the aluminum box and the surroundings of the diode) which decays by emitting beta (energy between 0 and 2.9 MeV) and gamma (1.78 MeV). Both of these could contribute to the second component.

By reducing the thermal neutron fluxes by a factor of 2, the count rate in the fourth component (^{10}B-related component) is also decreasing by roughly the same factor. Moreover a linear change in the counting rate in the thermal neutron with the reactor power was found as illustrated in figure 4.27.

In addition after the immediate SCRAM of the reactor the third and fourth peaks which are related to neutron interaction instantaneously disappear (see figure 4.26). The immediate disappearance of these two components indicates the prompt thermal neutron detection coming from the reactor. Based on the above discussion discrimination between gamma and thermal neutrons in one single detector is feasible.

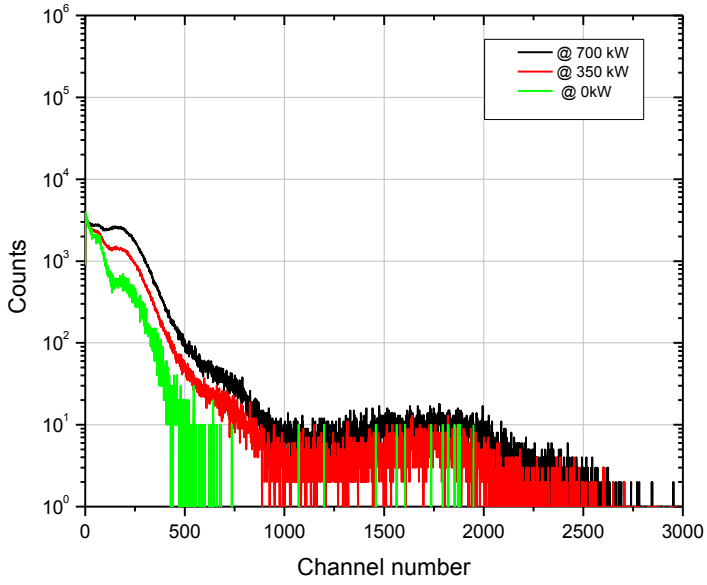

Figure 4.26 The response of the D3-b diode at different power reactor and after the immediate SCRAM of the reactor

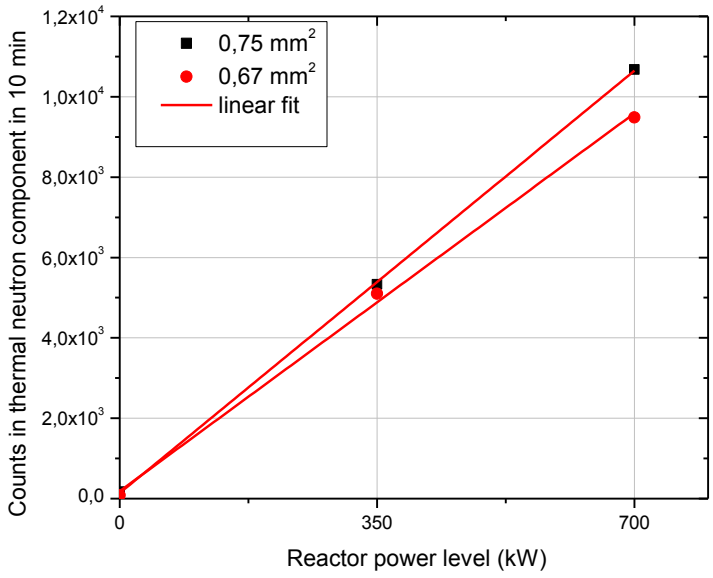

Figure 4.27 4H-SiC D3-b diodes response at 0V as a function of reactor power. Count rate is linear with reactor power and thus with neutron fluence rate.

4.3.3 Efficiency of a detector

An important characteristic of a detector is its efficiency, which is defined as the probability that a particle which passes through the detector is seen by it. This efficiency η can vary considerably depending on the type of a detector and radiation. For instance, charged particles in scintillation counters or gas detectors or in semiconductor detectors are seen with a probability of 100% while γ rays are measured in gas counters with low probabilities of the order of 1 % [101].

The efficiency also depends on the volume and shape of the detector material, absorption cross-section in the material, and attenuation layers in front of the detector. Therefore different detection efficiencies (absolute, intrinsic and full-energy peak efficiency) are defined to take into account these parameters. Restricting our discussion to the absolute efficiency which is defined as the ratio of the number of counts recorded by the detector (N_c) to the number of radiation (N_s) emitted by the source (in all directions), as given by the following formula:

$$\eta_{absolute} = \frac{N_c}{N_s} \tag{4.5}$$

Taking the total counts above the threshold level for D3-b diodes at self-bias voltage and the neutron flux emitted by the source (7×10^{8} n.cm^{-2}.s^{-1}) the efficiency can be approximated as 1.4×10^{-7} cps/n.cm$^{-2}\cdot$s^{-1}. Increasing the bias voltage up to -100 V increases the total efficiency by a factor 6. This increase in the efficiency is of course related to the greater efficiency for gammas and betas with the applied bias. Not only does the bias voltage increase the detector efficiency but an increase of the detector's area may also reveal a higher efficiency. This can be illustrated as follows by the relation between the reaction rate and the area of the detector.

Furthermore, in our case the efficiency of the used detector increases with using a NCL. Thus the reaction rate is calculated as follows [101] :

$$R = \emptyset \times \sigma \times N \tag{4.6}$$

where the N is the number of target nuclei (^{10}B ions in our case), σ is the reaction cross section (3840 barn) and Φ the flux of the source. Evaluating these values one finds that there are about 100 reactions per second taking place. However if one sums up the counts starting from channel 1000 (^{10}B related component) there are about 17 cps. Therefore the efficiency in detecting the charged particles from the $^{10}B(n,\alpha)^{7}Li$ reaction is about 17 %. This is an underestimation since not all the created charged particles will enter the SCR to be detected and some of the counts could contribute to lower channel numbers.

4.4 Fast neutron irradiation

4.4.1 High fast neutron flux

To test the diodes under fast neutrons we used a deuterium-tritium (D-T) neutron generator which typically produces neutrons with energy around 14 MeV depending on the angle from the tritium source and with a flux of the order of 10^{10} n/s for 4π. This source depends on the deuterium-tritium fusion reaction. Using this neutron generator of the Technical University of Dresden (TUD-NG) we tested most of the realized detectors. The distance between the source and the detectors is about 7 cm. The detectors were placed inside Al box (3.5 cm × 4 cm). Then the diode to be measured is connected into CAEN A1422 CSP through a 50 Ω coaxial cable.

To reduce the noise level the CSP was placed as close as possible to the detector. The signal processing was performed using a CAEN digitizer DT5780 which serves as a multichannel analyzer. In order to heat the diodes, ceramic heating plates supplied by Rauschert GmbH were used. These heating plates were placed in a macor box as shown in figure 4.28. The temperature was changed from room temperature (RT) up to 155 °C.

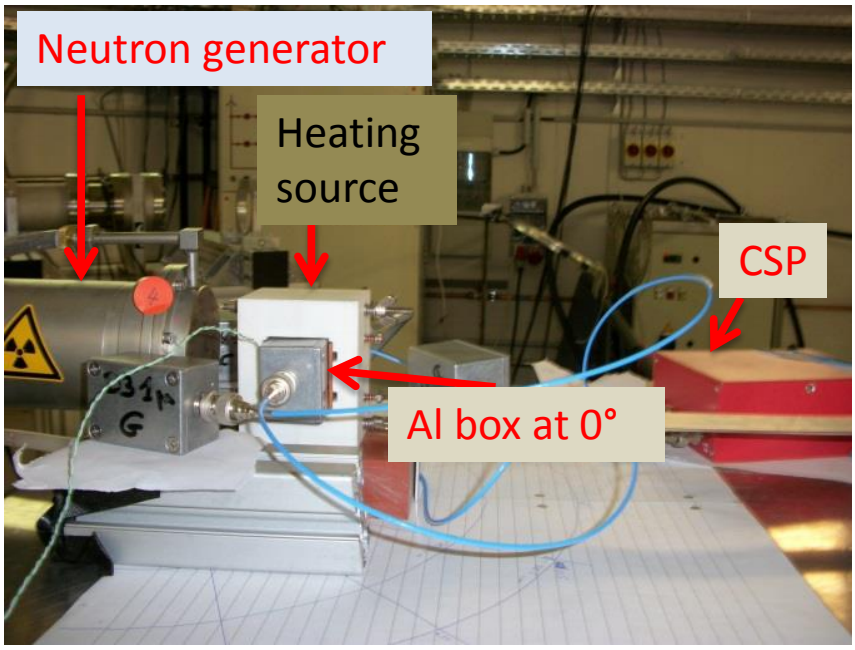

Figure 4.28 Setup used for fast neutron irradiation where each diode is placed inside an Al box and as close as possible to the tritium target of the D-T neutron generator. The CSP is placed close to the detectors.

4.4.1.1 D3-b diodes at different bias voltages

Due to the small area of the used diodes (less than 1 mm^2) the measurement time was in most cases 30 minutes to obtain high counts and thus a more resolvable PHS. In order to detect fast neutrons, they should interact with matter via scattering (elastic or inelastic) or by absorption [108]. All such interactions will contribute to the final PHS. The PHS from D3-b diodes at different bias voltages and temperatures are shown in figure 4.29. Such pulse height response is typical for fast neutrons with SiC [45] [109]. The expected nuclear reactions and the threshold energies are listed in table 4.1. Referring to this table many features of the measured pulse height spectra could be explained. The major part of the spectra is due to scattering because of the high cross section relative to the other possible interactions. Thus the continua for ^{28}Si and ^{12}C elastic and inelastic scattering dominate the detector response at the low energy portion of the PHS as presented in figure 4.29.

A noticeably well-defined peak is obtained which is generally related to the $^{12}C(n,\alpha)^{9}Be$ reaction. This peak is seen around channel 2500 that would correspond to about 8.3 MeV if a 14 MeV neutron source is used [109]. At higher energies several peaks related to $^{28}Si(n,\alpha)^{25}Mg$ are not well resolved because of the limited

thickness of the active volume of the detector (less than 20 μm). Peaks related to $^{12}C(n,p)$ and $^{28}Si(n,p)$ are absent in the PHS. This can be explained by the long range of protons over 400 μm in SiC as illustrated in figure 4.31. In this case most of the proton energy is deposited beyond the active region of the detector.

Table 4.1 Fast neutron induced reactions in silicon carbide

Reaction	**Q Value (MeV)**	**Energy Threshold (MeV)**
$^{12}C(n,n')^{12}C$ ground state	0	0
$^{12}C(n,n')^{12}C$ 2+	-4.4389	4.8088
$^{12}C(n,\alpha)^{9}Be$	-5.7012	6.4196
$^{12}C(n,n')3\alpha$	-7.3666	8.4286
$^{12}C(n,p)^{12}B$	-12.5856	13.7401
$^{28}Si(n,n')^{28}Si$ ground state	0	0
$^{28}Si(n,n')^{28}Si$ 2+	-1.7790	1.8425
$^{28}Si(n,\alpha)^{25}Mg$	-2.6537	2.7653
$^{28}Si(n,p)^{28}Al$	-3.8599	4.0042

It can be noticed from figures 4.29 and 4.30 that the counting rate increases with the applied reverse bias voltage. Peaks become more visible beyond the channel 2500 with the increased bias voltage. This is due to an increase in the thickness of the SCR from 12 μm to ~17 μm (see figure 4.15) leading to more charge deposition mainly due to the $^{28}Si(n,\alpha)^{25}Mg$ reaction. Thus increasing the SCR thickness results in more charge collection (see figure 4.30) which is in a good agreement with Monte Carlo N-Particle simulations in [110].

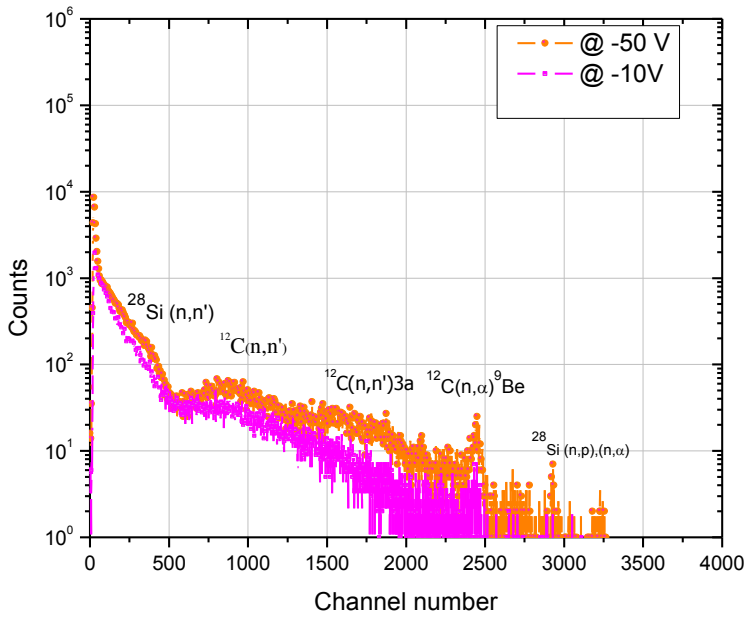

Figure 4.29 PHS of a D3-b diode at different reverse bias voltages. This diode was placed at 90° to the tritium source (30 min measuring time)

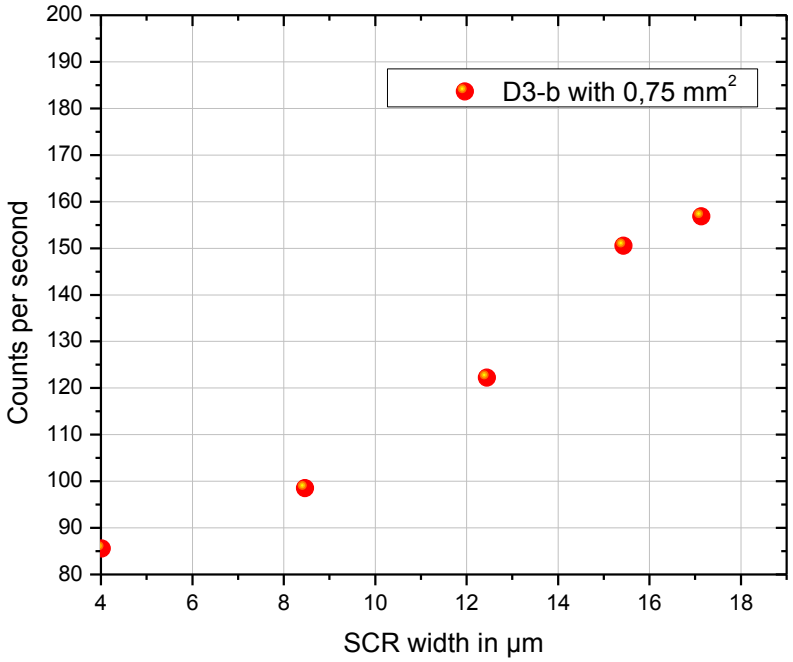

Figure 4.30 Count rates in the D3-b diode as a function of the thickness of the SCR

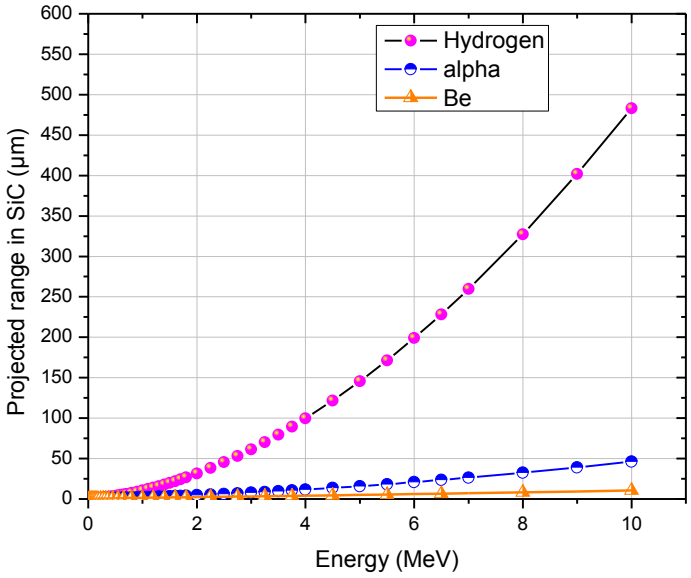

Figure 4.31 Projected range of protons, alphas and Be ions as they enter SiC with different energies

4.4.1.2 D3-b diodes at different temperatures

Measuring the diodes at different temperatures up to 150 °C leads to pulse height spectra all with the same features as illustrated in figure 4.32. This is to be expected as SiC is a wide band semiconductor with high thermal conductivity as mentioned in chapter 1. The position of the $^{12}C(n,\alpha)^{9}Be$ peak shifts by less than 0.04 MeV with temperature change [111]. This is because the energy band gap of SiC decreases by only 0.03 eV with a temperature change from room temperature to 150°C as calculated by the formulation of Varshni [112]:

$$E_g\ (T) = E_g(0) - \frac{\alpha T^2}{T + \beta} \tag{4.7}$$

where $E_g(0)$ and $E_g(T)$ are respectively the energy gap at 0 K and at a given temperature. α and β are material constants, for 4H-SiC their values are 6.5×10^{-4} eV/K and 1300 K respectively.

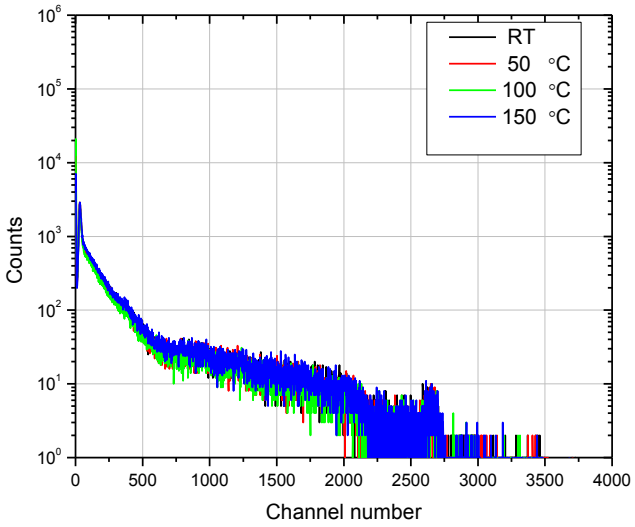

Figure 4.32 Stability of the PHS of a D3-b diode at -40V at different temperatures such a diode is placed in the forward direction to the tritium source (30 min measuring time)

4.4.1.3 D3-b diodes at different energies

The D3-b diodes are sensitive to the change in the neutron energy. Thus an increase of neutron energy by 0.6 MeV from 14.12 MeV at 90° to 14.70 MeV at 0° is seen in the PHS by the shift of the $^{12}C(n,\alpha)^{9}Be$ related peak by 212 channels (see figure 4.33), which would correspond to an equivalent increase in energy deposition [111]. As the incident neutron energy increases, more energy is imparted to the ^{12}C leading to more energy deposition by the reaction products $^{12}C(n,\alpha)^{9}Be$.

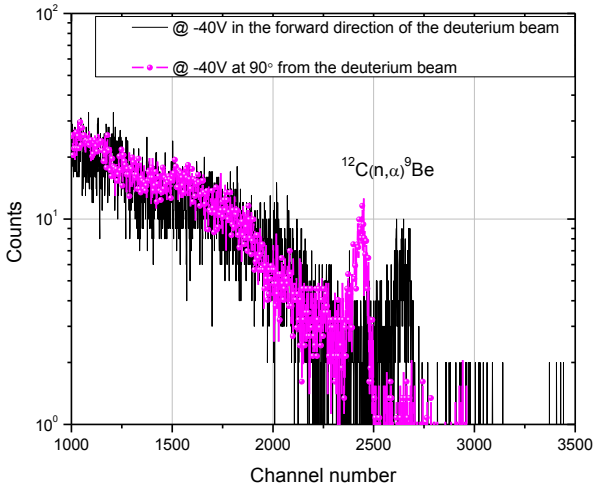

Figure 4.33 PHS of a D3-b diode at -40V at two different positions relative to the tritium source (30 min measuring time)

4.4.1.4 D1 and D2 diodes at different bias voltages

In addition to the D3-b diodes tested under fast neutrons, the D1 diodes have been irradiated under the same conditions (14.12 MeV). The PHS of such diodes at different bias voltages are presented in figure 4.34. As illustrated, increasing the bias voltage results in a slightly higher counting rate. This slight increase could be attributed to the very thin SCR of about 5 µm even at -75 V which leads to few structured features compared to the typical fast neutron spectra shown previously. A more structured PHS would require a further increase in the bias voltage to reach the 15 µm n-epitaxial layer.

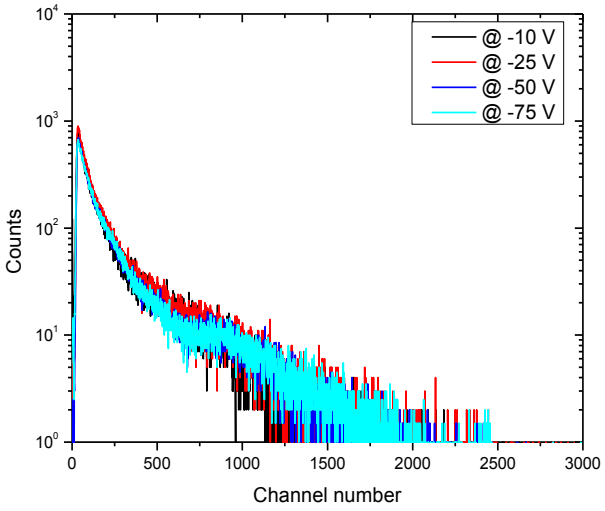

Figure 4.34 PHS of a D1 diode at different reverse bias voltages .Such a diode is placed at 90° to the axis of the tritium source (measuring time 1000 s)

However the D2-diodes realized by plasma or standard ion implantation show a different PHS under fast neutron irradiation. For comparison, the PHS of D2-diodes and D3-b diodes irradiated under the same conditions have been plotted on the same scale as illustrated in figures 4.35 and 4.36. The PHS of D3-b diodes irradiated for 300 s show more counts at higher channels compared to D2 diodes even though the latter have been irradiated for a longer time.

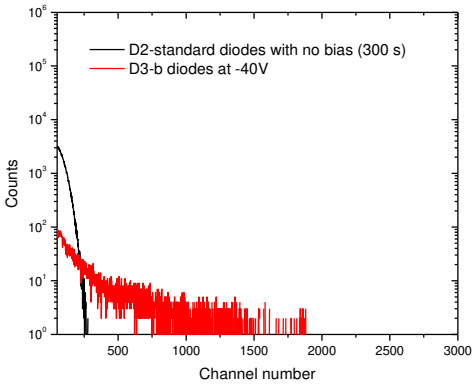

Figure 4.35 Non-typical response from D2-standard diodes irradiated under fast neutrons

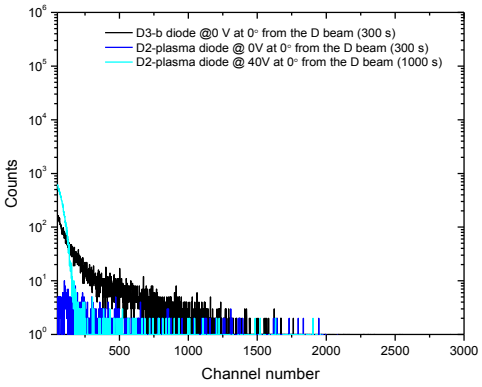

Figure 4.36 Non-typical response from D2-plasma diodes irradiated under fast neutrons

4.4.2 Low fast neutron flux

Besides irradiation in the BR1 nuclear reactor under thermal neutrons, the D3 diodes have been also irradiated under fast neutrons using the facilities at Schlumberger. The neutron source at Schlumberger's facility is a 14 MeV pulse source with a flux of about 10^8n/s over 4π steradian. The pulse duration is 10 seconds, and it is repeated every 100 μs. Inside a stainless steel tube the neutron source is placed into a water tank which acts as a moderator as illustrated in the figure 4.37. The thickness of the stainless steel wall is about 3 mm. An empty pipe goes through the whole central column to give access to the core of the set-up where the detector is placed.

Each diode was placed inside an Al box which in turn was placed inside the tank. Using a lemo cable 3 m long the diode was connected to a CAEN charge sensitive preamplifier A1422. The output of the CSP is fed into CAEN desktop digitizer (DT5780) which serves as a MCA. The diode was placed as close as possible (2 cm) to the neutron source. Thus it receives both fast neutrons emitted directly by the source and the moderated neutrons by the water surrounding the source. Due to the geometrical configuration of the diode and source the expected flux of fast neutrons hitting the box is 1.85 $\times 10^5$ n/cm^2·s and 1.75 $\times 10^4$ n/cm^2·s for the thermal neutrons. The gamma component is expected to be negligible[113].

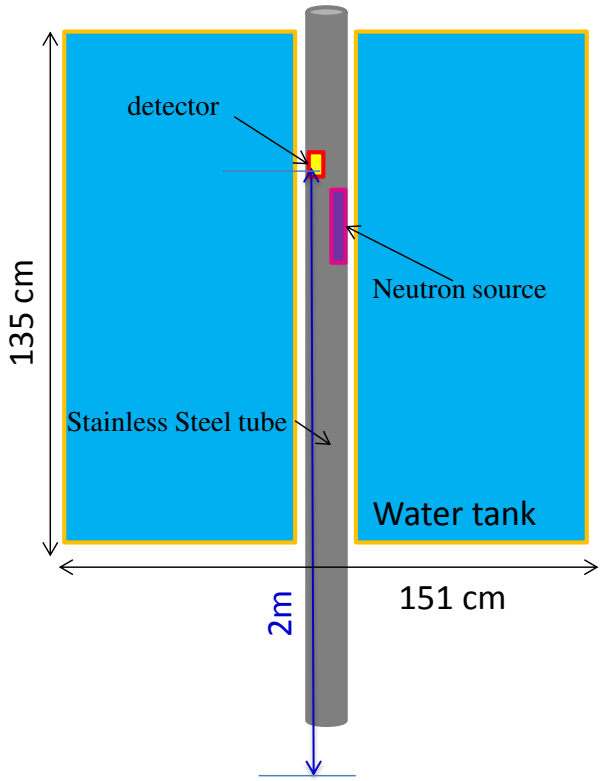

Figure 4.37 The setup used for fast neutron irradiation. The detector is placed as close as possible to the neutron source. The acquisition system is about 2m from the detector.

4.4.2.1 D3-diodes at different bias voltages and temperatures

The D3-b diode with ^{10}B-based NCL has been irradiated using this setup. The PHS of such a diode is shown in figure 4.38. Although the measuring time is 1 hour the count rate is still low (~1 cps), this can be due to both the small area of the used diode (0.78 mm^2) and the low neutron fluxes hitting the detector itself. However, the PHS of D3-a diodes with larger areas (25 mm^2) show a count rate of ~10 cps during 30 min of measurement. D3-a diodes (25 mm^2) with and without ^{10}B have been tested revealing the same PHS indicating no effect of the ^{10}B-based NCL (see figure 4.39). This could be due to the low thermal neutron flux seen by the detector.

Moreover such diodes have been irradiated at different temperatures showing the same PHS at room temperature and at 106 °C, reflecting their stability at high temperatures as illustrated in figure 4.40. Increasing the bias voltage from -3 V to -45 V produces a higher counting rate as indicated in figure 4.41 due to the increase in the detector active volume. It is worth noting that the features of the PHS are not

well defined as were those irradiated using the D-T generator with higher flux. This is of course attributed to the low neutron fluxes used in the present case requiring much longer measuring time.

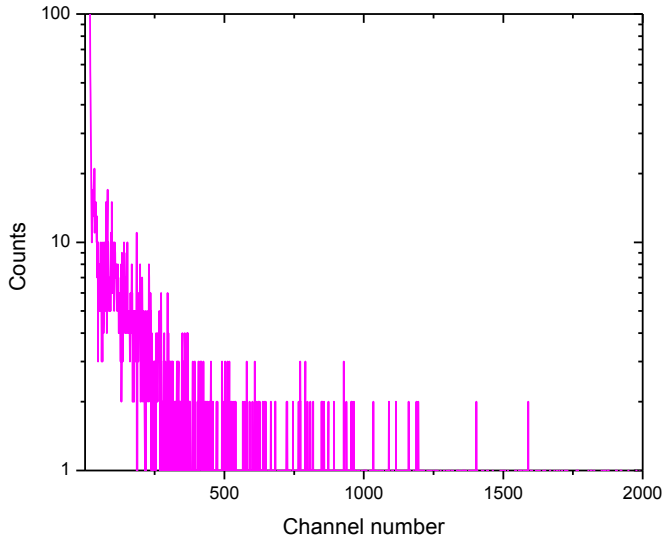

Figure 4.38 PHS of the D3-b diode (0.78 mm^2) at -40V for 1hour measurement

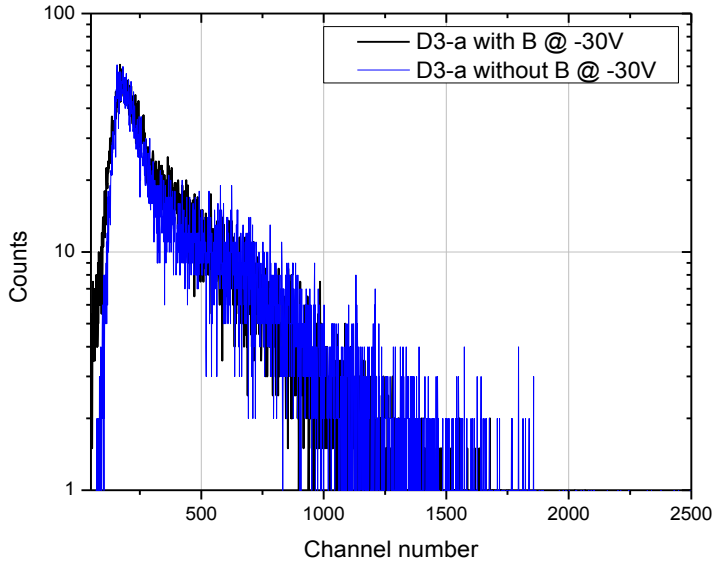

Figure 4.39 PHS of D3-a diodes with and without B at -30V for 30 min measuring time

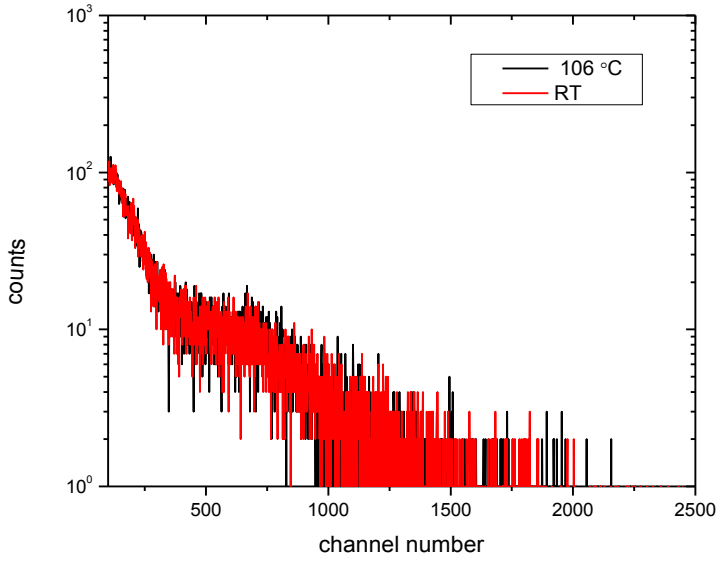

Figure 4.40 PHS of the D3-a diodes without B at -30 V at RT and 106°C for 30 min measuring time

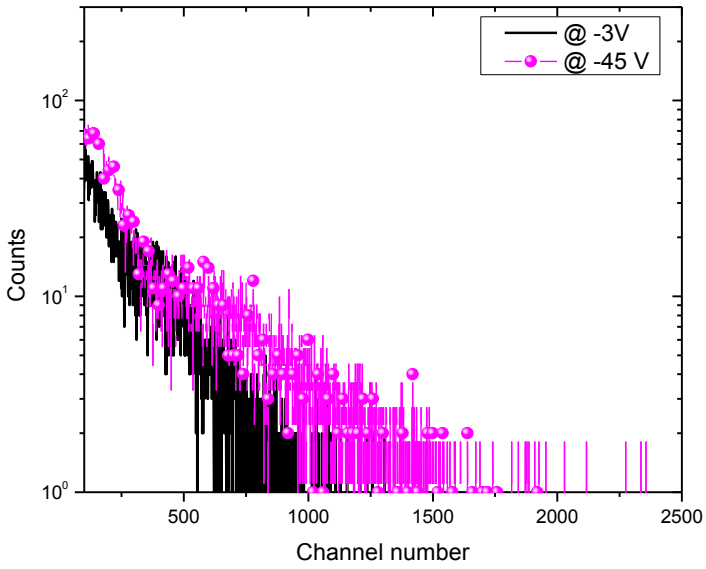

Figure 4.41 PHS of D3-a without B at different bias voltages. The measuring time is 30 min

4.5 Gamma ray response measurements

To examine the response of our detectors under gamma rays, an irradiation was carried out using the Linac Mini-Linatron source of the French Atomic Energy Commission (CEA) in Cadarache. This source is a bremsstrahlung source with a linear electron accelerator. The electron beam generates bremsstrahlung and a fraction of photoneutrons as it hits a tungsten target. The neutron fluxes (2.05×10^5 n/cm^2s) are low compared with the photon fluxes (2.13×10^9 photons/cm^2s). Only the D3-a diodes were tested in the Mini-Linatron facility.

Measurements were performed under different bias voltages, with different types of shielding, and with varying the distance from the source. Since the Mini-Linatron operates in pulse mode (300 Hz repetition frequency, 3.8 μs pulse width), the instantaneous photon flux during the pulses was extremely high. Therefore, no single event in the detector was resolvable; the pulse height spectrum represents the total energy deposited per Mini-Linatron pulse in the SCR of the detector.

As shown in figure 4.42, the integrated deposited energy decreases as the distance between the detector and the source increases from 8 to 14 cm. A slight shift of the peaks to a higher channel number is detected as the voltage increases from 0 to -200 V. This is because more charges are collected in the SCR of the diode.

Since low-energy photons make up most of the photon flux, a few centimeters of polyethylene (PE) and (Cd) cadmium not only provides an efficient neutron shielding, but also reduces considerably the low-energy photon flux near the detector, which explains the shift of the peak to lower channel number as shown in figure 4.43. Thanks to its high density and high atomic number, lead (Pb) is effective in stopping gamma rays. This explains the considerable decrease of the channel number when lead is used, as shown in figure 4.43 where low photon fluxes reached the sensitive region of the detector.

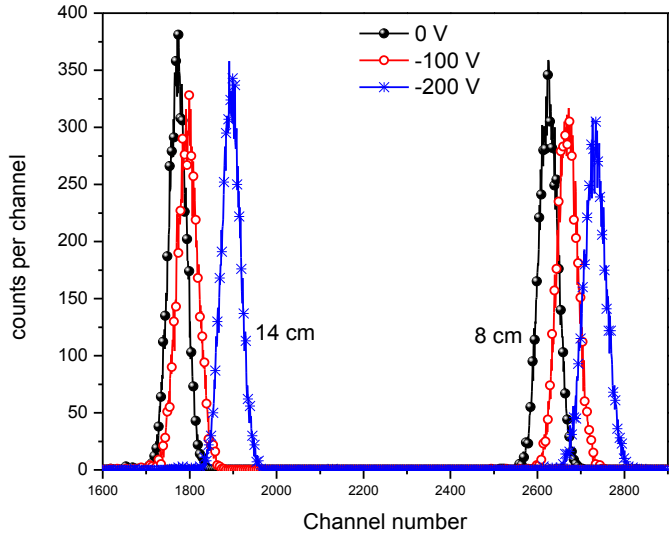

Figure 4.42 Pulse height spectra of D3-a diode with boron at different distances from the Linac source (8 and 14 cm) and at different reverse biases (0, -100 and -200 V)

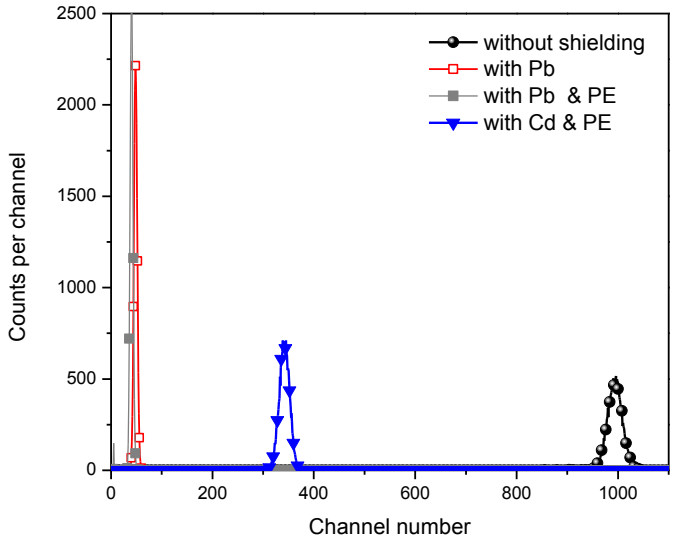

Figure 4.43 Pulse height spectra of the 25 mm^2 D3-a diode with boron using different types of shielding and at -100 Vbias

4.6 Stability of the detectors under irradiation

In order for the radiation to be detected the electron-hole pairs produced by such irradiation should be free to move in the detector to reach the electrodes. If the detector contains traps produced by impurities or by the irradiation itself, the electrons may be captured before reaching the electrode which will reduce the pulse height. Generally a deep level transient spectroscopy (DLTS) measurement is performed to obtain a detailed description about the defect formation type and its cross section. Such measurements that have been performed in this work in the temperature range 30 to 320 K do not show any new peaks related to defects caused by irradiation. However, as a first estimation, the electrical characteristics such as current voltage measurement can be used to have an idea about the detector stability under irradiation.

After they have been irradiated under thermal neutrons (7×10^{8} n/cm^{2}s for about 16 hours, leading to an accumulated thermal neutron fluence of 4×10^{13} n/cm^2), the current densities of the D1 diodes have been measured as shown in figure 4.44. Although the D1-diodes show low leakage current before irradiations, they prove to be less stable against thermal neutron irradiation than the D3-diodes. This is seen by the increase in the leakage current after the thermal neutron irradiation as illustrated in the figure below.

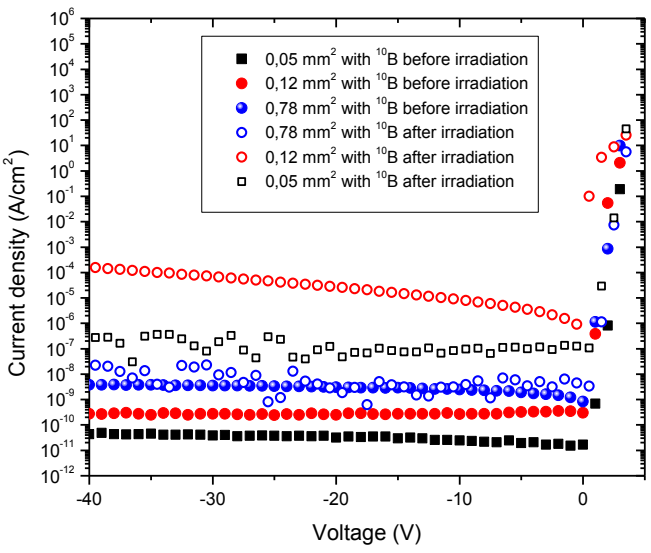

Figure 4.44. Current density of the D1 diodes before and after thermal neutron irradiation

The D3-a and D3-b diodes show the same electrical behavior before and after irradiations, proving a good stability against high irradiation as illustrated in figures 4.45 and 4.46 respectively.

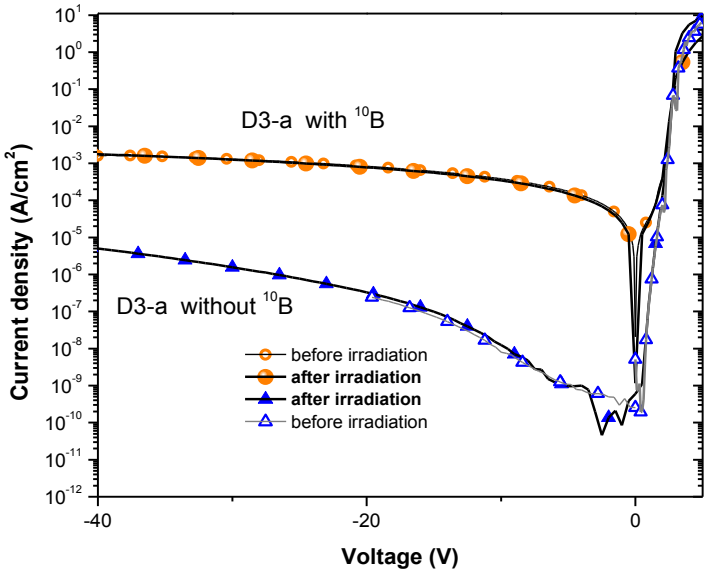

Figure 4.45 Current density of the 25 mm^2 D3-a diodes with and without ^{10}B before and after thermal neutron irradiation

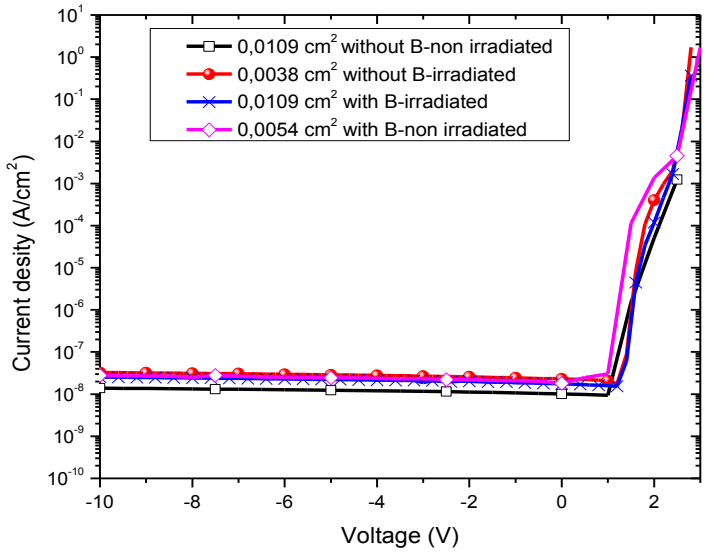

Figure 4.46 Current density of the D3-b diodes with different areas with and without ^{10}B before and after thermal neutron irradiation

To prove the reproducibility of the PHS of the diodes with time, several measurements have been repeated under the same conditions. Figures 4.47 and 4.48 show the pulse height spectra of D3-a and D3-b diode tested at a given bias voltages respectively. As shown in these figures, the pulse height spectra for both types of detectors are the same even after irradiating for a longer time. This behavior demonstrates the stability of such type of detectors under thermal neutron irradiation. Therefore irradiating for a longer time doesn't degrade the PHS characteristics in these cases.

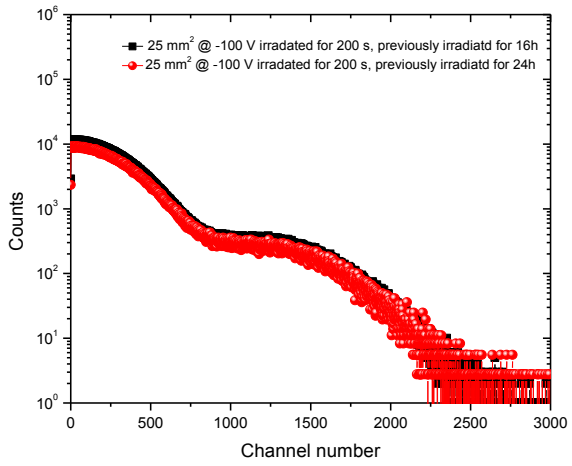

Figure 4.47. Thermal neutron detection spectra measured with D3a-diodes with ^{10}B-based NCL at -100 V previously irradiated for 16h (~4×10^{13} n/cm^2) and 24 h

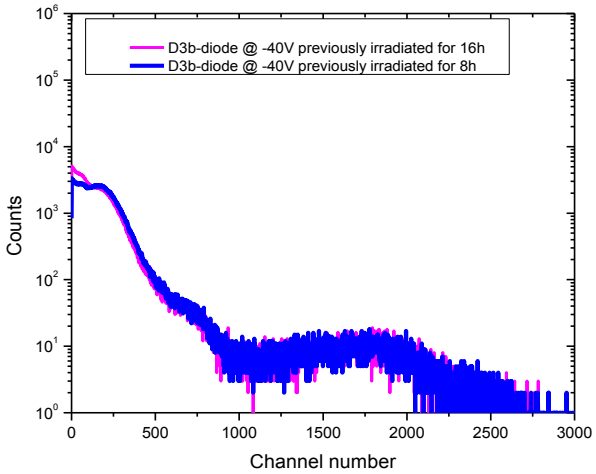

Figure 4.48. Thermal neutron detection spectra measured with D3b-diodes with ^{10}B-based NCL at -40 V previously irradiated for 8h (~ 2×10^{13} n/cm^2) or for 16h (~4×10^{13} n/cm^2)

4.7 Conclusions

So far we have presented the response of the realized diodes under different types of irradiations. Regardless of the method used to realize radiation detectors, the produced detector, should have a low leakage current to improve the signal-to-noise ratio. The area of the diode also plays an important role especially if low irradiation fluxes are present. Since in most cases the leakage current increases with the surface area of the diode, one must find a compromise between the area and the leakage current of the diode. As we have seen so far that the electronics used also affect the output response of a detector. In addition, the thickness of the space charge region is also an important parameter to be taken into consideration while realizing a detector. For instance, the SCR of the D1 diodes was thin enough (at -75 V) to be dedicated for fast neutron detection.

If a detector is dedicated for low flux environments, the efficiency of the detector should be enhanced either by increasing the area of the diode or the implanted boron concentration, or even by adding a converter layer. In our case we added a layer of boron to enhance the thermal neutron detection. However a hydrogen-rich layer can be added to enhance the fast neutron detection in the case of low fast neutron flux.

If we compare different realized diodes it is evident that diodes with high leakage current density (D3-a and the D2-diodes) show pulse height spectra with non-well characterized features. For example as we have seen for the D2-diodes irradiated under fast neutrons or the D3-a diodes under thermal neutrons. On the other hand the largest D1 diodes detect thermal neutrons even without any external bias voltage. It is worth noting that the smallest D1-diodes require a longer accumulation time to produce more readable spectra.

Discrimination between gammas and neutrons was feasible in one single detector (especially D3-b and D1 diodes). This is possible by the separation of the gamma contribution in the low energy part of the spectrum from the neutron contribution in the higher part.

Conclusions & future work

As a part of the European project (I_SMART) the main objective of this work was to demonstrate the reliability of new methods of realizing semiconductor radiation detectors. Such detectors are intended to be used in harsh environments where high temperature and high radiation fluxes exist. In such environments wide band gap semiconductors should be used. With its high thermal conductivity and high radiation resistance SiC is one of the best candidates for use in harsh environments.

Several methods have been applied to produce our SiC-based radiation detectors. The first method (D1) is based on aluminum ion implantation to create the p+ layer followed by an annealing step to activate the dopant. Then ^{10}B ion implantation has been performed to create the neutron converter layer (NCL). The second method creates the NCL and the p+ layer in one single process. This is attained by ion implantation of ^{10}B into SiC either by standard ion implantation (D2-standard) or by plasma immersion ion implantation (D2-plasma). The third method is based on ion implantation of ^{10}B into the aluminum metallic contact for converting thermal neutrons to detectable charged energetic ions. It should be mentioned that ^{10}B implantation at high temperature into Al metallic contact (D3-a) results in a significant diffusion of ^{10}B beyond the metallic contact as was demonstrated by SIMS measurement. Consequently ^{10}B implantation into Al should be performed at room temperature (D3-b) which results in the same electrical behavior before and after implantation. The fourth method is based on sputtering a layer of boron on top of a p-n junction (D4). However, such a layer was far (~6 μm) from the space charge region (SCR) of the detector resulting in a negligible thermal neutron detection.

We used SRIM simulations to choose the proper NCL thickness and position with respect to the active volume of the detector in order to have high ionization rate. This is an important issue since the mechanisms for thermal neutron detection rely on low energy charged particle detection (alpha and lithium) which have to reach the

active volume of the detector. Choosing a NCL thickness greater than the range of these charged particles results in a low neutron detection efficiency.

The electrical characteristics (current-voltage measurements) of the diodes with and without ^{10}B were performed before irradiation in order to select those with the lowest leakage current density. This current density should be as low as possible in order to reduce the noise contribution in the overall signal. The area of the used diode should be well adapted to the application. In other words the larger diodes can serve best in low radiation environments while smaller ones serve best in a high radiation flux.

The realized detectors have been irradiated under thermal neutrons, fast neutrons and under gamma rays. Using the well-chosen electronics, the diodes with and without ^{10}B were irradiated under thermal neutrons using the BR1 nuclear reactor. The diodes with ^{10}B detect thermal neutrons by showing an additional spectral component at high channel number (only seen in diodes with ^{10}B). Such component disappears when the reactor power is reduced to zero. A linear count rate was obtained versus the reactor power. Furthermore discrimination between neutrons and gammas is possible where gammas deposit their energy in the low energy part of the pulse height spectrum while neutrons contribute to the high energy spectra. Thus it is possible in one single diode to obtain separately information on the gamma and neutron fluxes. This is important when such detectors are dedicated to environments where both gammas and neutrons exist simultaneously.

The diodes with high leakage current density (especially D2-diodes) show high noise level during measurements. Although the features of their pulse height spectra resemble those of low leakage current density, their response was not affected by the different applied reverse bias voltages and was not faithfully reproducible.

Besides thermal neutron irradiations, the diodes have been irradiated under fast neutrons (D-T neutron generator) with different fluxes and different temperatures. The D3-b diodes irradiated for 1 hour with 14 MeV neutrons and at about $\sim 10^5$ $n/cm^2 \cdot s$, do not yield well-defined PHS. However irradiating the same diode for 30 minutes under higher fluxes ($\sim 10^{10}$ $n/cm^2 \cdot s$) reveal a well-characterized PHS showing a well-defined peak related to $^{12}C(n,\alpha)^9Be$ reaction. Such diodes were stable under

different temperatures up to 155 °C. Further increase in the temperature up to 500 °C is currently underway.

To enhance the sensitivity of the detector to fast neutrons hydrogen could be implanted into the SiC diodes. Then well-defined peaks for high energy protons, would require that the SCR be thick enough to collect most of the deposited energy. This could be achieved by using diodes with thick n-epitaxial layer (~100 μm).

After irradiation under thermal neutrons the electrical characterization of the irradiated diodes was measured and compared to those before irradiation. It was noticed that the D3-diodes show the same electrical behavior before and after irradiation. Moreover the PHS were reproducible even after irradiating for a long time (16 h which corresponds to an accumulation of ~4×10^{13} n/cm^2). However for the D1-diodes the electrical characterizations were not exactly reproducible. This will require further study of the radiation effects. Using deep level transient spectroscopy (DLTS) we have started to study the effects of different irradiations on defect formation in SiC in the temperature range 30 to 320 K. However for more detailed information higher temperatures will be essential. Such measurements are important as they could give an idea about the expected lifetime of the detectors.

Our realized detectors were based on boron ion implantation for thermal neutron detection but implantation or deposition of a layer of ^{6}Li could also be a solution for making thermal neutron detectors. Since ^{6}Li possesses a lower cross section for neutron capture than ^{10}B, such diodes could be suitable for environments where high neutron fluxes exist. To increase even more the thermal neutron detection efficiency, diodes could be implanted by ^{10}B to create the p+ layer followed by ^{6}Li to realize the NCL. Whatever the method followed to fabricate a radiation detector, it should detect the required radiations and discriminate them from background to avoid false data interpretation.

In conclusion, the results of this work should encourage a continuity of the current European project where pixel detectors could be used. Such a segmented or pixel-like detector design enhances the spectroscopic functionality of the whole detection system. For example, different pixel detector units could be manufactured on a single SiC wafer for simultaneous monitoring of fast and thermal neutrons as well as spectroscopy of gamma radiation. For fast neutron detection a hydrogen-rich layer

could be used, while for slow neutron detection a layer of ^{10}B or ^{6}Li-enriched converter layer could be added. Also the different detectors could incorporate different widths of space charge region to discriminate among different irradiations.

References

[1] G. E. Knoll, *Radiation Detection and Measurement*, 3rd edn. Wiley, 2000.

[2] A. Lyoussi, *Détection de rayonnements et instrumentation nucléaire*. France: EDP sciences, 2010.

[3] G. Lutz, *Semiconductor radiation detectors*. Munich, 1999.

[4] M. Moll, "Development of radiation hard sensors for very high luminosity colliders—CERN-RD50 project," *Nucl. Instruments Methods Phys. Res. Sect. A Accel. Spectrometers, Detect. Assoc. Equip.*, vol. 511, no. 1–2, pp. 97–105, Sep. 2003.

[5] J. Grant, W. Cunningham, A. Blue, V. O'Shea, J. Vaitkus, E. Gaubas, and M. Rahman, "Wide bandgap semiconductor detectors for harsh radiation environments," *Nucl. Instruments Methods Phys. Res. Sect. A Accel. Spectrometers, Detect. Assoc. Equip.*, vol. 546, no. 1–2, pp. 213–217, Jul. 2005.

[6] P. J. Sellin and J. Vaitkus, "New materials for radiation hard semiconductor dectectors," *Nucl. Instruments Methods Phys. Res. Sect. A Accel. Spectrometers, Detect. Assoc. Equip.*, vol. 557, no. 2, pp. 479–489, Feb. 2006.

[7] L. M. Tolbert, B. Ozpineci, S. K. Islam, and M. S. Chinthavali, "Wide bandgap semiconductors for utility applications," *semiconductors*, vol. 1, p. 3, 2003.

[8] M. Siad, A. Keffous, Y. Belkacem, H. Menari, S. Mamma, and C. Lakhdar Chaouch, "Degradation of electrical properties of silicon detectors under 3MeV proton irradiation," *Nucl. Instruments Methods Phys. Res. Sect. A Accel. Spectrometers, Detect. Assoc. Equip.*, vol. 512, no. 1–2, pp. 106–110, Oct. 2003.

[9] M. Cooke, "Semiconductor hardnut," *III-Vs Rev.*, vol. 18, no. 9, pp. 40–44, 2006.

[10] G. Lucas and L. Pizzagalli, "Comparison of threshold displacement energies in β-SiC determined by classical potentials and ab initio calculations," *Nucl. Instruments Methods Phys. Res. Sect. B Beam Interact. with Mater. Atoms*, vol. 229, no. 3–4, pp. 359–366, Apr. 2005.

[11] F. Nava, G. Bertuccio, A. Cavallini, and E. Vittone, “Silicon carbide and its use as a radiation detector material,” *Meas. Sci. Technol.*, vol. 19, no. 10, p. 102001, Oct. 2008.

[12] J. A. Dueñas, J. de la Torre Pérez, A. Martín Sánchez, and I. Martel, “Diamond detector for alpha-particle spectrometry.,” *Appl. Radiat. Isot.*, vol. 90C, pp. 177–180, Apr. 2014.

[13] V. Grilj, N. Skukan, M. Jakšić, W. Kada, and T. Kamiya, “Irradiation of thin diamond detectors and radiation hardness tests using MeV protons,” *Nucl. Instruments Methods Phys. Res. Sect. B Beam Interact. with Mater. Atoms*, vol. 306, pp. 191–194, Jul. 2013.

[14] M. Willander, M. Friesel, Q. Wahab, and B. Straumal, “Silicon carbide and diamond for high temperature device applications,” *J. Mater. Sci. Mater. Electron.*, vol. 17, no. 1, pp. 1–25, Jan. 2006.

[15] G. Bertuccio, “Silicon Carbide Radiation Micro-Detectors for Harsh Environments,” *SPIE Defense, Secur. Sens.*, 2010.

[16] S. Saddow and A. Agarwal, *Advances in silicon carbide processing and applications*. Boston, 2004.

[17] J. J. Berzelius, “Unterfuchungen Uber die Flufsfpathfaure und deren Merkwurdigften Verbindungen,” *Ann. Phys., Lpz*, vol. 1, p. 169, 1824.

[18] E. Acheson, M. City, and I. Assicnoe, “production of artificial crystalline carbonaceous materials,” No,492767,1893.

[19] H. Moissan, “Etude du silicure de carbone de la météorite de canon Diablo,” *C.R Acad. Sci Paris*, vol. 140, pp. 405–406, 1905.

[20] J. A. Lely, “Darstellung von Einkristallen vonSilizium Karbid und Beherrschung von Art und Menge der Eingebauten Verunreingungen,” *Ber. Deut. Keram*, vol. 32, pp. 229–236, 1955.

[21] Y. M. Tairov and V. F. Tsvetkov, “Invetsigation of growth processes of ingots of silicon carbide single crystal,” *J. Cryst. Growth*, vol. 43, no. 2, pp. 209–212, 1978.

[22] S. G. Muller and J. , R.C. Glass, H.M. Hobgood, V.F. Tsvetkov, M. Brady, D. Henshall, D. Malta, R. Singh, J. Palmour, C.H. Carter, “Progress in the industrial production of SiC substrates for semiconductor devices,” *Mater. Sci. Eng. B*, vol. 80, pp. 327–331, 2001.

[23] J. C.H. Carter, V. F. Tsvetkov, R. C. Glass, D. Henshall, M. Brady, S. G. Muller, O. Kordina, K. Irvine, J. A. Edmond, H.-S. Kong, R. Singh, S. T. Allen, and J. W. Palmour, “Progress in SiC: from material growth to

commercial device development," *Mater. Sci. Eng. B*, vol. 62, pp. 1–8, 1999.

[24] S. G. Müller, E. Sanchez, D. Hansen, R. D. Drachev, G. Chung, B. Thomas, J. Zhang, M. J. Loboda, M. Dudley, H. Wang, F. Wu, S. Byrappa, B. Raghothamachar, and G. Choi, "Volume production of high quality SiC substrates and epitaxial layers: Defect trends and device applications," *J. Cryst. Growth*, vol. 352, no. 1, pp. 39–42, Aug. 2012.

[25] R. D.Evans, *The atomic nucleus*. New York, 1955.

[26] J. E. Turner, *Atoms, Radiation, and Radiation Protection*, 3rd edn. Wiley, 2007.

[27] "Nuclear Data Viewer http://t2.lanl.gov/nis/data.shtml." .

[28] R. Babcock, S. Ruby, F. Schupp, and K. Sun, "Miniature Neutron Detectors," *Electr. Corp. Mater. Eng. Rep. No. 5711-6600-A*, 1957.

[29] V. Tikhomirova, O. Fedoseeva, and G. Kholuyanov, "Properties of Ionizing-Radiation Counters Made of Silicon Carbide Doped by Diffusion of Beryllium," *Sov. Phys. -Semiconductors*, vol. 6, no. 5, 1972.

[30] F. H. Ruddy, A. R. Dulloo, J. G. Seidel, S. Seshadri, and L. B. Rowland, "Development of a silicon carbide radiation detector," *IEEE Trans. Nucl. Sci.*, vol. 45, no. 3, pp. 536–541, Jun. 1998.

[31] F. Nava, P. Vanni, C. Lanzieri, and C. Canali, "Epitaxial silicon carbide charge particle detectors," *Nucl. Instruments Methods Phys. Res. Sect. A Accel. Spectrometers, Detect. Assoc. Equip.*, vol. 437, no. 2–3, pp. 354–358, Nov. 1999.

[32] E. V Kalinina, A. M. Ivanov, and N. B. Strokan, "Performance of pn 4H-SiC film nuclear radiation detectors for operation at elevated temperatures (375° C)," *Tech. Phys. Lett.*, vol. 34, no. 3, pp. 210–212, 2008.

[33] E. V Kalinina, A. M. Ivanov, N. B. Strokan, and A. A. Lebedev, "Structure and characteristics of the high-temperature SiC detectors based on Al ion-implanted p + –n junctions," *Semicond. Sci. Technol.*, vol. 26, no. 4, p. 045001, Apr. 2011.

[34] A. M. Ivanov, N. B. Strokan, and A. A. Lebedev, "Effect of elevated temperatures (up to 250°C) on the operating capacity of heavily irradiated p+–n SiC detectors," *Nucl. Instruments Methods Phys. Res. Sect. A Accel. Spectrometers, Detect. Assoc. Equip.*, vol. 597, no. 2–3, pp. 203–206, Dec. 2008.

[35] G. Bertuccio, R. Casiraghi, A. Cetronio, C. Lanzieri, and F. Nava, "A new generation of X-ray detectors based on silicon carbide," *Nucl. Instruments*

Methods Phys. Res. Sect. A Accel. Spectrometers, Detect. Assoc. Equip., vol. 518, no. 1–2, pp. 433–435, Feb. 2004.

[36] G. Bertuccio, R. Casiraghi, A. Cetronio, C. Lanzieri, and F. Nava, "Silicon carbide for high resolution X-ray detectors operating up to 100°C," *Nucl. Instruments Methods Phys. Res. Sect. A Accel. Spectrometers, Detect. Assoc. Equip.*, vol. 522, no. 3, pp. 413–419, Apr. 2004.

[37] F. Moscatelli, "Silicon carbide for UV, alpha, beta and X-ray detectors: Results and perspectives," *Nucl. Instruments Methods Phys. Res. Sect. A Accel. Spectrometers, Detect. Assoc. Equip.*, vol. 583, no. 1, pp. 157–161, Dec. 2007.

[38] F. H. Ruddy and J. G. Seidel, "The effects of intense gamma-irradiation on the alpha-particle response of silicon carbide semiconductor radiation detectors," *Nucl. Instruments Methods Phys. Res. Sect. B Beam Interact. with Mater. Atoms*, vol. 263, no. 1, pp. 163–168, Oct. 2007.

[39] F. H. Ruddy and J. G. Siedel, "Effects of Gamma Irradiation on Silicon Carbide Semiconductor Radiation Detectors," in *Nuclear Science Symposium Conference Record, 2006. IEEE*, 2006, vol. 1, pp. 583–587.

[40] A. Kinoshita, M. Iwami, K. Kobayashi, I. Nakano, R. Tanaka, T. Kamiya, A. Ohi, T. Ohshima, and Y. Fukushima, "Radiation effect on pn-SiC diode as a detector," *Nucl. Instruments Methods Phys. Res. Sect. A Accel. Spectrometers, Detect. Assoc. Equip.*, vol. 541, no. 1–2, pp. 213–220, Apr. 2005.

[41] J. L. Jones, B. W. Blackburn, F. H. Ruddy, J. G. Seidel, and R. W. Flammang, "Novel Silicon Carbide Detector for Active Inspections," *Pulse*, 2007.

[42] M. Heibel, M. Walter, and R. Flammang, "Solid state radiation detector with enhanced gamma radiation sensitivity," 2013.

[43] R. R. Ferber and G. N. Hamilton, "Silicon Carbide High Temperature Neutron Detectors for Reactor Instrumentation," *Nucl. Appl. Title varies Nucl. Appl., Febr. 1965-June 1969*, vol. 2, 1966.

[44] F. H. Ruddy, J. U. Patel, and J. G. Williams, "Power monitoring in space nuclear reactors using silicon," in *Proceedings of the Space Nuclear Conference*, 2005.

[45] F. H. Ruddy, A. R. Dulloo, J. G. Seidel, M. K. Das, and A. K. Agarwal, "The fast neutron response of 4H silicon carbide semiconductor radiation detectors," *IEEE Trans. Nucl. Sci.*, vol. 53, no. 3, pp. 1666–1670, Jun. 2006.

[46] J. HA, S. KANG, K. H. Soo, and S. PARK, "4H-SiC PIN-type Semiconductor Detector for Fast Neutron Detection," *Prog. Nucl. Sci. Technol.*, vol. 1, pp. 237–239, 2011.

[47] R. W. Flammang, J. G. Seidel, and F. H. Ruddy, "Fast neutron detection with silicon carbide semiconductor radiation detectors," *Nucl. Instruments Methods Phys. Res. Sect. A Accel. Spectrometers, Detect. Assoc. Equip.*, vol. 579, no. 1, pp. 177–179, Aug. 2007.

[48] F. H. Ruddy, A. R. Dulloo, B. Petrović, and J. G. Seidel, "Fast neutron spectrometry using silicon carbide detectors," in *Reactor Dosimetry in the 21st Century - Proceedings of the 11th International Symposium on Reactor Dosimetry*, 2003, vol. 1, pp. 347–355.

[49] J. Wu, Y. Jiang, J. Lei, X. Fan, Y. Chen, M. Li, D. Zou, and B. Liu, "Effect of neutron irradiation on charge collection efficiency in 4H-SiC Schottky diode," *Nucl. Instruments Methods Phys. Res. Sect. A Accel. Spectrometers, Detect. Assoc. Equip.*, vol. 735, pp. 218–222, Jan. 2014.

[50] F. Moscatelli, A. Scorzoni, A. Poggi, M. Bruzzi, S. Sciortino, S. Lagomarsino, G. Wagner, I. Mandic, and R. Nipoti, "Radiation hardness after very high neutron irradiation of minimum ionizing particle detectors based on 4H-SiC p+n junctions," *IEEE Trans. Nucl. Sci.*, vol. 53, no. 3, pp. 1557–1563, Jun. 2006.

[51] F. Moscatelli, A. Scorzoni, A. Poggi, and R. Nipoti, "Annealing effects on leakage current and epilayer doping concentration of p+n junction 4H-SiC diodes after very high neutron irradiation," *Nucl. Instruments Methods Phys. Res. Sect. A Accel. Spectrometers, Detect. Assoc. Equip.*, vol. 583, no. 1, pp. 173–176, Dec. 2007.

[52] A. Dulloo, F. H. Ruddy, J. G. Seidel, J. M. Adams, J. S. Nico, and D. M. Gilliam, "The thermal neutron response of miniature silicon carbide semiconductor detectors," *Nucl. Instruments Methods Phys. Res. Sect. A Accel. Spectrometers, Detect. Assoc. Equip.*, vol. 498, no. 1–3, pp. 415–423, Feb. 2003.

[53] A. R. Dulloo, F. H. Ruddy, J. G. Seidel, J. M. Adams, J. S. Nico, and D. M. Gilliam, "The neutron response of miniature silicon carbide semiconductor detectors," *Nucl. Instruments Methods Phys. Res. Sect. A Accel. Spectrometers, Detect. Assoc. Equip.*, vol. 422, no. 1–3, pp. 47–48, Feb. 1999.

[54] C. Manfredotti, A. Lo Giudice, F. Fasolo, E. Vittone, C. Paolini, F. Fizzotti, A. Zanini, G. Wagner, and C. Lanzieri, "SiC detectors for neutron monitoring," *Nucl. Instruments Methods Phys. Res. Sect. A Accel. Spectrometers, Detect. Assoc. Equip.*, vol. 552, no. 1–2, pp. 131–137, Oct. 2005.

[55] A. R. Dulloo, F. H. Ruddy, J. G. Seidel, C. Davison, T. Flinchbaugh, and T. Daubenspeck, "Simultaneous measurement of neutron and gamma-ray radiation levels from a TRIGA reactor core using silicon carbide semiconductor detectors," *IEEE Trans. Nucl. Sci.*, vol. 46, no. 3, pp. 275–279, Jun. 1999.

[56] J. H. Ha, S. M. Kang, S. H. Park, H. S. Kim, N. H. Lee, and T.-Y. Song, "A self-biased neutron detector based on an SiC semiconductor for a harsh environment.," *Appl. Radiat. Isot.*, vol. 67, no. 7–8, pp. 1204–7, 2009.

[57] J. Ha, S. Kang, S. Park, H. Kim, and Y. Kim, "6H-SiC solid state detector development for a neutron measurement," vol. 355, no. June, pp. 352–355, 2008.

[58] W. J. CHOYKE and L. PATRICK, "Luminescence of Donor-Acceptor Pairs in Cubic SiC," *Phys. Rev. B*, vol. 2, p. 4959, 1970.

[59] M. Ikeda, H. Matsunami, and T. Tanaka, "Site effect on the impurity levels in 4H, 6H, and 15R SiC. M.," *Phys. Rev. B*, vol. 22, pp. 2842–2854, 1980.

[60] S. R. Smith, A. O. Evwaraye, W. C. Mitchel, and M. A. Capano, "Shallow acceptor levels in 4H- and 6H-SiC," *J. Electron. Mater.*, vol. 28, no. 3, pp. 190–195, Mar. 1999.

[61] A. Hallén, R. Nipoti, S. E. Saddow, S. Rao, and B. G. Svensson, "Advances in Selective Doping of SiC Via Ion," in *Advances in silicon carbide processing and applications*, Boston, 2004.

[62] K. Gotz and K. Gartner, *High energy ion beam analysis of solid*. Berlin, 1988.

[63] J. Wong-Leung, M. S. Janson, A. Kuznetsov, B. G. Svensson, M. K. Linnarsson, A. Hallén, C. Jagadish, and D. J. H. Cockayne, "Ion implantation in 4H–SiC," *Nucl. Instruments Methods Phys. Res. Sect. B Beam Interact. with Mater. Atoms*, vol. 266, no. 8, pp. 1367–1372, Apr. 2008.

[64] T. Troffer, M. Schadt, T. Frank, H. Itoh, G. Pensl, J. Heindl, H. P. Strunk, and M. Maier, "Doping of SiC by implantation of boron and aluminum," *Phys. Status Solidi*, vol. 162, no. 1, pp. 277–298, 1997.

[65] M. A. Capano, S. Ryu, M. R. Melloch, J. A. Cooper, and M. R. Buss, "Dopant activation and surface morphology of ion implanted 4H- and 6H-silicon carbide," *J. Electron. Mater.*, vol. 27, no. 4, pp. 370–376, Apr. 1998.

[66] W. Jiang, W. J. Weber, S. Thevuthasan, and D. E. McCready, "Displacement energy measurements for ion-irradiated 6H–SiC," *Nucl.*

Instruments Methods Phys. Res. Sect. B Beam Interact. with Mater. Atoms, vol. 148, no. 1–4, pp. 557–561, Jan. 1999.

[67] W. Jiang, W. J. Weber, S. Thevuthasan, and D. E. McCready, "Damage formation and recovery in C+-irradiated 6H–SiC," *Nucl. Instruments Methods Phys. Res. Sect. B Beam Interact. with Mater. Atoms*, vol. 148, no. 1–4, pp. 562–566, Jan. 1999.

[68] H. Strack, "Ion Bombardment of Silicon in a Glow Discharge," *J. Appl. Phys.*, vol. 34, no. 8, p. 2405, 1963.

[69] W. Ensinger, "Semiconductor processing by plasma immersion ion implantation," *Mater. Sci. Eng. A*, vol. 253, no. 1–2, pp. 258–268, Sep. 1998.

[70] J. F. Ziegler, U. Littmark, and J. P. Biersack, *The stopping and range of ions in solids / J.F. Ziegler, J.P. Biersack, U. Littmark*. Pergamon New York, 1985.

[71] "http://www.srim.org/SRIM/SRIMLEGL.htm." .

[72] N. S. Saks, A. V. Suvorov, and D. C. Capell, "High temperature high-dose implantation of aluminum in 4H-SiC," *Appl. Phys. Lett.*, vol. 84, no. 25, p. 5195, 2004.

[73] V. Heera, D. Panknin, and W. Skorupa, "p-Type doping of SiC by high dose Al implantation—problems and progress," *Appl. Surf. Sci.*, vol. 184, no. 1–4, pp. 307–316, Dec. 2001.

[74] M. K. Linnarsson, M. S. Janson, U. Zimmermann, B. G. Svensson, P. O. Å. Persson, L. Hultman, J. Wong-Leung, S. Karlsson, A. Schöner, H. Bleichner, and E. Olsson, "Solubility limit and precipitate formation in Al-doped 4H-SiC epitaxial material," *Appl. Phys. Lett.*, vol. 79, no. 13, p. 2016, 2001.

[75] M. Rambach, A. J. Bauer, and H. Ryssel, "High Temperature Implantation of Aluminum in 4H Silicon Carbide," *Mater. Sci. Forum*, vol. 556–557, pp. 587–590, 2007.

[76] Y. Negoro, T. Kimoto, and H. Matsunami, "High-voltage 4H-SiC pn diodes fabricated by p-type ion implantation," *Electron. Commun. Japan (Part II Electron.*, vol. 86, no. 12, pp. 44–51, Dec. 2003.

[77] L. Ottaviani, S. Biondo, S. Morata, O. Palais, T. Sauvage, and F. Torregrosa, "Influence of Heating and Cooling Rates of Post-Implantation Annealing Process on Al-Implanted 4H-SiC Epitaxial Samples," *Mater. Sci. Forum*, vol. 645–648, pp. 717–720, Apr. 2010.

[78] R. Nipoti, F. Mancarella, F. Moscatelli, R. Rizzoli, S. Zampolli, and M. Ferri, "Carbon-Cap for Ohmic Contacts on Ion-Implanted 4H–SiC," *Electrochem. Solid-State Lett.*, vol. 13, no. 12, p. H432, 2010.

[79] S. Ahmed, C. J. Barbero, T. W. Sigmon, and J. W. Erickson, "Boron and aluminum implantation in α-SiC," *Appl. Phys. Lett.*, vol. 65, no. 1, p. 67, 1994.

[80] L. Ottaviani, V. Vervisch, F. Issa, and A. Lyoussi, "Procédé de réalisation d'un détecteur de neutrons et détecteur de neutrons," B2944-HD15654.

[81] L. Ottaviani, S. Biondo, M. Kazan, O. Palais, J. Duchaine, F. Milesi, R. Daineche, B. Courtois, and F. Torregrosa, "Implantation of Nitrogen Atoms in 4H-SiC Epitaxial Layers: A Comparison between Standard and Plasma Immersion Processes," *Adv. Mater. Res.*, vol. 324, pp. 265–268, Aug. 2011.

[82] L. Ottaviani, M. Kazan, S. Biondo, F. Tuomisto, F. Milesi, J. Duchaine, F. Torregrosa, and O. Palais, "Study of Defects Generated by Standard- and Plasma-Implantation of Nitrogen Atoms in 4H-SiC Epitaxial Layers," *Mater. Sci. Forum*, vol. 725, pp. 41–44, Jul. 2012.

[83] S. Biondo, L. Ottaviani, M. Lazar, D. Planson, J. Duchaine, V. Le Borgne, M. A. El Khakani, F. Milesi, W. Vervisch, O. Palais, and F. Torregrosa, "4H-SiC P+N UV Photodiodes : A Comparison between Beam and Plasma Doping Processes," *Mater. Sci. Forum*, vol. 717–720, pp. 1203–1206, May 2012.

[84] S. Biondo, M. Lazar, L. Ottaviani, W. Vervisch, O. Palais, R. Daineche, D. Planson, F. Milesi, J. Duchaine, and F. Torregrosa, "Electrical Characteristics of SiC UV-Photodetector Device from the P-I-N Structure Behaviour to the Junction Barrier Schottky Structure Behaviour," *Mater. Sci. Forum*, vol. 711, pp. 114–117, Jan. 2012.

[85] N. Ramungul, V. Khemka, R. Tyagi, T. P. Chow, M. Ghezzo, P. G. Neudeck, J. Kretchmer, W. Hennessy, and D. M. Brown, "Comparison of aluminum- and boron-implanted vertical 6H-SiC p+n junction diodes," *Solid. State. Electron.*, vol. 42, no. 1, pp. 17–22, Jan. 1998.

[86] M. Ghezzo, D. M. Brown, E. Downey, J. Kretchmer, and J. J. Kopanski, "Boron-implanted 6H-SiC diodes," *Appl. Phys. Lett.*, vol. 63, no. 9, p. 1206, 1993.

[87] T. Kimoto, N. Miyamoto, A. Schöner, A. Saitoh, H. Matsunami, K. Asano, and Y. Sugawara, "High-energy (MeV) Al and B ion implantations into 4H-SiC and fabrication of pin diodes," *J. Appl. Phys.*, vol. 91, no. 7, p. 4242, 2002.

[88] T. Kimoto, A. Itoh, H. Matsunami, T. Nakata, and M. Watanabe, "Aluminum and boron ion implantations into 6H-SiC epilayers," *J. Electron. Mater.*, vol. 25, no. 5, pp. 879–884, May 1996.

[89] H. Bracht, N. A. Stolwijk, M. Laube, and G. Pensl, "Diffusion of boron in silicon carbide: Evidence for the kick-out mechanism," *Appl. Phys. Lett.*, vol. 77, no. 20, p. 3188, 2000.

[90] M. Laube, G. Pensl, and H. Itoh, "Suppressed diffusion of implanted boron in 4H–SiC," *Appl. Phys. Lett.*, vol. 74, no. 16, p. 2292, 1999.

[91] T. Tsirimpis, M. Krieger, H. B. Weber, and G. Pensl, "Electrical Activation of B+-Ions Implanted into 4H-SiC," *Mater. Sci. Forum*, vol. 645–648, pp. 697–700, Apr. 2010.

[92] F. Issa, V. Vervisch, L. Ottaviani, D. Szalkai, L. Vermeeren, A. Lyoussi, A. Kuznetsov, M. Lazar, A. Klix, O. Palais, and A. Hallén, "Nuclear Radiation Detectors Based on 4H-SiC p+-n Junction," *Mater. Sci. Forum*, vol. 778–780, pp. 1046–1049, Feb. 2014.

[93] H. Blom, T. Larsson, S. Berg, and M. Östling, "Reactively sputtered titanium boride thin films," *J. Vac. Sci. Technol. A*, vol. 7, no. 2, 1989.

[94] F. Sarubbi, T. L. M. Scholtes, and L. K. Nanver, "Chemical Vapor Deposition of α-Boron Layers on Silicon for Controlled Nanometer-Deep p + n Junction Formation," *J. Electron. Mater.*, vol. 39, no. 2, pp. 162–173, Dec. 2009.

[95] "www.cree.com."

[96] J. H. Park and P. H. Holloway, "Effects of nickel and titanium thickness on nickel/titanium ohmic contacts to n-type silicon carbide," *J. Vac. Sci. Technol. B Microelectron. Nanom. Struct.*, vol. 23, no. 2, p. 486, 2005.

[97] P. Macháč, B. Barda, and J. Maixner, "Structural characterization of nickel–titanium film on silicon carbide," *Appl. Surf. Sci.*, vol. 254, no. 6, pp. 1691–1693, Jan. 2008.

[98] B. Barda, P. Macháč, M. Hubičková, and J. Náhlík, "Comparison of Ni/Ti and Ni ohmic contacts on n-type 6H–SiC," *J. Mater. Sci. Mater. Electron.*, vol. 19, no. 11, pp. 1039–1044, Nov. 2007.

[99] F. Laariedh, M. Lazar, P. Cremillieu, J. Penuelas, J. L. Leclercq, and D. Planson, "The role of nickel and titanium in the formation of ohmic contacts on p-type 4H–SiC," *Semicond. Sci. Technol.*, vol. 28, no. 4, p. 045007, Apr. 2013.

[100] R. Konishi, R. Yasukochi, O. Nakatsuka, Y. Koide, M. Moriyama, and M. Murakami, "Development of Ni/Al and Ni/Ti/Al ohmic contact materials

for p-type 4H-SiC," *Mater. Sci. Eng. B*, vol. 98, no. 3, pp. 286–293, Apr. 2003.

[101] P. J. Ouseph, *Introduction to Nuclear Radiation Detectors*, vol. 51, no. 4. Boston, MA: Springer US, 1975.

[102] H. Spieler, *Semiconductor detector systems*. Oxford university press, 2005.

[103] S. Ben Krit, W. Rahajandraibe, K. Coulie-Castellani, G. Micolau, and A. Lyoussi, "First Investigations on the Feasibility of Integration of a Readout System for Neutrons Detection in Harsh Environment," *IEEE Trans. Nucl. Sci.*, vol. 61, no. 4, pp. 2271–2278, Aug. 2014.

[104] L. Vermeeren, W. Leysen, D. Szalkai, A. Klix, and F. Issa, "Report on tests of signal processing under real irradiation conditions (such as neutron-gamma discrimination)," 2014.

[105] F. Issa, V. Vervisch, L. Ottaviani, D. Szalkai, L. Vermeeren, A. Lyoussi, A. Kuznetsov, M. Lazar, A. Klix, O. Palais, and A. Hallen, "Radiation Silicon Carbide Detectors Based on Ion Implantation of Boron," *IEEE Trans. Nucl. Sci.*, vol. 61, no. 4, pp. 2105–2111, Aug. 2014.

[106] F. Issa, V. Vervisch, L. Ottaviani, D. Szalkai, L. Vermeeren, A. Lyoussi, A. Kuznetsov, M. Lazar, A. Klix, O. Palais, and A. Hallén, "Improvements in realizing 4H-SiC thermal neutron detectors," in *Fifteenth International Symposium on Reactor Dosimetry (ISRD)*, 2014.

[107] V. Vervisch, F. Issa, S. Biondo, L. Ottaviani, W. Vervisch, D. Szalkai, L. Vermeeren, A. Klix, A. Hallen, A. Kuznetsov, M. Lazar, and A. Lyoussi, "Thermal neutron detection enhancement by 10B implantation in silicon carbide sensor," *MRS Proc.*, vol. 1693, Jul. 2014.

[108] P. Rinard, "Neutron interactions with matter," *Passiv. Nondestruct. Assay Nucl. Mater.*, pp. 357–377, 1991.

[109] F. Franceschini and F. H. Ruddy, "Silicon Carbide Neutron Detectors," *Prop. Appl. Silicon Carbide, R. Gerhardt ed., InTech*, 2011.

[110] S. Biondo, W. Vervisch, L. Ottaviani, V. Vervisch, R. Ferrone, and A. Lioussy, "Simulations of interactions between fast neutrons and 4H-SiC detectors," *Mater. Sci. Forum*, 2014.

[111] D. Szalkai, A. Klix, F. Issa, L. Ottaviani, V. Vervisch, L. Vermeeren, and A. Lyoussi, "Fast neutron detection with SiC semiconductor detector on elevated temperatures," in *AMNT*, 2015, p. in press.

[112] Y. P. Varshni, "Temperature dependence of the energy gap in semiconductors," *Physica*, vol. 34, no. 1, pp. 149–154, Jan. 1967.

[113] R. Ferone, F. Issa, D. Szalkai, A. Klix, L. Ottaviani, S. Biondo, V. Vervisch, L. Vermeeren, R. Saenger, and A. Lyoussi, "SiC-based Neutron Detector in Quasi-realistic Working Conditions : Efficiency and Stability at Room and High Temperature Under Fast Neutron Irradiations," in *International Conference on Advancements in Nuclear Instrumentation, Measurement Methods and their Applications (ANIMMA)*, 2015.